MPM SCIENTIFIC JOURNAL

ISSN 1605-2730

MATERIALS PHYSICS AND MECHANICS

Vol. 37, No. 2, 2018

MATERIALS PHYSICS AND MECHANICS

"Materials Physics and Mechanics" Editorial Office:
Phone: +7(812)591 65 28 **E-mail:** mpmjournal@spbstu.ru **Web-site:** http://www.mpm.spbstu.ru

International scientific journal "**Materials Physics and Mechanics**" is published by Peter the Great St.Petersburg Polytechnic University in collaboration with Institute of Problems of Mechanical Engineering of the Russian Academy of Sciences in both hard copy and electronic versions.

The journal provides an international medium for the publication of reviews and original research papers written in English and focused on the following topics:

- Mechanics of nanostructured materials (such as nanocrystalline materials, nanocomposites, nanoporous materials, nanotubes, quantum dots, nanowires, nanostructured films and coatings).
- Physics of strength and plasticity of nanostructured materials, physics of defects in nanostructured materials.
- Mechanics of deformation and fracture processes in conventional materials (solids).
- Physics of strength and plasticity of conventional materials (solids).

Owner organizations: Peter the Great St. Petersburg Polytechnic University; Institute of Problems of Mechanical Engineering RAS.

Materials Physics and Mechanics is indexed in Chemical Abstracts, Cambridge Scientific Abstracts, Web of Science Emerging Sources Citation Index (ESCI) and Elsevier Bibliographic Databases (in particular, SCOPUS).

MPM MATERIALS PHYSICS AND MECHANICS

МЕХАНИКА И ФИЗИКА МАТЕРИАЛОВ

Materials Physics and Mechanics

Vol. 37, No. 2, 2018

Based on presentations of 2017 International Conference on "Physics and Mechanics of New Materials and Their Applications", PHENMA-2017, 14-16 October, 2017, Jabalpur, India

Edited by
Ivan A. Parinov, Shun-Hsyung Chang, Vijay K. Gupta

Учредители:
ФГАОУ ВО «Санкт-Петербургский политехнический университет Петра Великого»
ФГБУН «Институт проблем машиноведения Российской Академии Наук»

Тел.: +7(812)591 65 28 **E-mail:** mpmjournal@spbstu.ru **Web-site:** http://www.mpm.spbstu.ru

Тематика журнала

Международный научный журнал "Materials Physics and Mechanics" издается Санкт-Петербургским политехническим университетом Петра Великого в сотрудничестве с Институтом проблем машиноведения Российской Академии Наук в печатном виде и электронной форме. Журнал публикует обзорные и оригинальные научные статьи на английском языке по следующим тематикам:

- Механика наноструктурных материалов (таких как нанокристаллические материалы, нанокомпозиты, нанопористые материалы, нанотрубки, наноструктурные пленки и покрытия, материалы с квантовыми точками и проволоками).
- Физика прочности и пластичности наноструктурных материалов, физика дефектов в наноструктурных материалах.
- Механика процессов деформирования и разрушения в традиционных материалах (твердых телах).
- Физика прочности и пластичности традиционных материалов (твердых тел).

Редколлегия принимает статьи, которые нигде ранее не опубликованы и не направлены для опубликования в другие научные издания. Все представляемые в редакцию журнала "Механика и физика материалов" статьи рецензируются. Статьи могут отправляться авторам на доработку. Не принятые к опубликованию статьи авторам не возвращаются.

Журнал "Механика и физика материалов" ("Materials Physics and Mechanics") включен в систему цитирования Web of Science Emerging Sources Citation Index (ESCI), SCOPUS и РИНЦ.

Contents

Materials Physics and Mechanics 37 (2018) 109-117 Received: December 22, 2017

STUDY OF THE PROPERTIES OF CU-CONTAINING POLYACRYLONITRILE NANOSTRUCTURED GAS-SENSING FILMS

T.V. Semenistaya

Institute of Nanotechnologies, Electronics and Equipment Engineering, Southern Federal University,

2 Shevchenko Str., Taganrog, 347928, Russia

e-mail: semenistayatv@sfedu.ru

Abstract. The Cu-containing polyacrylonitrile (PAN) thin films (0.04 – 0.6 μm thicknesses) were fabricated using IR-pyrolysis in ambient argon in different temperature and time modes. The films were studied by X-ray photoelectron spectroscopy (XPS), X-ray diffraction (XRD), transmission electron microscopy (TEM) and atomic force microscopy (AFM). CuCl, Cu_2O and Cu crystalline inclusions were obtained in the nanocomposite films by XRD. The film microstructure was analyzed by AFM and TEM: the typical morphology corresponds to composite film with nanoparticles of 10 nm average size in the polymer matrix. The film electrical resistance was in the range from $4.0 \cdot 10^2$ to $2.7 \cdot 10^{11}$ Ω. The Cu-containing PAN nanocomposite films are promising for application as low-temperature NO_2 sensor in 36.5 – 255 ppm concentration range.

Keywords: IR-pyrolized polyacrylonitrile; electroconductive organic polymers; gas-sensing materials; nanostructured films; AFM; XPS; XRD; TEM.

1. Introduction

Polymeric materials have gained a wide theoretical interest and can be used for very different purposes and demonstrate unique possibilities [1 – 3]. Recent advances in polymer science and film preparation have made polymeric material films useful, practical and economical in a wide range of sensor designs and applications [4 – 12]. PAN is extremely popular and attracts much attention due to its unique structure. It is capable to change its microstructure under heating, possesses tolerance to most solvents and commercial availability [13 – 17]. Hydrolyzed PAN membranes widely used as a support for the assembly of a composite membrane and play an important role in the processes of pervaporation, bioproduct purification and water treatment [18]. PAN membranes, prepared via thermally induced phase separation process using dimethylsulfone/glycerol as the mixed diluents, may be suitable for micro- or ultra-filtration processes in water treatments [19]. The pyrolyzed PAN becomes conducting conjugative polymer matrix and acts as a buffer to relieve the morphological change of Sb, and as an inactive component to prevent the further aggregation of Sb during cycling. Nano Sb and Sn encapsulated pyrolytic PAN composites are used for anode material in lithium-ion batteries [20, 21].

The recent review by Nataraj et al. [22] describes the chemistry and applications of PAN-based nanofibers. PAN is the most commonly used polymer for producing carbon nanofibers, mainly due to its high carbon yield (up to 56%), flexibility of tailoring the structure of the final carbon nanofiber products due to the formation of a ladder structure via nitrile polymerization. The chemistry of PAN is of particular interest because of its use as a precursor in the formation of carbon nanofibers for different applications, including porous

http://dx.doi.org/10.18720/MPM.3722018_1

structured carbon nanofibers of high surface area for elecrtronics and energy storage applications [22]. Therefore, PAN-based nanofibers have been the subject of considerable interest, PAN nanocomposites, combined with various transition metal compounds, were found as better choice for gas-sensing material due to their good environmental and chemical stability, ease of synthesis, inexpensive monomer and their ability to change the structural and electric properties under thermal treatment. This inspires the idea that PAN films can be appropriate material for high performance sensors. PAN films can be considered as one of the most promising material in order to obtain chemo-resistive sensors for environmental applications.

In this paper, we describe low-cost flexible sensors, used for the detection of nitrogen dioxide and based on a conducting nanocomposite Cu-containing PAN films, obtained by IR-pyrolysis in ambient argon. The electrical transport properties of the fabricated films, deposited on polycor substrates were evaluated from electrical measurements, performed at different temperatures. Sensing measurements were performed under exposition to calibrated nitrogen dioxide gas at concentration ranging between 36.5 ppm and 255 ppm with air as the buffer gas, at different temperatures and under different relative humidity levels.

In the present work, we studied gas-sensing properties of the Cu-containing PAN nanocomposite films in dependence on a modifying additives concentrations and technological parameters of the films fabrication that influence the formed polymer structure.

2. Experimental technique

Thermally treated PAN polymer shows a rich evolution of structural and electric properties: the chains undergo cyclization to form a conjugated-chain chemical structure, resulting in electrical conductivity. PAN becomes a conjugated conducting polymer by low temperature pyrolysis [23, 24]. On the other hand, PAN is a very processable polymer, which can be dissolved in DMF. It is also found that the doping of PAN prior to carbonization can alter the physicochemical nature of the polymer under the thermal treatment [25]. The thermal treatment of PAN leads to changes in physical properties, which are of great practical importance. A perspective application of this thermal treatment of PAN was found, when this polymer was used as a precursor to produce high quality carbon materials. An early initiation and sufficient cyclization is an important precondition for obtaining stabilized carbon materials with uniform microstructure [26].

Fabrication of Cu-containing polyacrylonitrile films. The Cu-containing polyacrylonitrile films were fabricated by pyrolysis method under the influence of incoherent IR-radiation under inert atmosphere conditions. The following components were used: polyacrylonitrile (PAN) (Aldrich 181315) as a conductive polymer matrix, copper chloride (II) $CuCl_2$ as a modifying additive to increase the selectivity and adsorption activity of the nanocomposite films, dimethylformamide (DMF) as a solvent.

A film forming solution was prepared by dissolving 0.8 g PAN and copper chloride (II) in an amount of 0.2 – 10 wt. % in 20 ml DMFA under stirring at 90 ºC. After being cooled down to room temperature, the film-forming solution was deposited (centrifuged) on quartz substrates and then dried at 90 ºC for 30 minutes. Further, the samples were stored in air for 24 hours at 22 °C until full bleaching to extract the solvent.

IR-pyrolysis of the samples was carried out in several steps: the chamber of IR-radiation in ambient air was used at the first stage for oxidizing thermal stabilization of the PAN polymer; the IR-annealing device «Foton» was used in ambient argon at the second stage for PAN carbonization. Halogen lamps KG-220 with high radiation in the area of 0.8 μm – 1.2 μm were used as the source of radiation. Uniform heating of the samples was supplied with up and down position of the halogen lamps in the black lead cassette. The

thermoelectric couple chromium-aluminum inside the black lead cassette was used to control the intensity of IR-radiation. The temperature measurement accuracy was 0.25 ºC [27].

The time-temperature modes of IR-annealing were selected experimentally, since the intensity and duration of infrared radiation provide an opportunity to control the properties of the material films by changing the molecular structure of the polymer. The radiation intensity at the first stage of IR-annealing corresponds to temperatures of 150 ºC and 220 °C during a 15-minute period each sequentially, and the intensity of radiation at the second stage of the IR-annealing corresponds to temperatures of 500 – 800 °C during a 5 – 15-minute period [28].

Methods of film analysis. The thickness of the films was measured by the interferential microscopy using interferometer MII-4. The films structure was analyzed by X-ray diffraction (XRD) technique using DRON-6 with CuKα 1.54051 Å radiation. EFTEM (energy-filtered TEM) microanalysis was done using LEO 912 ABOMEGA transmission electron microscope fitted with an in-column Omega energy filter, having such characteristic as an operating accelerating voltage of 100 kV; magnification: 80 – 500000x; image resolution: 0.2 – 0.34 nm. The surface morphology was observed by atomic force microscopy (AFM) using scanning probe microscope Solver P-47. The X-ray photoelectron spectra were recorded by means of a Kratos Axis Ultra spectrometer using excitation with monochromatic Al Kα radiation (1486.6 eV). The residual pressure in the spectrometer during the experiments was $5 \cdot 10^{-7}$ Pa. The spectra were processed with the Vision 2 software package (Kratos Analytical). The accuracy of the binding energies (E_b) determination was ~ 0.1 eV, and that of the quantitative analysis was 10 rel. %. The binding energy scale was calibrated against the C1s line of aliphatic carbon (E_b = 285.0 eV). The specific resistance measurements were carried out using a source measure unit VIK-UES 07 by four-point probe method. The electrical characteristics of the prepared samples were carried out in a setup, equipped with heating element [29]. Ag contacts were deposited on the film surface using the electro conductive glue in order to investigate the electrical properties of the samples.

The steady-state gas distribution method was used for testing gas-sensing properties. A specially made setup, equipped with a quartz chamber, sensor holder, gas and purge lines, was used to maintain the desired level of detected gas concentration. Sensing characteristics were examined on base of the measurement of the film resistance. The quartz chamber volume was around 700 cm^3 so that the change in gas concentration was immediate and measurements of the response time and the recovery time of the sensors were accurate. The response time was defined as the time, required to achieve 90% of the total resistance change, when the detected gas is introduced into air. The recovery time is the time, required to achieve 90% of the total resistance change, when the detected gas admission is turned off and the air is reintroduced into the chamber. The gas sensitivity (S) was defined as the following ratio: $S = (R_0 - R_g)/R_0$, when $R_0 > R_g$, where R_0 is the resistance in air, R_g is the resistance in the atmosphere of the detected gas [30].

3. Results and discussion

PAN has a number of advantageous properties: (i) the solubility in polar solvents (DMFA, dimethylsulfoxide, dimethylacetatamide) turning into gel that is advantage for copper particles uniform distribution in the polymer organic matrix; (ii) the ability to form thin films; (iii) the change of electrophysical properties from dielectric to semiconducting material under IR-annealing [31].

The thickness of the prepared films was measured by the method of the interferential microscopy (Fig. 1). The films growth was observed in accordance with the technological parameters and different weight concentration of a modifying additive in film-forming solutions. The PAN films thickness was between 0.01 – 0.03 μm. The Cu-containing PAN films were of various thicknesses in the range from 0.04 to 0.6 μm.

The phase formation and the surface crystallization were analyzed by the XRD. There are CuCl, Cu_2O and Cu crystalline inclusions in the composites films (Table 1). The XRD pattern of the synthesized sample contains peaks that characterize crystalline inclusions in the samples. This result is in good agreement with the other XRD reports (Table 1) [32 – 34].

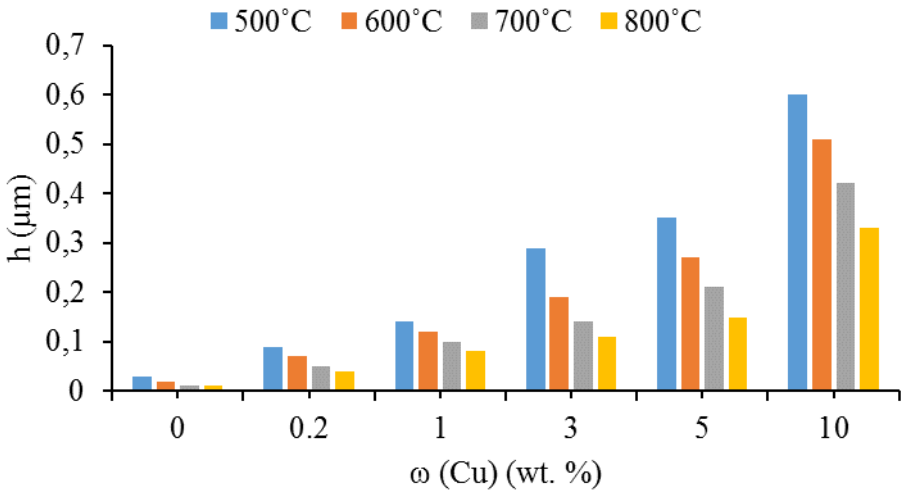

Fig. 1. 3D histogram, showing the films thickness dependence on the weight concentration of modifying additive and IR-pyrolysis temperature.

Table 1. XRD-data of the Cu-containing PAN films.

2θ					
CuCl		Cu_2O		Cu	
Tabular data	Actual data	Tabular data	Actual data	Tabular data	Actual data
28.12	28.22	37.01	37.05	43.29	43.36
36.42	36.02	–	–	–	43.6

The microstructure of the Cu-containing PAN film has been obtained, using EFTEM [35]. The micrograph clearly indicates copper compounds nanoparticles and their distribution, which size is 10 nm in average. We consider the polymer matrix stabilizes the nanoparticles and prevents their aggregation. The diffraction pattern indicates the crystalline order regardless of the light-sized nanoparticles. These TEM results were verified by XRD analysis [35].

X-ray photoelectron spectroscopy was used to study the composition and structural organization of the Cu-containing conducting polymer formed [36 – 39]. XPS survey and narrow scan data were taken on the film samples [35]. XPS survey spectra, acquired for the Cu-containing PAN film, are present in [35]. The peaks located at about 933 eV, 531 eV, 400 eV, and 285 eV correspond to the electron states of Cu2p, O1s, N1s and C1s in the PAN molecule, respectively. PAN, subjected to carbonization under controlled conditions, as it is known to transform into polymer with conjugated bonds [13, 16, 17, 24]. XPS signal characteristics of C1s, O1s, N1s confirm the well-known chemical structure of PAN polymer [35 – 41]. The C1s signal is dominated by a major peak at BE of approximately 284.7 eV. This peak can be attributed to aliphatic carbon (C – C) of the polymer chain, i.e. the carbon atoms bonded with carbon and hydrogen atoms [35, 36]. The intensity of the C1s peaks at 285.9 eV and at 286.7 eV, indicating the formation of carbon nitrogen atoms links in $(–CH_2CH(CN)–)_n$ and of imino bonds (C=N–) [35, 36, 44], respectively, is roughly equal.

The N1s core is on level spectrum of the Cu-containing PAN films. The large peak with its maximum at 398.4 is attributable to the imino-like (=N–) nitrogen atoms [45]. The peak at 400.4 eV can be seen due to carbons, linked to the nitrogen atom. The peak, located at 400.4 eV in the N1s core region corresponds to the binding energy of the nitrogen atoms in C–N=C bonds [45]. The peak-fit of the O1s core level reveals two binding energy states. The low-binding energy component at 530.9 eV is from CuO or Cu_2O. The high-binding energy component at 532,3 eV arises from carbon species, combined with oxygen (C=O, C–O–C) [43, 46].Two components by peak fitting the Cu XPS data were identified. The larger and narrower low-binding energy component at 932.6 eV is from metallic Cu or Cu(I) species and the higher binding energy component at 934.8 eV can be assigned to oxidized Cu [42 – 45]. In Table 2, the XPS elemental surface compositions of the Cu-containing PAN films are presented.

Table 2. Assignments of the main spectral bands, based on their binding energies (BE) and atomic concentration (AC) of the Cu-containing PAN films.

Element	BE (eV)	AC (at. %)	Assignments
C1s	284.7	81.1	$–(CH_2)–$
	285.9		$C≡N$ $(–CH_2CH(CN)–)_n$
	286.7		C–N, C=N, $(–CH_2CH(CN)–)_n$
	288.2		C=O, O–C–O
N1s	398.4	11.7	C=N–H
	400.4		–NH–, C–N=C
O1s	530.9	6.4	CuO, Cu_2O
	532.3		C=O, O–C–O
Cu2p	932.5	0.7	Cu^0, Cu^{1+} (Cu_2O)
	934.8		Cu^{2+} (CuO)

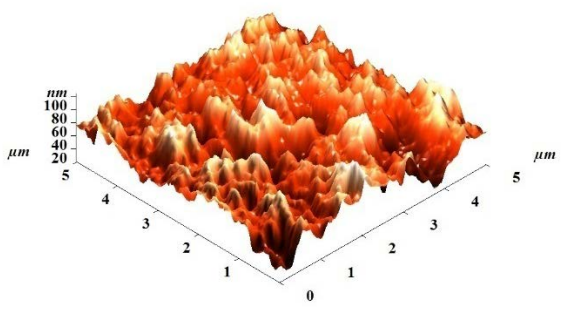

(a)

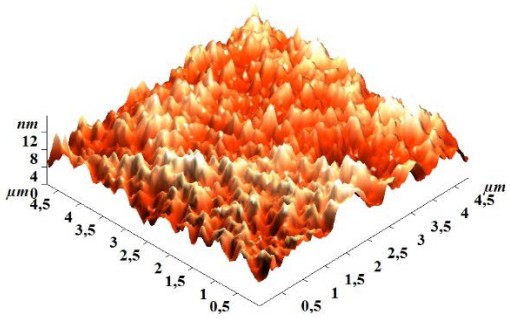

(b)

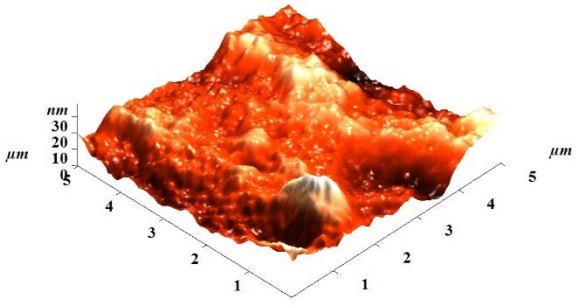

(c)

Fig. 2. AFM-images of the Cu-containing PAN films: 600-3 (a), 700-3 (b), 800-3 (c).

In order to observe clearly the microtopographical changes on the nanocomposite film surfaces, the AFM images of the film surfaces, formed under various time-temperature IR-annealing modes from film-forming solutions with different weight concentration of copper chloride (II), were taken and are shown in Fig. 2. It could be observed that the Cu-containing PAN films are dense and show a rough surface. When the IR-annealing temperature was increased to 800 ºC, a decrease in surface roughness was observed and the distribution of crystallite was uniform. High temperature enhances the crystallite size and the roughness decrease [42].

The statistical parameters of the surface morphology were estimated, using the Image Analysis software. Fig. 2 shows that the Cu-containing PAN samples change the surface roughness of the films due to fabrication temperature growth. It was noted that the surfaces became smoother. For example, the root-mean-square (*Rq*) surface roughness over an area of 5×5 μm^2 for the films changes from 15.4 nm to 1.9 nm, while forming films at 600 ºC and 700 °C, respectively [47].

Thus, using different time-temperature modes of the two-stage IR-pyrolysis allows fabricating the Cu-containing PAN films with nanosized particles of copper compounds with different surface morphology. The study of structure and composition of the fabricated films makes it possible to explain their electrical and gas-sensing properties.

The thin films with the resistance values in the range from $4.0 \cdot 10^2$ to $2.7 \cdot 10^{11}$ Ω were fabricated at various IR-annealing temperatures and using various weights of a modifying additive (Fig. 3). As observed from the Fig. 3, the film conductivity was improved significantly by the IR-annealing temperature growth and the increase of copper chloride (II) weight concentration.

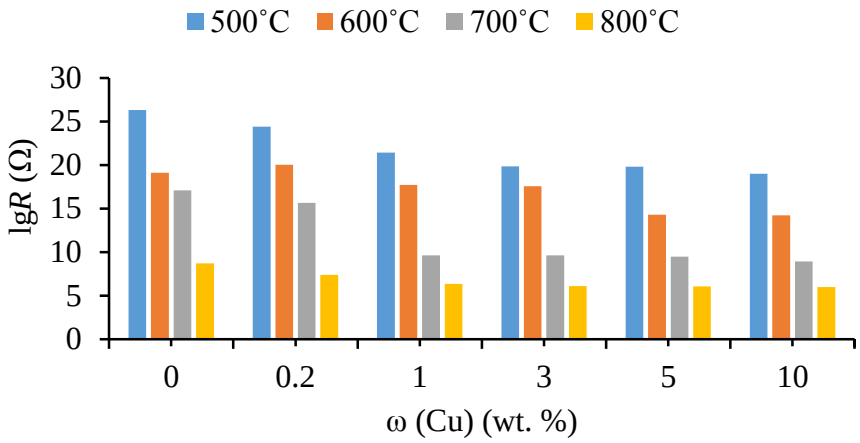

Fig. 3. Histogram, showing the dependence of the film resistance on the weight concentration of a modifying additive and IR-pyrolysis temperature.

According to the results of four-point probe measurements performed on PAN and Cu-containing PAN films, there is the exponential temperature dependence on the films resistance points to the semiconducting nature of the film material [29]. The resistance of the Cu-containing PAN films exponentially decreases with the temperature in the range between room temperature and 70 ºC above that temperature a linear dependence occurs.

The results of the sensing tests of the Cu-containing PAN films revealed their sensitivity to nitrogen dioxide NO_2 in the range of concentration between 36.5 – 255 ppm. The films material behavior is reversible that is the resistance decreases at the adding of NO_2 gas in the air flux, then it restores at fresh air. So, the conductivity of the film increases while adsorbing the gas-oxidizer, as NO_2 is an acceptor of electrons pointing to *p*-type semiconductor

characteristics of film material. In general, the sensitivity of the Cu-containing PAN sensors is affected by technological parameters as well as by the working temperature. The IR-annealing temperatures provide a possibility to manage the gas-sensing properties of the Cu-containing PAN [30].

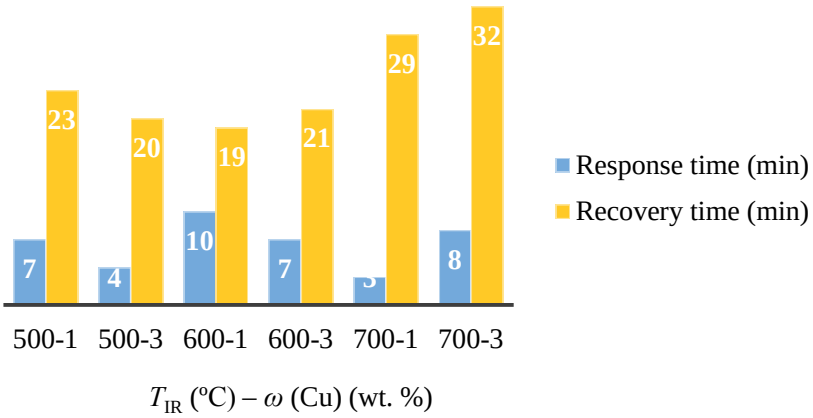

Fig. 4. Response time and recovery time of the Cu-containing PAN sensors *vs* IR-pyrolysis temperature (ºC) and weight concentration of a modifying additive (wt. %), at 20 °C, $c(NO_2)$ = 146 ppm.

The response time and the recovery time of the NO_2 sensors using the Cu-containing PAN nanocomposite films were defined (Fig. 4). The sensors display a relatively rapid response under NO_2 exposure and rather high recovery time: it is extended up to several tens of minutes. The IR-annealing temperatures exert bad influence on the recovery time. To meet the best sensitivity and the fastest response and recovery time requirements a sample, fabricated under 500 ºC from 3 wt. % film-forming solution, was used. The working temperature of the NO_2 sensor with the Cu-containing PAN films sensing layer was determined in the temperatures ranging between 20 °C and 50 °C. The response linearly decreases with the temperature increase in the specified range, the sensitivity of the sensor below 33 ºC was very low (~0.1 r.u.).

The films sensitivity as a function of relative humidity was measured in stationary conditions at 20 ºC. The relative humidity levels are established inside the measurement chamber by fluxing dry air mixed with humidity-saturated air at different ratios [48]. The sensing performances of the films are evaluated by means of electrical measurements, performed while exposing the samples to different relative humidity levels. It was found that within the range of humidity values from 43 % to 90 %, there is no essential change of gas sensitivity.

4. Conclusions

Cu-containing PAN films were fabricated by IR-pyrolysis in ambient argon and their structural and electrical properties were studied. Gas-sensing measurements were performed at low temperature in order to assess the sensing properties of the films for no-heated application. The fabricated films used as a sensing layer for chemo-resistive NO_2 sensor that operates at room temperature. The sensor was found to detect nitrogen dioxide gas down to 36.5 ppm with a reversible and reproducible response.

Acknowledgments. *This work was performed with the financial support of Southern Federal University within project No. VnGr-07/2017-21. The author is greatly thankful for the*

opportunity to fulfill the XPD and spectroscopic investigation to Kabardino-Balkarian State University; AFM investigation to Research and Educational Center of "Nanotechnology" of Southern Federal University; IR-pyrolysis on the installation «FOTON» of the A.I. Topchiev Institute of Petroleum Chemical Synthesis of the Russian Academy of Science.

References

[1] U. Lange, N.V. Roznyatovskaya, V.M. Mirsky // *Analytica Chimica Acta* **614 (**2008) 1.
[2] X. Li, Y. Wang, X. Yang, J. Chen, H. Fu, T. Cheng // *Trends in Anal. Chem.* **39 (**2012) 163.
[3] A. Iwan, D. Sek // *Prog. Polym. Sci*. **33** (2008) 289.
[4] B. Wang, Zh. Chen, X. Zuo, Y. Wu, Ch. He, X. Wang, Z. Li // *Sens. Actuators B* **160** (2011) 1.
[5] G. Han, G. Shi // *Thin Solid Films* **515** (2007) 6986.
[6] T. Fiorido, M. Bendahan, K. Aguir, S. Bernardini, C. Martini, H. Brisset, F. Fages, C. Videlot-Ackermann, J. Ackermann // *Sens. Actuators B* **151** (2010) 77.
[7] A. Singh, S. Samanta, A. Kumar, A.K. Debnath, R. Prasad, P. Veerender, V.Balouria, D.K. Aswal, S.K. Gupta // *Org. Electron* **13** (2012) 2600.
[8] P.P. Sengupta, P. Kar, B. Adhikari // *Thin Solid Films* **517** (2009) 3770.
[9] X. Wang, S. Ji, H. Wang, D. Yan // *Sens. Actuators B* **160** (2011) 115.
[10] S. Javadpour, A. Gharavi, A. Feizpour, A. Khanehzar, F. Panahi // *Sens. Actuators B* **142** (2009) 152.
[11] M.A. Chougule, Sh. Sen, V.B. Patil // *Synth.Met.* **162** (2012) 1598.
[12] S. Srivastava, S. Kumar, Y.K. Vijay // *Int. J. Hydrogen Energy* **37** (2012) 3825.
[13] C. Nandini, B. Sudhapada, S. Palit, M. Mrinal // *J.Polym. Sci. Part B: Polymer Physics* **12** (1995) 1705.
[14] M.A. Geiderikh // *Russ. Chem. Bull.* **14** (1965) 618.
[15] J.J. Ritsko, G. Crecelius, J. Fink // *Phys. Rev. B* **27 (**1983) 2612.
[16] M. Surianarayanan, R. Vijayaraghavan, K.V. Raghavan // *J. Polym. Sci.* **36 (**1998) 2503.
[17] N. Chatterjee, S. Basu, S.K. Palit, M.M. Maiti // *J. Polym. Sci. Part B: Polym. Phys.* **33 (**1995) 1705.
[18] G. Zhanga, H. Mengb, Sh. Jia // *Desalination* **242** (2009) 313.
[19] Q.-Y. Wu, L-S. Wan, Z-K. Xu // *J.Membrane Sci.* **409-410** (2012) 355.
[20] X. He, W. Pu, L. Wang, J. Ren, Ch. Jiang, Ch. Wan // *Electrochim. Acta* **52** (2007) 3651.
[21] X. He, W. Pu, L.Wang, J. Ren, Ch. Jiang, Ch. Wan // *Solid State Ionics* **178** (2007) 833.
[22] S.K. Nataraj, K.S. Yang, T.M. Aminabhavi // *Prog. Polym. Sci.* **37** (2012) 487.
[23] I-H. Chen, Ch.-Ch. Wang, Ch.-Y. Chen // *Carbon* **48** (2010) 604.
[24] M. Jing, Ch. Wang, Q. Wang, Y. Bai, B. Zhu // *Polym. Degrad. Stab.* **92** (2007) 1737.
[25] A.V. Korobeinyk, R.L.D. Whitby, S.V. Mikhalovsky // *Eur.Polym. J.* **48** (2012) 97.
[26] P. Miao, D. Wu, K. Zeng, G. Xu, Ch. Zhao, G. Yang // *Polym. Degrad. Stab.* **95** (2010) 1665.
[27] L.M. Zemtsov, G.P. Karpacheva // *High-molec. Comp*. **6(36)** (1994) 919.
[28] A.N. Korolev, I.S. Al-Hadrami, T.V. Semenistaya, G.P. Karpacheva, L.M. Zemtsov, T.P. Loginova, V.V. Petrov, T.N. Nazarova // *Russian Patent RU 2415158 C2,* 27.03.2011 (In Russian).
[29] I.S. Al-Hadrami, A.N. Korolev, L.M. Zemtsov, G.P. Karpacheva, T.V. Semenistaya // *Mater. Elektr. Tehniki* **1** (2008) 14 (In Russian).
[30] A.N. Korolev, T.V. Semenistaya, I.S. Al-Hadrami, T.N. Nazarova, V.V. Petrov // *Izv. VUZov Elektronika* **1** (2008) 20 (In Russian).
[31] A.A. Dulov, A.A. Slinkin, *Organic Semiconductors* (Nauka, Moscow, 1970) (In Russian).
[32] M.P. Wadekar, C.V. Rode, Y.N. Bendale, K.R. Patil, A.A. Prabhune // *J. Pharm. Biomed. Anal.* **39** (2005) 951.

[33] Y. Matsumura, H.Ishibe // *J. Catal*. **268** (2009) 282.
[34] A. Jagminas, G. Niaura, J. Kuzmarskyte, R. Butkiene // *Appl. Surf. Sci*. **225** (2004) 302.
[35] A.N. Korolev, T.V. Semenistaya, I.S. Al-Hadrami, T.P. Loginova, M. Bruns // *Persp. Mater*. **5** (2010) 52 (In Russian).
[36] http://srdata.nist.gov/xps/
[37] C.D. Wagner, W.M. Riggs, L.E. Davis, J.F. Moulder, G.E. Muilenberg, *Handbook of X-ray Photoelectron Spectroscopy* (Perkin-Elmer Corp., Phys. Electron. Division, Eden Prairie, Minn. 55344, 1979).
[38] G. Beamson, D. Briggs, *High Resolution XPS of Organic Polymers: the Scienta ESCA300 Database* (John Wiley & Sons, Ltd, Chichester, 1992).
[39] V.I. Nefedov, *X-ray Photoelectron Spectroscopy of Chemical Compounds. Handbook.* (Chemistry, Moscow, 1984) (In Russian).
[40] Yu.M. Shulga, V.I. Rubtsov, O.N. Efimov // *Vysokom. Soedin., Seriya A* **36(6)** (1996) 989 (In Russian).
[41] G.A. Shagisultanova, A.V. Shchukarev, T.V. Semenistaya // *Russ. J. Inorg. Chem*. **50(6)** (2005) 912 (In Russian).
[42] L.S. Dake, D.E. King, A.W. Czanderna // *Solid State Sci*. **2** (2000) 781.
[43] R.S. Vieira, M.L.M. Oliveira, E. Guibal, E. Rodríguez-Castellón, M.M. Beppu // *Colloids Surf. A: Physicochem. Eng. Aspects* **374** (2011) 108.
[44] V.W.L. Lim, E.T. Kang, K.G. Neoh // *Synth. Metals* **123** (2001) 107.
[45] D. Zheng, Z. Gao, X. He, F. Zhang, L. Liu // *Appl. Surf. Sci*. **211** (2003) 24.
[46] Z.Mekhalif, F. Sinapi, F. Laffineur, J. Delhalle // *J. Elect. Spectr. and Related Phen*. **121** (2001) 149.
[47] T.V. Semenistaya. In: *Advanced Materials - Manufacturing, Physics, Mechanics and Applications*, *Springer Proceedings in Physics*, ed.by Ivan A. Parinov, Shun-Hsyung Chang, Vitaly Yu. Topolov (Heidelberg, New York, Dordrecht, London: Springer Cham., 2016), Vol. 175, p. 61.
[48] G. Scandurra, A. Arena, C. Ciofi, A. Gambadoro, F. Barreca, G. Saitta, G. Neri // *Sens. Actuators B* **157** (2011) 473.

Materials Physics and Mechanics 37 (2018) 118-123 Received: December 22, 2017

SURFACE MORPHOLOGY STUDY OF GAS-SENSITIVE COBALT-CONTAINING POLYACRYLONITRILE NANOCOMPOSITE FILMS

M.M. Avilova, T.V. Semenistaya*, N.K. Plugotarenko

Institute of Nanotechnologies, Electronics and Equipment Engineering of Southern Federal University,

2 Shevchenko Str., Taganrog, 347928, Russia

*e-mail: semenistayatv@sfedu.ru

Abstract. The paper presents the results of studying the surface morphology of cobalt-containing polyacrylonitrile (PAN) films from the standpoint of the theory of self-organization and information theory. It is stated that the films surface is a set of fractals. The correlation dimension D and fractal dimension D_f of the fabricated films were calculated. Using the C++ software package program, mutual information of cobalt-containing PAN films surfaces was calculated, resulting in a correlation between the values of gas sensitivity coefficient and the values of average mutual information of cobalt-containing PAN films.

Keywords: polyacrylonitrile film; self-organization; correlation analysis; fractal analysis; average mutual information.

1. Introduction

Since the middle of the last century, it became known that polymer materials with a system of conjugated bonds exhibit semiconductor properties [1]. It is known that heat-treated PAN is an organic semiconductor, the value of its resistivity is in the range from 10^{10} Ω/cm to several Ω/cm [2], and is used to create various modern electronic devices, including sensors of resistive type [3].

Considering the anthropogenic impact on the environment, it is necessary to use gas sensors with high selective gas sensitivity to obtain accurate information on the quantitative and qualitative composition of the atmospheric air. Therefore, research in the field of creation of gas-sensitive materials with high sensitivity and selectivity is a topical issue in nanoelectronics. In [4] it is found there are self-affinity fractals due to self-organization processes occurring during the formation of organic material at the stage of heat stabilization in metal-containing PAN films that are characterized by high values of gas-sensitivity coefficient.

The surface of the semiconductor films is rough, structure of coatings can be determined by film fabrication technology [5], by deposition conditions and nature of the material. The developed surface-relief structure increases real surface area, which can significantly exceed the topological area. This affects the electrical and other functional properties of the films, in order to evaluate the effect of morphological characteristics, it is necessary to study the connection between surface roughness and fractal dimension.

The difficulty in estimation of the roughness and the size of the surface roughness is in the scale of the measurements, i.e. the scanning step while investigate film surface using scanning probe microscopy [6]. The fractal approach is invariant with respect to the measurement scale [7].

http://dx.doi.org/10.18720/MPM.3722018_2

There are accurate methods of theoretical research of film formation processes and features of their surface. Morphological characterization of surfaces of cobalt-containing PAN films, was explored by the method of atomic force microscopy (AFM). The irregular shape of thin-film surfaces requires such methods for description as the theory of self-organization [8].

To determine the self-organization processes in the cobalt-containing PAN films, the correlation (D) and fractal dimensions (D_f) are calculated. The advantage of the methods of the theory of self-organization is the analysis of the dynamic processes occurring in the structure under the temperature-time regimes of their formation.

However, the method of self-organization does not allow one to assess the degree of ordering of the structure of the polymer material associated with the dynamic processes occurring during its synthesis. The use of information theory allows evaluating relations between morphological characteristics of cobalt-containing PAN nanocomposite films and its sensitive properties. Average mutual information (AMI) value of cobalt-containing PAN films affords to estimate the relation between technological and AFM-image dataset [9]. It allows one to give a correlation model between the values of gas sensitivity coefficient and the value of AMI. Fisher test (F-test) was used to examine adequacy of the obtained numerical model.

The present work aims to identify presence of self-organization processes in the cobalt-containing PAN films, as well as to find relation between the gas sensitivity of the films and the surface morphology.

2. Experimental technique

The gas-sensitive material is a nanocomposite film [10], which consists of PAN and a modifying additive (cobalt concentrations are 0.0 %, 0.25 %, 0.5 %, 0.75 %, 1.0 %). The gas-sensitive material was deposited on a dielectric substrate. To obtain the cobalt-containing PAN films, the incoherent IR-radiation method was used.

To determine the gas-sensitive characteristics, silver contacts formed on the surface of the films. Gas sensitivity of the obtained samples was determined to nitrogen dioxide and chlorine at a temperature of 22 °C. The measured parameter was the resistance of the sample, the value of which changes depending on the concentration of the detected gas in the chamber. The gas sensitivity was evaluated using gas sensitivity coefficient S, which is calculated as

$$S = (R_a - R_g)/R_a, \quad (1)$$

where R_a is the resistance value of the film in air, R_g is the value of the film resistance in the atmosphere of the detected gas (NO_2).

The surface morphology was observed by atomic force microscopy (AFM) using scanning probe microscope Solver P-47. For the investigation of the films, point density of 256 points/1 μm is taken to obtain results, namely a minimum number of points, which are necessary to characterize the fractal behavior of the surfaces [11].

To study the presence of self-organization processes that occur during the thermal stabilization of cobalt-containing PAN films, an analysis of the surface morphology of the samples is made on the base of the AFM image (Fig. 1) and the profile height distribution functions are constructed (Fig. 2).

Using the Grassberger-Procaccia algorithm [12], the correlation dimension (D) of the surface of cobalt-containing PAN films was calculated by the Taken method [13]. As a result, not only a numerical equivalent is obtained that corresponds to the dimension identified for a particular sample, but also a frozen picture of the dynamics of the film surface formation is given. Then, in the Gwyddion software package, the fractal dimension of the surface (D_f) was calculated by four methods: cube counting method, triangulation method, variance method,

power spectrum method. The relative accuracy is ± 0.15. Close to the arithmetic mean is the calculation of fractal dimension by triangulation method.

To calculate value of AMI, the algorithm according to [9] was used. Correlation of the AMI values the gas sensitivity coefficient was determined by regression analysis (Fig. 3). For this, correlation coefficient (r) was calculated, then the coefficients of the regression equation were determined by least-squares method. Distributions of AMI value over the surface of cobalt-containing PAN films are obtained (Fig. 4), calculating the AMI in the C++ program.

3. Results and discussion

Figure 1 presents AFM images of samples of cobalt-containing PAN films with different concentrations of the modifying additive.

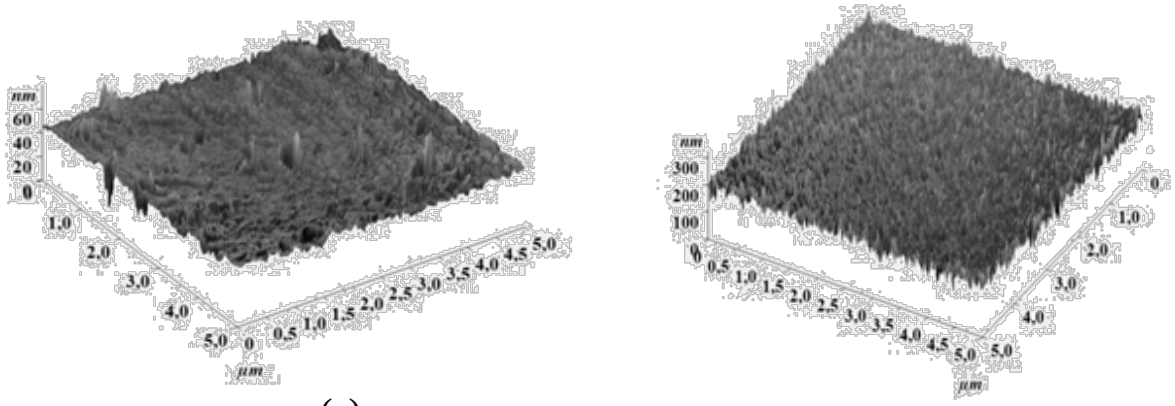

(a) (b)

Fig. 1. AFM image of the surface of Co-containing PAN films annealed at 450 °C with the concentration of the modifying additive in the film-forming solution: (a) ω = 0%; (b) ω = 0.25%.

Figure 2 shows the convergence of the value of D or the onset of the saturation moment and the presence of a plateau, which indicates the presence of self-organizing structures in the films.

Figure 2,a reveals linear section of the dependence of D on $\log^2(r)$ in the saturation zone (plateau region) that is a sign of deterministic chaos [14] and proves the presence of the self-organization process in the cobalt-containing PAN films. It was experimentally determined the maximum value of the gas sensitivity coefficient of the sample to nitrogen dioxide (S = 0.88 relative units).

The calculation of fractal dimension D_f for most samples showed that D_f values are within $2 < D_f < 3$ and in average equal to 2.2. The latter means that the samples have a small bulk, formed by the planar structures of the thin film. It is possible to assume that the three-dimensionality of the flat structures is attached to loose areas, formed by the cobalt metal oxides embedded in PAN matrix. At the same time, it was revealed that D_f = 3 is characteristic for films with a metal content of 0.25%, which allows us to relate these samples to a three-dimensional space from the position of the self-organization theory.

In order to find the interrelationships in the disordered structure of the surfaces of cobalt-containing PAN films from the position of information theory, the calculation of the AMI of samples surface with different concentrations of the modifying additives was carried out.

Correlation model, based on the calculated AMI and experimental values of gas sensitivity coefficient, was constructed (Fig. 3) and is described by the regression equation:

$$y(x) = -61313.18x + 1.19. \quad (2)$$

The coefficient of correlation between the values of the gas sensitivity coefficient and the AMI of 0.88 indicates a good linear dependence.

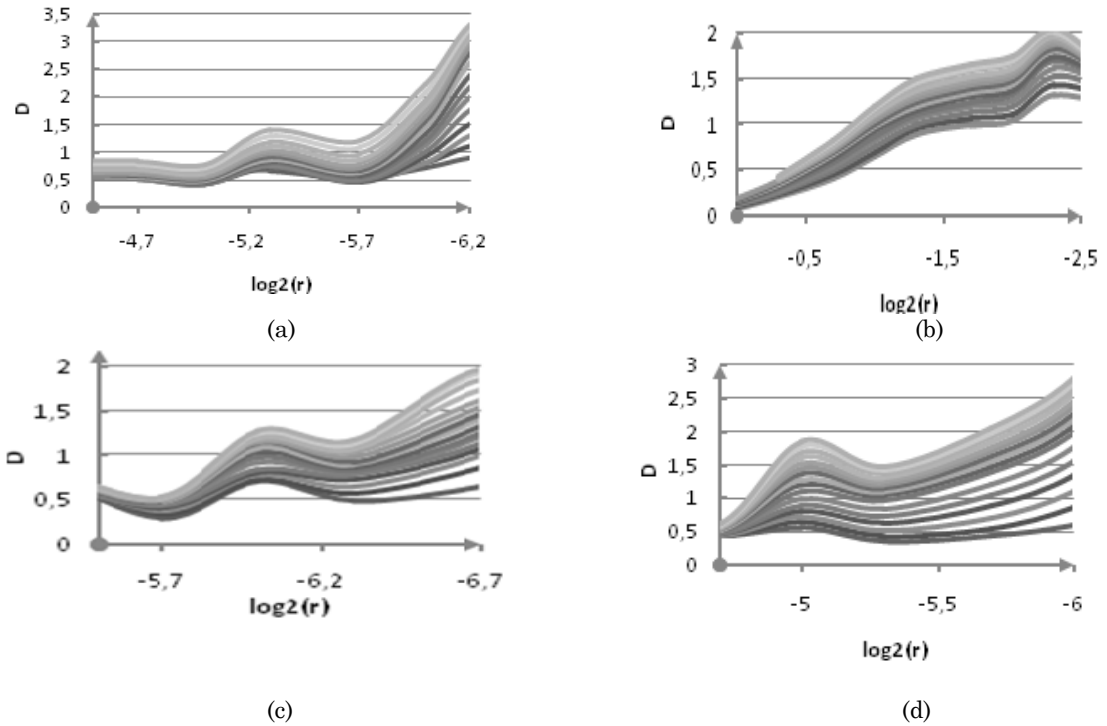

Fig. 2. Dependences of the correlation dimension *D* on the size of the phase space, for the surfaces of the Co-containing PAN films with the concentration of the modifying additive in the film-forming solution: (a) ω = 0.25 %, (b) ω = 0.5 %, (c) ω = 0.75 %, (d) ω = 1.0 %.

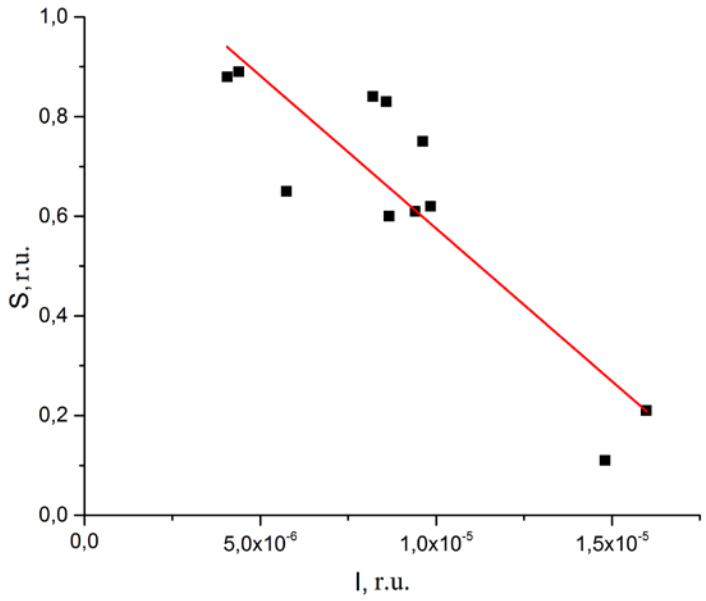

Fig. 3. Correlation of gas sensitivity coefficient and AMI in cobalt-containing PAN films.

Fisher test (F-test) was applied to the gained equation (2): the determination coefficient is $R^2 = 0.78$. In addition, the probability that the obtained model is incorrect corresponds to a value of 0.005. The latter testifies to the significance of this model and the adequacy of the obtained results.

In addition to the foregoing, as a result of calculating the AMI of the film surfaces (I), images of distribution of a given quantity were obtained (Fig. 4).

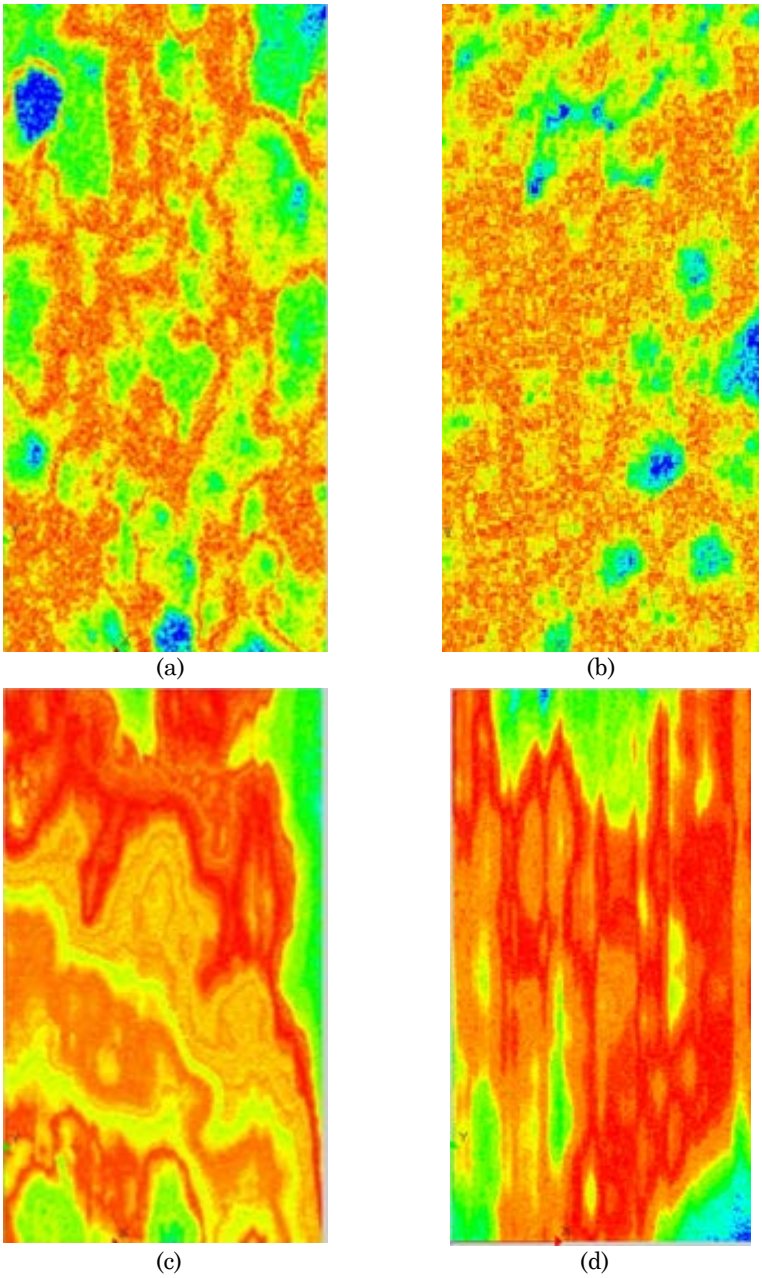

Fig. 4. AMI distribution over the surface of the cobalt-containing PAN films: (a) $I = 1.4 \cdot 10^{-5}$ r.u. and (b) $I = 1.6 \cdot 10^{-5}$ r.u. corresponding to low values of gas sensitivity coefficient to nitrogen dioxide; (c) $I = 0.2 \cdot 10^{-5}$ r.u. and (d) $I = 0.3 \cdot 10^{-5}$ r.u., corresponding to the highest values of gas sensitivity coefficient for nitrogen dioxide.

The results presented in Fig. 4 are consistent with the correlation model shown in Fig. 3. This allows us to conclude that the higher the AMI value, the lower value of the gas sensitivity coefficient to nitrogen dioxide. Fig. 4 indicates that films with similar gas

sensitivity, identical patterns of the distribution of the AMI value are characteristic. Thus, the gas sensitivity of cobalt-containing PAN films can be estimated by AMI distribution without preliminary laboratory analysis.

4. Conclusions

Based on the results of the theoretical study, carried out by the methods of self-organization theory and information theory, it has been confirmed that self-organization processes participate in the formation of cobalt-containing PAN films.

The results of the fractal analysis of the self-affine random surfaces using AFM show cobalt-containing PAN films with a metal content of 0.25%, which are characterized by the greatest values of gas sensitivity to nitrogen dioxide, and are referred to volumetric structures.

Based on the results of the mathematical model obtained, it has been established that there is an inverse correlation between the AMI and the gas sensitivity coefficient values of cobalt-containing PAN films.

Acknowledgments. *This work was performed with the financial support of Southern Federal University within project No. VnGr-07/2017-21. The equipment of the Research and Educational Center of "Nanotechnologies" and of the Research and Educational Center "Microsystem Technology and Multisensory Monitoring Systems" of Southern Federal University was used for this study.*

References

[1] T.V. Semenistaya, V.V. Petrov, *Metal-containing Polyacrylonitrile: Composition, Structure, Properties* (Southern Federal University Press. Taganrog, 2015) (In Russian).
[2] T.V. Semenistaya. In: *Advanced Materials - Manufacturing, Physics, Mechanics and Applications, Springer Proceedings in Physics*, ed.by Ivan A. Parinov, Shun-Hsyung Chang, Vitaly Yu. Topolov (Heidelberg, New York, Dordrecht, London: Springer Cham., 2016), Vol. 175, p. 61.
[3] T.V. Semenistaya, V.V. Petrov, T.A. Bednay, *Energy-effective Gas Sensors Based on Nano-composite, Organic Semiconductors* (Southern Federal University Press, Taganrog, 2013) (In Russian).
[4] N.A. Makeeva, Pin Lu, V.A. Ivanec, T.V. Semenistaya, N.K. Plugotarenko, A.N. Korolev // *Izvestiya SFedU. Engineering Sciences* **117** (2011) 149 (In Russian).
[5] P. Lu, V.A. Ivanec, T.V. Semenistaya, N.K. Plugotarenko // *Nano- and Microsystem Technique* **21** (2012) 21 (In Russian).
[6] N.A. Torhov, V.G. Bozhkov, I.V. Ivonin, V.A. Novikov // *Semicond.* **43** (2009) 38.
[7] A.R. Shugurov, A.V. Panin, A.O. Lyazgin, E.V. Shesterikov // *Pis'ma v ZHTF* **38** (2012) 70.
[8] W. Zahn, A. Zosch // *Fresenius. J. Anal. Chem.* **358** (1997) 119.
[9] V.V. Petrov, N.K. Plugotarenko, T.V. Semenistaya, M.M. Falchari // *Izvestiya SFedU. Engineering Sciences* **169** (2015) 184 (In Russian).
[10] T.V. Semenistaya et al. // *Surf. Eng. Appl. Electrochem.* **51** (2015) 9.
[11] W. Zahn, A. Zösch // *Fresenius. J. Anal. Chem.* **365** (1999) 168.
[12] A. Put, A. Vertes, D. Wegrzynek, B. Treiger, R. Grieken // *Fresenius. J. Anal. Chem.* **350** (1994) 440.
[13] J. Theiler // *Physical Review A* **36** (1987) 4456.
[14] S.P. Vihrov, N.V. Bodyagin, T.G. Larina, S.M. Mursalov // *Semicond.* **39** (2005) 953.

Materials Physics and Mechanics 37 (2018) 124-132 Received: December 22, 2017

3D PRINTING OF FLEXIBLE PARTS USING EVA MATERIAL

Narendra Kumar[1*], Prashant K. Jain[1], Puneet Tandon[1], Pulak Mohan Pandey[2]

[1]PDPM Indian Institute of Information Technology, Design and Manufacturing, Jabalpur, INDIA

[2]Indian Institute of Technology, Delhi, New Delhi, INDIA

[*]e-mail: narendra.kumar@iiitdmj.ac.in

Abstract. In the fused filament fabrication (FFF) process, filament buckling occurs during the processing of elastomers. Elastomer filament buckles between the rollers and liquefier head due to flexibility hence make difficult elastomer processing and extrusion through as mall nozzle. In this paper, ethylene vinyl acetate (EVA), an elastomer has been processed through the in-house developed CNC assisted material deposition tool (MDT). Instead of the filament, the developed system processes the material in the pellet form, which overcomes the limitations of FFF process in elastomer processing. An experimental study has been carried out to find the suitable set of process parameters setting for part fabrication. The fabricated parts show the flexibility similar to rubber, which is suitable for various end-use applications. The present study outcome shows that EVA material has the potential for additive manufacturing of flexible parts.

Keywords: additive manufacturing; 3D printing; pellet; screw extrusion; flexible; CNC milling machine; hybrid manufacturing; EVA.

1. Introduction

Additive manufacturing (AM) refers to the process of making three-dimensional objects in layer-by-layer fashion by using CAD data directly. Many AM processes have emerged over the time, and many more are in development stage [1]. Fused Deposition Modeling (FDM) or Fused Filament Fabrication (FFF) is one of the very popular AM processes, in which an object is made by depositing melted material in a predefined tool path [2]. It builds 3D objects using a filament of polymeric materials, however, now a day polymer composite filaments are also available in the market. FFF uses the appropriate size filament material that uncoils from a spool and enters inside the liquefier head with the help of drive wheels. Thermoplastics such as acrylonitrile butadiene styrene (ABS), polylactic acid (PLA), and nylon, etc. are widely used FFF materials to produce parts for various applications [3 – 5]. Sometimes, the specific materials are needed for to fulfill the demand of customers. Therefore, the technology should be more generic and compatible to accept the wide range of materials [6]. However, in FFF, there are many obstacles in the use of new materials such as specific size and properties requirement in the filament. For example, the available materials to be used in FFF process should be sufficiently rigid to withstand the force exerted by the counter-rotating rollers [7]. As the elastomers have less rigidity and low column strength, existing feeding system of commercial FFF cannot process the filaments made by elastomers. When the rollers push the elastomer filament into the liquefier of the FDM machine, it buckles due to low column strength and flexibility. Furthermore, the high melt viscosity of the elastomers requires substantial force to push the filament into the liquefier head as compared to other polymeric materials, which cannot be fulfilled due to low column strength as shown in Fig. 1. These two properties contradict each other. These constraints make commercial FFF systems

http://dx.doi.org/10.18720/MPM.3722018_3

incompatible for processing flexible filaments. Some researchers have done the modifications in the existing feeding systems of FFF to print flexible parts [2]. Nevertheless, this modification in the existing FFF feeding system may create the problem in the processing of other polymeric materials such as ABS and PLA, etc. It is worthwhile to develop a generic solution for fabricating 3D flexible or rigid parts. Instead of the filament, development of pellet feeding, based AM process, can provide the solution for this problem.

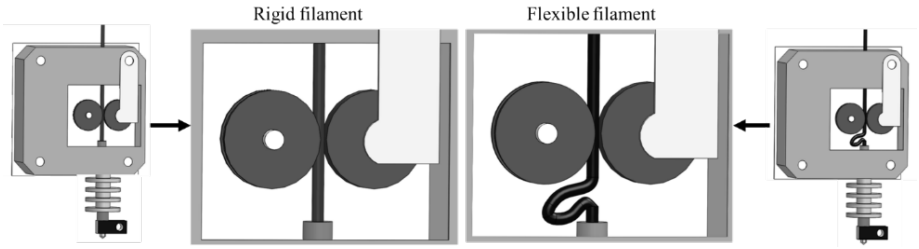

Fig. 1. Buckling issue in flexible filament feeding.

In order to overcome the limitations of FFF process, a pellet based innovative AM process has been implemented for fabricating flexible parts. A customized screw extrusion based material deposition tool (MDT) has been developed, which has pellet based feeding system to process the material. Hence, due to use of pellets, it unlocks the opportunities for the wide range of rigid as well as flexible polymeric materials. Ethylene vinyl acetate (EVA) is an elastomeric material and has many applications in the commercial market. However, the potential of this material has not been explored. Hence, the present study focuses on the investigation of EVA material for the use in additive manufacturing. Further, a study has been carried out to find the optimum process parameters. The printed parts of EVA have been tested for the flexibility.

2. Literature review

In the past decade, various efforts have been made towards the material development for the FFF process. The researchers focused on the new thermoplastics as well as hybrid polymer matrix composite materials for the use in FFF process. Masood et al. mixed the iron particles with the nylon matrix and developed metal-polymer composite material as feedstock for the FDM process [8]. This feedstock filament was loaded into the feeding system of FDM machine to fabricate 3D objects. The objects were fabricated successfully without doing any single modification in the machine components. Another study on the metal-polymer composite material was carried out by Nikzad et al. [9]. Composite materials of iron/ABS and copper/ABS were successfully prepared in filament form. Experimental results showed that significant improvement in the part strength was observed in the parts made of composite materials. Carneiro et al. explored the possibilities of polypropylene (PP) as a new candidate material for the FDM [10]. They evaluated the entire process chain from the filament production to the samples fabrication from the material. Mechanical characterization of the sample parts was done, and the effect of process parameters on the mechanical properties was evaluated through experimental work. Further, FDM printed samples results were compared with the samples, prepared by compression molding process. Boparai et al. investigated the nylon6-Al-Al_2O_3 as an alternative filament material for FDM process [11]. In their study, the filament exhibited good thermal and wear properties but inferior mechanical properties as compared to the ABS material filament. Also, some researchers explored the nanoparticles filled polymers in FDM process. The different weight percentage of nanofibers were added in the ABS polymer matrix by Shofner et al. to reinforce the filament for the FDM process[12]. In order to analyze the results, the composite filament was compared with unfilled ABS filament. Significant changes in the mechanical properties were seen in the swelling

behavior of the filament. In another work, Francis and Jain developed the polymer-layered silicate nanocomposites for the FDM applications [13]. The results showed the significant improvement in the part strength when compared with other macro-composites produced parts by other researchers. Lee et al. attempted a work on flexible part fabrication through ABS material by varying the process parameters. They measured the elastic performance of the ABS made prototypes with the help of custom-made apparatus [14].

It can be seen from the aforementioned literature that the most of the researchers have focused on the enhancement of the part strength by adding micro or nanoparticles in the polymer matrix. Moreover, some of them explored the new materials for this process, but most of the studies were focused on the rigid thermoplastic materials such as ABS, polypropylene, nylon, etc. The prime concern of researchers was the strength of the printed parts. However, very few studies were considered the flexibility aspect of the material. To the best of author knowledge, none of them considered the elastomers in their study to fabricate flexible parts.

3. Ethylene vinyl acetate

Ethylene vinyl acetate (EVA) is the copolymer of ethylene and vinyl acetate. It is very flexible similar to rubber and has many properties such as excellent toughness, transparency, cracks resistant and easy processability, etc. In general, EVA is frequently used for fabricating flexible parts in the shoe, biomedical and electrical industries and conventional techniques are used to process this material. The properties of EVA such as low melting and quick curing make it more suitable for additive manufacturing of flexible parts. In this study, pellets of 2 – 3 mm size have been used, which was supplied by Ananta Polyrubb Pvt. Ltd.

4. CNC assisted Material Deposition Tool (MDT)

In CNC assisted MDT, proposed in this work, pellets of EVA material are directly used to fabricate 3D parts. The screw extrusion based principle is used to process the EVA pellets. The viscous paste of EVA material extrudes at a controlled rate through a nozzle of 0.8 mm diameter. MDT has various components such as barrel, screw, heater, funnel, band heater, and temperature controller, etc., as shown in Fig. 2. The MDT is attached to the available three-axis CNC milling machine at the place of the cutting tool, which makes it capable of moving in *x*, *y* and *z* directions by *G* and *M* codes. The codes are generated through indigenously developed software in the MATLAB. The material is extruded in the form of the filament on the built platform, located on the CNC table. During deposition of material, MDT moves in *x* and *z* directions, at the same time, built platform moves in the *y*-direction. Once, a layer is completed, the MDT moves in the upward direction equal to the layer thickness.

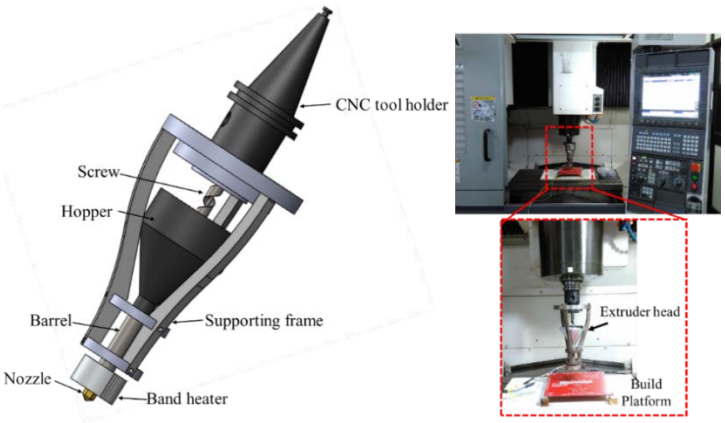

Fig. 2. Developed CNC assisted MDT system.

Since MDT is attached to the CNC milling machine, therefore, commercial tool path planning software of milling cannot work for additive manufacturing of the parts. Due to the limitations, a program was developed in the MATLAB software, which is capable of reading, slicing the part geometry in STL file. Further, tool path for each layer can be prepared by embedding the standard *G* and *M* codes of the milling machine. The user can change the process parameters such as layer thickness, deposition speed, road gap, etc., as per the need. Some features of the developed program are shown in Fig. 3.

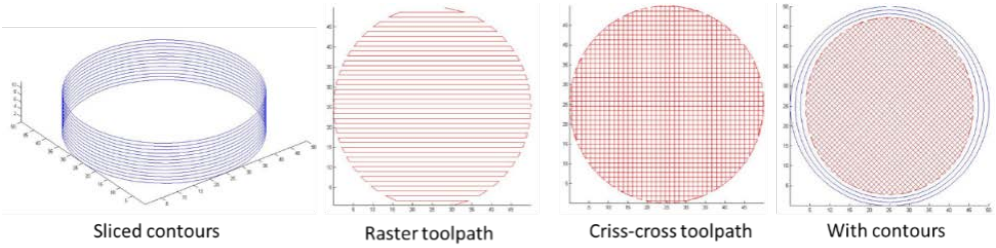

Fig. 3. Slicing contours and different types of the toolpath.

5. EVA behavior under different extrusion process parameters

An experimental study was carried out before flexible part fabrication to see the behavior of EVA material under different process conditions. Preliminary experiments were conducted to see the crucial parameters and based on the experimental results, barrel temperature and screw speed were selected as the input parameters as shown in Table 1, while flow rate and change in diameter were the output parameters.

Table 1. Selected parameters and their range.

Input Parameter	Selected Levels					
	1	2	3	4	5	6
Barrel Temperature (°C)	100	110	120	130	140	150
Screw Speed (RPM)	50	55	60	65	70	75

Determination of flow rate is necessary to examine because the material deposition speed can be obtained, which is very essential to fabricate the excellent quality parts. The diameter of the extrudate is considered due to its importance during the selection of appropriate road gap and layer thickness during the part fabrication. To study the extrudate diameter, the study was conducted in two phases. Firstly, the material was extruded vertically in the space without any deposition on the built platform while in the second phase the material was deposited onto the platform in a prescribed pattern as shown in Fig. 4. This is done because of the shape of extrudate changes after the deposition due to its weight. This change in shape depends on the viscosity of the deposited material. The shape of extruded remains circular before deposition due to the circular nozzle; it will be elliptical after the deposition onto the built platform. This cross-sectional change affects the dimensional accuracy and the part strength.

Obtained results for melt flow speed. The results obtained for melt flow speed for barrel temperature and screw speed are shown in Figs. 5 and 6, respectively. It can be seen that melt flow speed of the extrudate increases with the rise in barrel temperature (BT) and screw speed (RPM) both. This is because the temperature is rising, the considerable changes in the viscosity are occurring. As the temperature rises, the viscosity decreases, hence flowability of the extrudate improves. That is why melt flow speed of the material is increasing with temperature. Moreover, increase in screw speed increases the pressure gradient. Hence the considerable increment in melt flow speed can be observed. It means that

if the high value of screw speed and barrel temperature are considered for part fabrication, then the deposition speed will be high as compared to the other combination of process parameters.

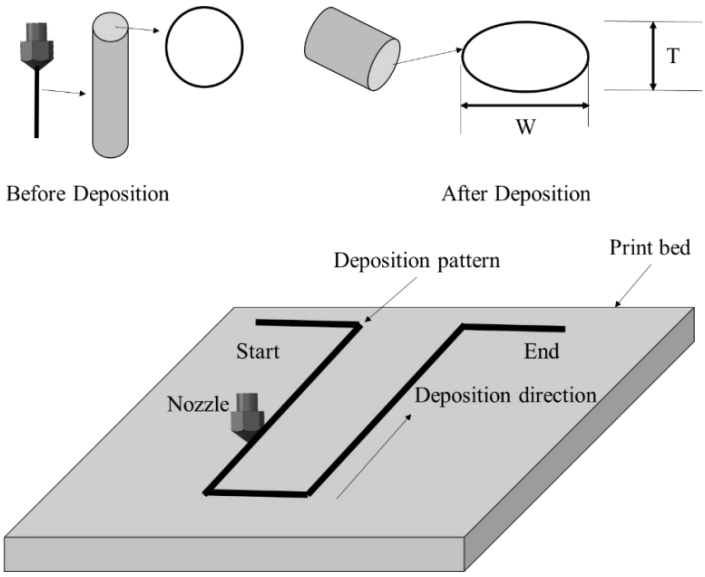

Fig. 4. Used material deposition pattern.

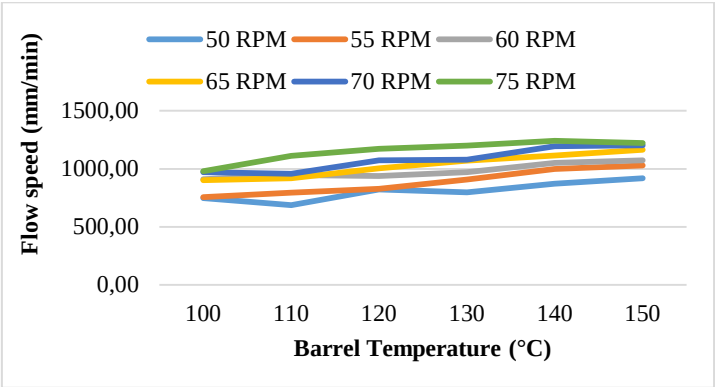

Fig. 5. Effect of barrel temperature on flow speed.

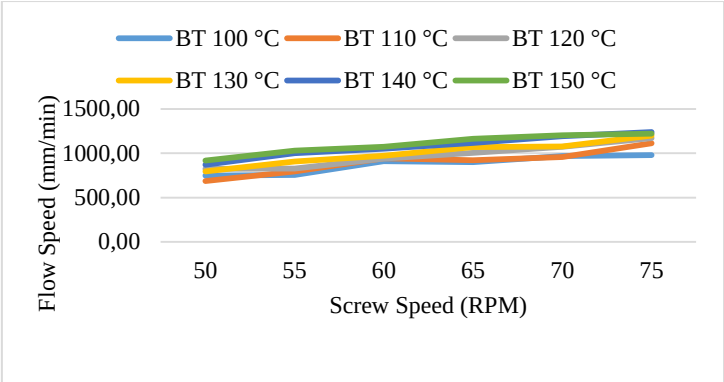

Fig. 6. Effect of screw speed on flow speed.

Obtained results for diameter. The values of filament diameter were recorded at different locations of filament after and before extrusion. The average diameter of the

filament was then finalized as the actual diameter of the filament. Mitutoyo digital micrometer was used to measure the values at different locations.

Before deposition. The nozzle of 0.8 mm diameter is used in the present study, but the obtained diameter of the EVA extrudate was quite larger as compared to nozzle diameter. It was due to the considerable amount of swell in the extrudate during the extrusion. The diameter of the filament was varied in the range of 1.65 to 1.95 mm for barrel temperature (see Fig. 7) while for the screw speed, it was varied from 1.47 to 1.65 mm as shown in Fig. 8. The diameter trend line for barrel temperature goes direction upward while the trend line approximately goes downward for the screw speed. In general, extrudate diameter decreases with increase in barrel temperature for other polymers but in the current study, the trend line shows the opposite results with temperature. The reason might be the reduction in melt elasticity at colder temperatures, which lead to increment in the molecular disentanglement.

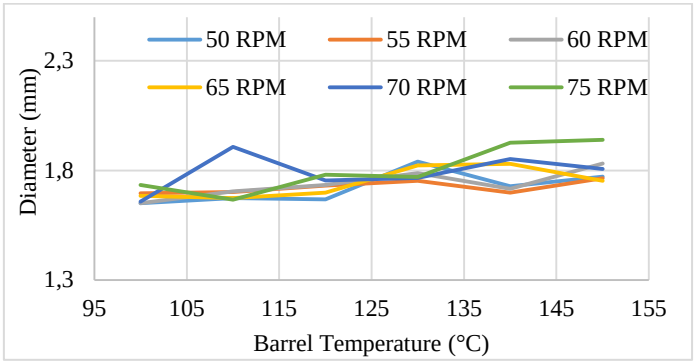

Fig. 7. Effect of barrel temperature on filament diameter before deposition.

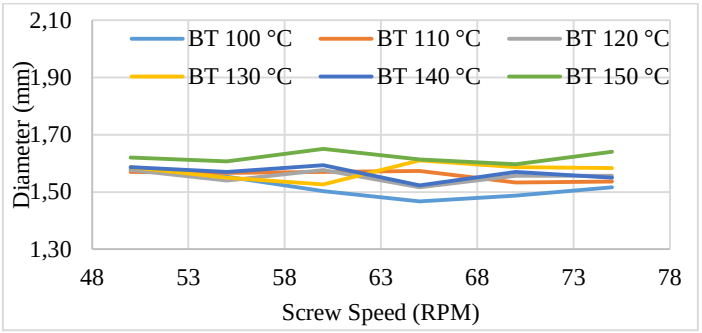

Fig. 8. Effect of screw speed on filament diameter before deposition.

After deposition. Elliptical shape filament was obtained after deposition onto the build platform due to the self-weight of the filament. Therefore, the value was recorded for maximum and minimum diameter. The maximum value was recorded as the filament width while the minimum value as filament thickness. The results for filament thickness and width are shown in Figs. 9 – 12 for screw speed and barrel temperature. It can be seen that filament width is increasing with the increase in barrel temperature while filament thickness is decreasing. Flowability of extrudate improves at high temperature due to a reduction in viscosity due to which extrudate flows and increase the filament width at the cost of filament thickness.

6. Part fabrication

Based on the experimental results, the optimum process parameters were selected as deposition speed 938 mm/min, barrel temperature 120 °C, screw speed 60 rpm, bed temperature 50 °C and layer thickness 1.42-mm. Different types of parts with different geometries were fabricated using these process parameters as shown in Fig. 13. It can be seen

that additive manufacturing of EVA is possible with developed CNC assisted MDT system and can be useful for various end-use applications such as shoe and soft robotics industries.

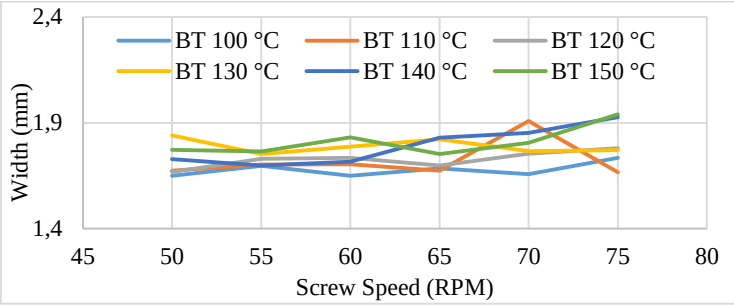

Fig. 9. Effect of screw speed on filament width after deposition.

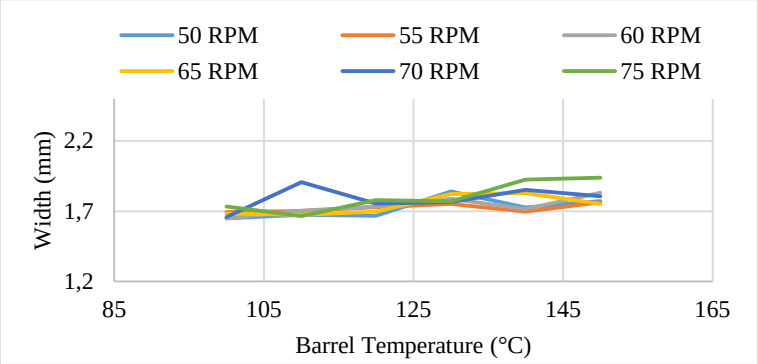

Fig. 10. Effect of barrel temperature on filament width after deposition.

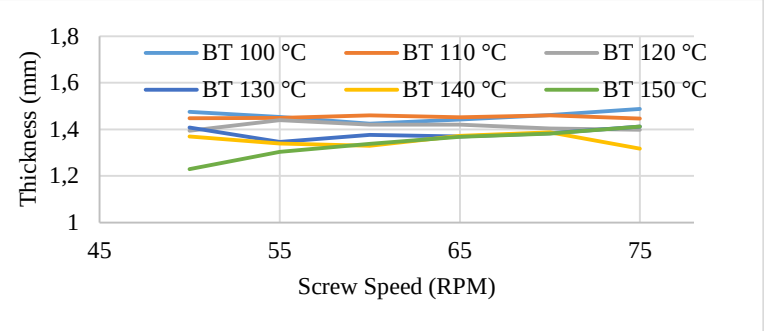

Fig. 11. Effect of screw speed on filament thickness after deposition.

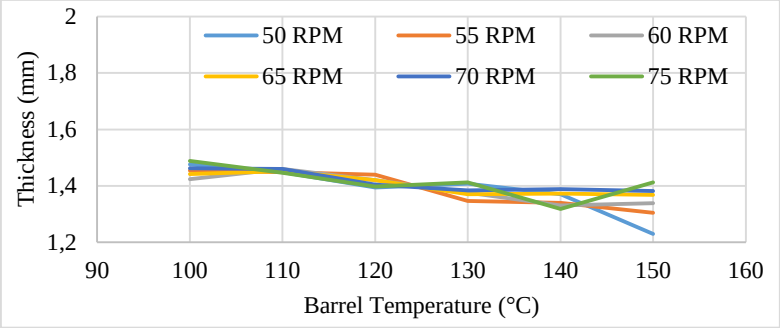

Fig. 12. Effect of barrel temperature on filament thickness after deposition.

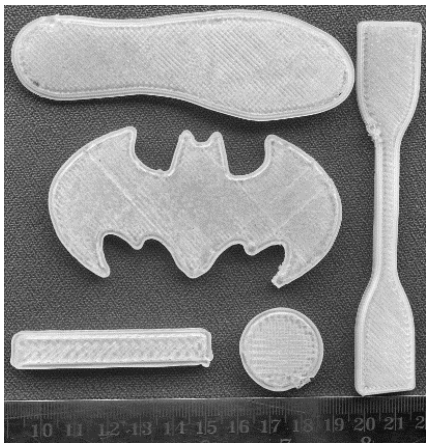

Fig. 13. Fabricated parts.

To show the part flexibility, a fabricated part was twisted manually as shown in Fig. 14. The twisting results show that EVA can twist similar to rubber and also can recover its original shape after removal of the load.

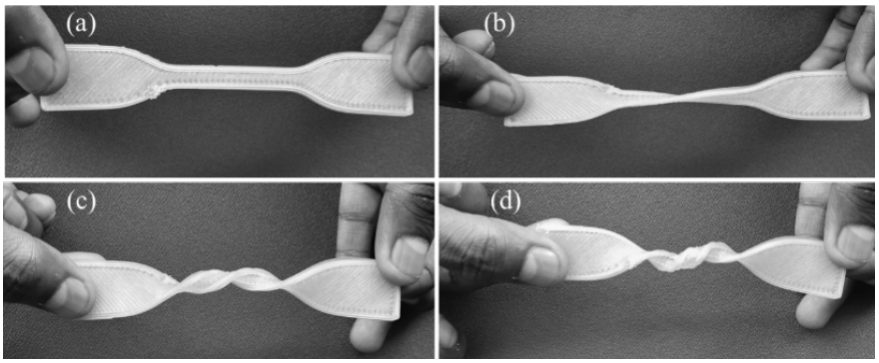

Fig. 14. Flexibility in fabricated parts.

7. Conclusion

The need of 3D flexible parts is very frequent in many industries. However, the fabrication of flexible parts through well-established FFF faces many issues. In the present work, flexible parts fabrication has been done using EVA material by developing an in-house CNC assisted MDT system. An exhaustive experimental study has been performed to determine the optimum process parameters setting. Screw speed and barrel temperature were considered as input process parameters while melt flow speed and filament diameter before and after deposition were considered as the measured responses. Based on experimental results, optimum process parameters were selected. Different types of 3D flexible parts were fabricated using the optimum process parameters. Overall, the current study indicates that flexible parts can be fabricated by developing pellet based AM systems with the ease. In future, many more materials and their composites can be explored on this type of systems.

Acknowledgment. *Authors would like to thank DST-SERB for providing financial support. Present work has been carried under the DST-SERB sponsored project "Development of Additive Subtractive Integrated RP System for Improved Part Quality" (SB/S3/MMER/0043/2013).*

References

[1] H. Bikas, P. Stavropoulos, G. Chryssolouris // *Int. J. Adv. Manuf. Technol.* **83(1–4)**

(2016) 389.
[2] M. Taufik, P.K. Jain // *J. Manuf. Sci. Eng.* **138(6)** (2016) 1.
[3] N. Kumar, S. Shaikh, P.K. Jain, P. Tandon // *Int. J. Rapid Manuf.* **5(2)** (2015) 186.
[4] S. Shaikh, N. Kumar, P.K. Jain, P. Tandon, *CAD/CAM, Robot. Factories Future* (Springer India, 2016) 751.
[5] M. Taufik, P.K. Jain // *Int. J. Manuf. Technol. Manag.* **27(1/2/3)** (2013) 47.
[6] B.N. Turner, R. Strong, S.A. Gold // *Rapid Prototyp. J.* **20(3)** (2014) 192.
[7] N. Venkataraman, S. Rangarajan, M.J. Matthewson, B. Harper, A. Safari, S.C. Danforth, G. Wu, N. Langrana, S. Guceri, A. Yardimci // *Rapid Prototyp. J.* **6(4)** (2000) 244.
[8] S. Masood, W. Song // *Mater. Des.* **25(7)** (2004) 587.
[9] M. Nikzad, S.H. Masood, I. Sbarski // *Mater. Des.* **32(6)** (2011) 3448.
[10] O.S. Carneiro, A.F. Silva, R. Gomes // *Mater. Des.* **83** (2015) 768.
[11] K.S. Boparai, R. Singh, H. Singh // *Rapid Prototyp. J.* **22(2)** (2016) 217.
[12] M.L. Shofner, K. Lozano, F.J. Rodríguez-Macías, E.V. Barrera // *J. Appl. Polym. Sci.* **89(11)** (2003) 3081.
[13] V. Francis, P.K. Jain // *Virtual Phys. Prototyp.* **11(2)** (2016) 1.
[14] B.H. Lee, J. Abdullah, Z.A. Khan // *J. Mater. Process. Technol.* **169(1)** (2005) 54.

Materials Physics and Mechanics 37 (2018) 133-139 Received: December 22, 2017

NONLINEAR OPTICAL CHARACTERISTICS OF ALBUMIN AND COLLAGEN DISPERSIONS WITH SINGLE-WALLED CARBON NANOTUBES

M.S. Savelyev[1,2]*, P.N. Vasilevsky[1], A.Yu. Gerasimenko[1,2], L.P. Ichkitidze[1,2], V.M. Podgaetsky[1], S.V. Selishchev[1]

[1]National Research University of Electronic Technology - MIET,

bld. 1, Shokin Square, Zelenograd, Moscow, 124498 Russian Federation

[2]I.M. Sechenov First Moscow State Medical University - MSMU,

bld. 2-4, Bolshaya Pirogovskaya, Moscow, 119991 Russian Federation

*e-mail: savelyev@bms.zone

Abstract. The interaction of laser radiation with aqueous dispersion of only bovine serum albumin (BSA) 25 wt. %, only bovine collagen (BC) 2 wt. %, and 25 wt. % BSA with single-walled carbon nanotubes (SWCNTs) 0.3 wt. % and 2 wt. % BC with 0.3 wt. % SWCNT was studied. The beam was absorbed mainly by nanotubes, that confirmed by the small value of the nonlinear absorption coefficients for aqueous dispersed media with BSA 6 cm·GW^{-1}, as well as dispersion with BK 4 cm·GW^{-1} and the large values of coefficients for these media with addition of SWCNTs, respectively 350 cm·GW^{-1} and 70 cm·GW^{-1}. Determination of nonlinear optical parameters was obtained by the method of fixed sample location. Knowledge of the values of these parameters allowed calculating theoretical curve of Z-scan with open aperture what made possible to compare with the experimental data.

Keywords: nonlinear optics; laser applications; three-dimensional printing; absorption.

1. Introduction

Laser printing of multilayered three-dimensional cellular- and tissue-engineered constructions with a structured internal scaffold is currently a promising task [1]. It is necessary to use bio-inks, which are capable of biodegradation, photo-cross-linking and providing sufficient strength of the formed structure for formation of constructions for bioengineering of human organs and tissues. Proteins that perform many functions are the most numerous organic substances in the human body, have high biocompatibility and biodegradability [2, 3] and are almost transparent in the visible range [4] are well suited for printing cellular and tissue-engineered constructions in solution of the practical challenges of laser surgery. Water dispersed media, containing only bovine serum albumin (BSA) 25 wt. %, only bovine collagen (BC) 2 wt. %, 25 wt. % BSA with single-walled carbon nanotubes (SWCNTs) 0.3 wt. % and 2 wt. % BC with SWCNTs 0.3 wt. % have desired properties. The printed samples on the basis of bio-inks with such a composition are able to ensure, during implantation, the germination of blood vessels through itself during the process of self-biodegradation [5]. Moreover, there is no hemolysis (the value of the hemolysis level is less than 0.5%), when blood contacts with such tissue-engineered constructions, which makes

http://dx.doi.org/10.18720/MPM.3722018_4

it possible to use them for the restoration of damaged heart tissues heart and blood vessels. The tensile strength and hardness of such multilayered three-dimensional constructions in the presence of a structured scaffold from SWCNT surpasses similar characteristics of porous human bone tissue [6].

In this paper, the main attention is paid to the investigation of the interaction of pulsed nanosecond laser radiation. Moreover, the intensity of laser radiation varies greatly so that the effect of light fluence on the formation of three-dimensional cellular and tissue-engineered constructions can be studied in detail. It is known that the effect of high-intensity laser radiation leads to the noticeable manifestation of nonlinear effects, when a certain threshold intensity is exceeded [7]. As a result, the energy, absorbed by the substance, can sharply increase, and this increase has a nonlinear character. Therefore, the study of nonlinear optical characteristics of proposed dispersion media was carried out to determine the optimal parameters of laser radiation for the formation of three-dimensional cellular and tissue-engineered structures.

At present, work is being carried out to create new photo-cross-linkable, biodegradable polymers for increasing the number of materials that are currently available for laser printing using laser sterolyolography (SLA) technology, which is very limited for choice [8, 9]. Another common method is digital light processing (DLP) [10]. Both of these techniques make it possible to fabricate tissue-engineered constructions from cell-saturated bio-inks, but differ in time, which is required for the formation of multilayered three-dimensional constructions [11]. In turn, the use of visible light instead of UV light reduces the potential risk of cells' DNA damage [12]. Therefore, in this paper, we studied the effect of laser radiation with a wavelength of 532 nm on the previously proposed in this paper composition for bio-ink.

The possibility of tissue-engineered structures formation by methods of laser printing make easier conducted procedures in laser surgery and simultaneously it improves the quality of these operations. That is why, it makes promising the development of this direction. This is achieved through the possibility of making implants of any anatomical shape, based on bio-inks. Using a laser can reduce the probability of infection due to a lack of the working surface contact with surgical instruments [13]. However, in comparison with the non-biological seal, it is necessary to solve a number of problems related to the sensitivity of cells and the choice of the correct layer design [14].

2. Materials

Aqueous dispersed media of BSA and BC proteins and similar dispersions with SWCNTs were investigated in this paper. The BSA and BC proteins were weighed in the form of a powder on an analytical weighing-machine AND HR-100A. After that, this amount of powder was mix with distilled water in proportions of 25 wt. % by weight and 2 wt. % by weight, respectively. The resulting dispersion was stirred on a magnetic stirrer for 30 minutes. SWCNTs were also mixed in the necessary concentration with distilled water and placed in "Sonicators Q700" homogenizer for 40 minutes. The power of the homogenizer was controlled by the program and was set to 60 – 65 W. The processing time of the dispersion with nanotubes was 30 minutes, the temperature did not exceed 70 °C. After reaching a homogeneous state, the dispersions were intermixed. The obtained dispersion of proteins with SWCNTs was processed by ultrasound for 30 minutes in the "Sapphire" ultrasonic bath. Before the experiment, the solution was additionally stirred on a magnetic stirrer for 10 minutes.

3. Experiments and methods for determining the nonlinear optical parameters of samples

In the course of the experiments, a nanosecond Nd: YAG laser was used, which generated radiation with a wavelength of 532 nm. The focal length of the lenses was 10 cm. The experimental apparatus used was described in detail in [15]. Based on the measured dependence of the normalized weakening coefficient K_{norm} from the input energy U_0 by the method of fixed sample location (direct nonlinear transmission), nonlinear optical characteristics of the prepared samples of proteins with SWCNTs such as nonlinear absorption coefficient, limiting threshold and maximum of weakening coefficient were calculated. In addition, this scheme allows one to make measurements of Z-scan with open aperture method. This method makes it possible to determine the nonlinear properties of the materials without changing the energy of the laser beam by varying its width, which leads to an increase in the light fluence of the beam [16, 17].

Unlike the Z-scan, during the direct nonlinear transmission experiment, the sample was placed in the focus of the lens and did not move during the study. The use of this method makes it possible to determine the linear α and non-linear β absorption coefficients and the threshold intensity I_c, without taking into account the change of the beam radius depending on the position of the sample in the mathematical model. Thus, there is a decrease in the number of variable parameters, which have an influence on the results of the experiment. As the result, it allows simplifying calculations that simultaneously increase accuracy of obtained results.

Dependence of the normalized weakening coefficient on the input energy of the laser beam was found by experiments with a fixed sample location:

$$K_{norm}(U_0) = \frac{K_{nonlin}(U_0)}{K_{lin}}, \tag{1}$$

where the value of the nonlinear weakening coefficient K_{nonlin} is calculated as

$$K_{nonlin}(U_0) = \frac{U_0}{U}. \tag{2}$$

The determination of the sample's nonlinear optical parameters from the known dependence of the transmitted energy U on the incident U_0 is described in detail in [18]. The value of the linear weakening coefficient K_{lin} is determined from the experimental data, obtained by the method of a fixed sample location with a laser radiation intensity not exceeding the threshold value. Knowing the nonlinear optical parameters of the sample, a theoretical Z-scan with open aperture curve can be calculated by the method described in [7]. The dependence of the light fluence on the distance from the center of the beam was determined by a technique that is described in detail in [15].

4. Results

The normalized weakening coefficient was increase with growth of input energy, but in aqueous dispersion of proteins without SWCNTs, this increasing was inconsiderable in comparison with dispersions containing SWCNTs. Fig. 1 shows experimental data, obtained by direct nonlinear transmission and theoretical curves.

The addition of nanotubes to the dispersion leads to a sharp growth of the nonlinear optical effects. The nonlinear absorption coefficient β was 6 cm·GW^{-1} and 4 cm·GW^{-1}, respectively, for the dispersions of BSA and BC, however, the same dispersions with SWCNTs showed much larger values of the nonlinear absorption coefficient (350 cm·GW^{-1} for BSA with SWCNTs and 70 cm·GW^{-1} for BC with SWCNTs). It should be noted that the linear absorption coefficient α also increased with the addition of SWCNTs, but the increase was small and had little effect on the value of the linear weakening coefficient K_{lin}. For

dispersions of BSA and BC, it was 1.92 cm^{-1} and 2.16 cm^{-1}, respectively, and 2.7 cm^{-1} and 2.91 cm^{-1} for the same dispersions with SWCNTs.

The limiting threshold for BSA and BC dispersions was 0.2 MW/cm^2 and 0.3 MW/cm^2, and for the same dispersions with SWCNTs, it was 1.8 MW/cm^2 and 0.9 MW/cm^2, respectively.

Knowledge of the values of these parameters allowed calculating theoretical curve of Z-scan with open aperture what made possible to compare with the experimental data (Fig. 2). Thus, the calculations, conducted with the help of the threshold model, was in good agreement with the values of the normalized weakening coefficient obtained experimentally. It was found that the behavior of the Z-scan with open aperture curve can be predicted, if the values of linear α and nonlinear β absorption coefficients, threshold intensity I_c, and the waist radius w_0, created by the lens, are determined.

The graphs show that the addition of SWCNTs to aqueous BSA and BC dispersions leads to a significant increase in the normalized weakening coefficient, i.e. to a sharp increase in absorption of laser radiation by the dispersion.

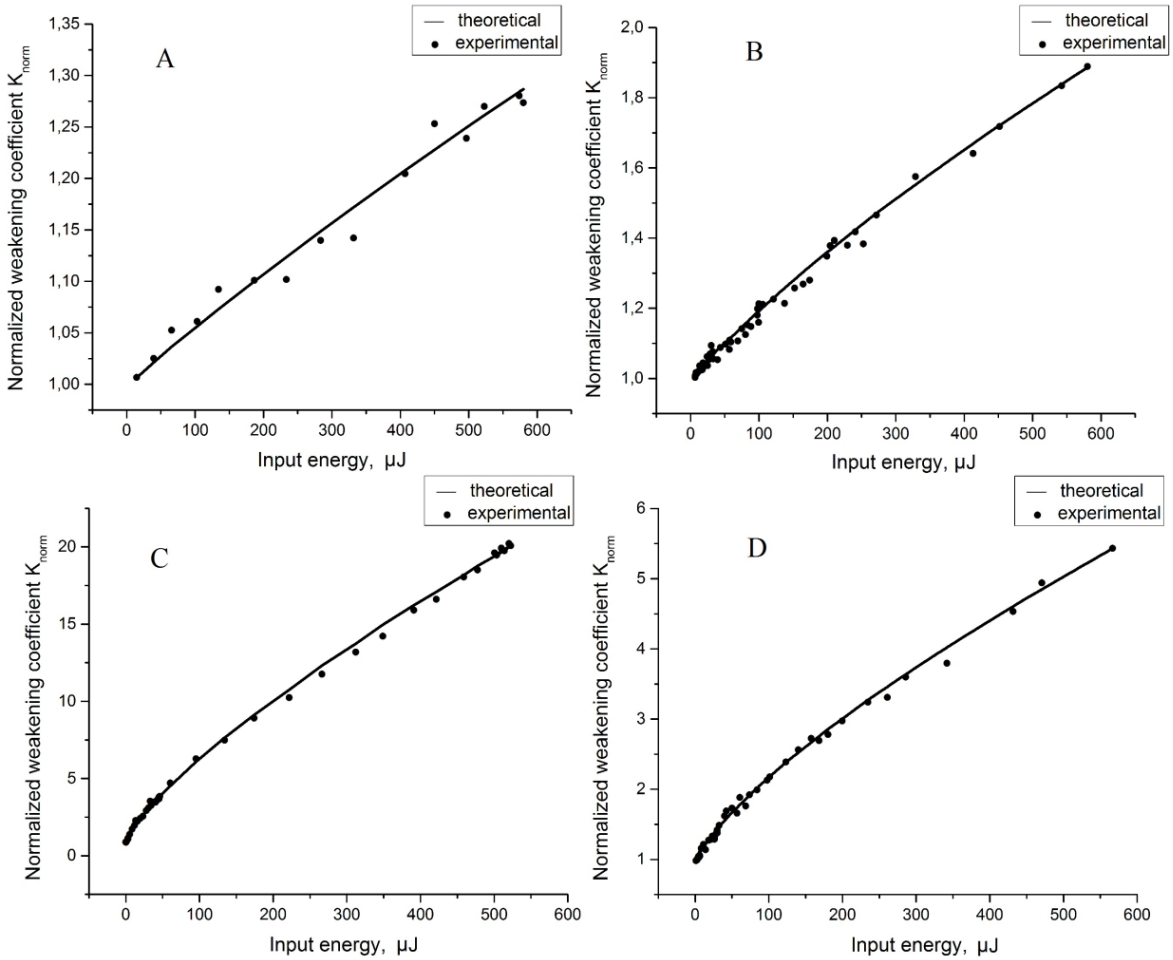

Fig. 1. Dependence of the normalized weakening coefficient on the input energy of the beam for aqueous solutions: (A) BSA (25 wt. %), (B) BC (2 wt. %), (C) BSA (25 wt. %) with SWCNT (0.3 wt. %), (D) BC (2 wt. %) with SWCNT (0.3 wt. %).

Figure 3 shows the dependence of the light fluence distribution on the distance from the center of the beam. In aqueous dispersions of BCs without SWCNTs, the waist radius was equal to 22 μm, and in the same samples with SWCNT was 23 μm. The calculated curves show that the greatest amount of energy is absorbed by the central region of the beam and the

absorption is greatly reduced, by approaching its edges. The light fluence distribution, which is shown in Fig. 3, is calculated for the position of the sample in the focus of the lens. Thus, these graphs show the minimum size of the laser spot.

5. Conclusion

The addition of SWCNTs to the aqueous dispersion of albumin and collagen proteins results in an insignificant increase in the linear absorption coefficient, which characterizes the passage of laser radiation at low laser radiation power and a sharp decrease of transmittance at high degrees. However, as the light fluence increases, a single pulse energy decreases sharply, which is characterized by a nonlinear absorption coefficient. This suggests that SWCNTs not only help create biodegradable forests, but also significantly increase the thermal effect of laser radiation.

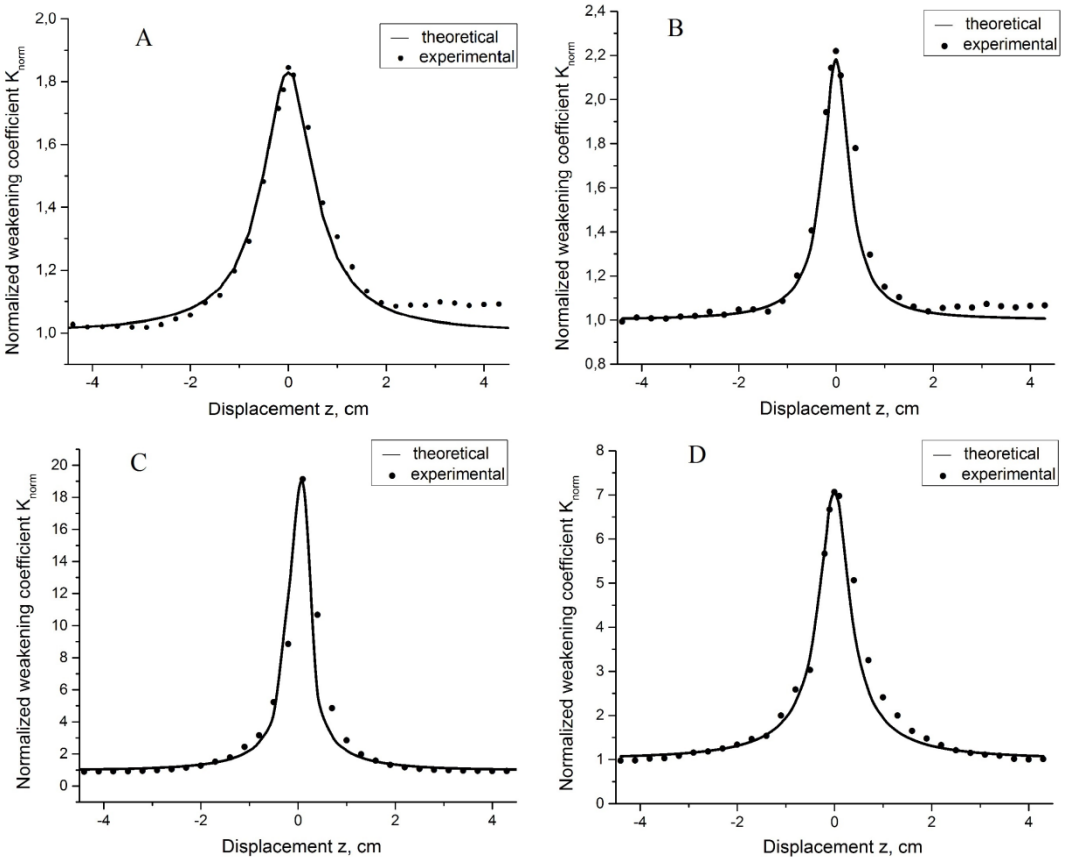

Fig. 2. Dependence of the normalized weakening coefficient on the position of the sample relative to the focus of the lens for aqueous solutions: (A) BSA (25 wt. %), (B) BC (2 wt. %), (C) BSA (25 wt. %) with SWCNT (0.3 wt. %), (D) BC (2 wt. %) with SWCNT (0.3 wt. %).

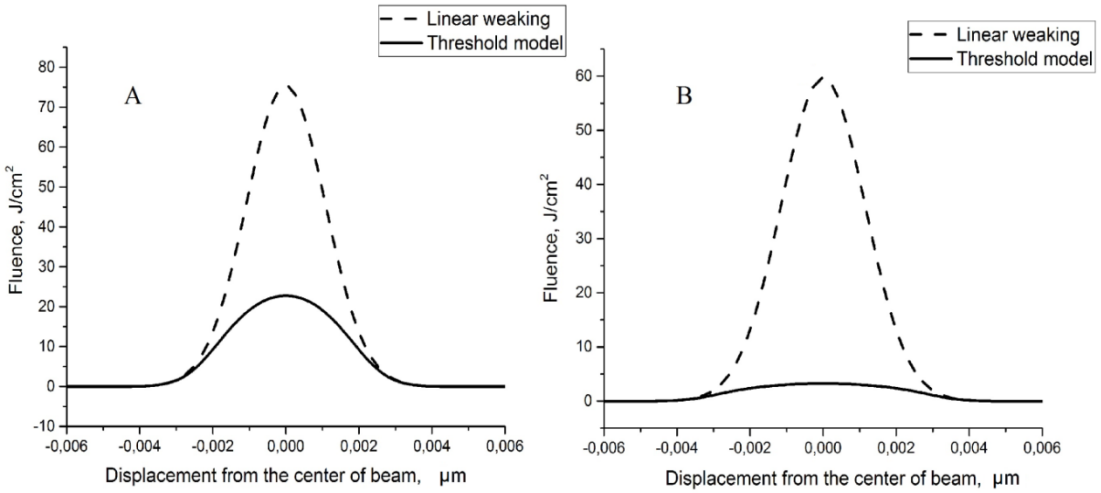

Fig. 3. Dependence of the light fluence distribution on the distance from the center of the beam for dispersions: (A) BC (2 wt. %), (B) BC (2 wt. %) with SWCNT (0.3 wt. %).

The use of nanosecond laser pulses with light fluence above the threshold values makes it possible to reduce the thermal effect on proteins, since the most radiation is absorbed by nanotubes during the formation of the scaffold. Thus, laser printing of multilayered three-dimensional cellular and tissue-engineered constructions with a structured internal nanocarbon scaffold with molecules of proteins such as albumin and collagen can be made. Subsequently, these constructions can be used for the implantation in the damaged area of the cardio-vascular system.

Acknowledgement. *This work was provided by the Ministry of Education and Science of the Russian Federation (Agreement 14.578.21.0234 RFMEFI57817X0234).*

References

[1] A. Skardal, A. Atala // *Annals of Biomedical Engineering* **43(3)** (2014) 730.
[2] A. Parag, J.B. Hall, C.B. McLeland, M.A. Dobrovolskaia, S.E. McNeil // *Advanced Drug Delivery Reviews* **61** (2009) 428.
[3] X. Liu, P.X. Ma // *Annals of Biomedical Engineering* **32** (2004) 477.
[4] S. Lousinian, S. Logothetidis // *Microelectronic Engineering* **84** (2007) 479.
[5] U.E. Kurilova, N.N. Zhurbina, M.V. Mezentseva, L.I. Russu, I.A. Suetina, I.V. Pyanov, D.V. Telyshev, A.Yu. Gerasimenko // *Biomedical Engineering* **51(1)** (2017) 16.
[6] L.P. Ichkitidze, S.V. Selishchev, A.Y. Gerasimenko, V.M. Podgaetsky // *Biomedical Engineering* **49(5)** (2016) 308.
[7] S.A. Tereshchenko, M.S. Savelyev, V.M. Podgaetsky, A.Yu. Gerasimenko, S.V. Selishchev // *Journal of Applied Physics* **120** (2016) 093109-1.
[8] L. Elomaa, C.-C. Pan, Y. Shanjani, A. Malkovskiy, J.V. Seppala, Y. Yang // *J. Mater. Chem. B* **3** (2015) 8348.
[9] B.K. Gu, D.J. Choi, S.J. Park, M.S. Kim, C.M. Kang, C.-H. Kim // *Biomaterials Research* **20(12)** (2016) 1.
[10] D. Dean, J. Wallace, A. Siblani, M.O. Wang, K. Kim, A.G. Mikos, J.P. Fisher // *Virtual Phys. Prototyp.* **7(1)** (2012) 13.
[11] F.P.W. Melchels, J. Feijen, D.W. Grijpma // *Biomaterials* **31** (2010) 6121.
[12] H. Ikehata, T. Ono // *Radiat. Res.* **52** (2011) 115.
[13] J.M. White, H.E. Goodis, C.L. Rose // *Lasers in Surgery and Medicine* **11** (1991) 455.
[14] S.V. Murphy, A. Atala // *Nature Biotechnology* **32(8)** (2014) 773.

[15] A.Yu. Tolbin, M.S. Savelyev, A.Yu. Gerasimenko, L.G. Tomilova, N.S. Zefirov // *Phys. Chem. Chem. Phys.* **18** (2016) 15964.
[16] R.K. Choubey, S. Medhekar, R. Kuma, S. Mukherjee, S. Kumar // *Journal of Materials Science: Materials in Electronics* **25(3)** (2014) 1410.
[17] W. Song, C. He, W. Zhang, Y. Gao, Y. Yang, Y. Wu, Y. Dong // *Carbon* **77** (2014) 1020.
[18] S.A. Tereshchenko, V.M. Podgaetskii, A.Yu. Gerasimenko, M.S. Savel'ev // *Quantum Electron* **45(4)** (2015) 315.

Materials Physics and Mechanics 37 (2018) 140-145 Received: December 22, 2017

ELECTRICAL CONDUCTIVITY OF THE NANOCOMPOSITE LAYERS FOR USE IN BIOMEDICAL SYSTEMS

L.P. Ichkitidze[1,2]*, A.Yu. Gerasimenko[1,2], V.M. Podgaetsky[1], S.V. Selishchev[1], A.A. Dudin[3], A.A. Pavlov[3]

[1]National Research University of Electronic Technology, bld. 1, Shokin Square, Zelenograd, Moscow, 124498, Russia

[2]I.M. Sechenov First Moscow State Medical University, bld. 4, Bolshaya Pirogovskaya Str., 2, Moscow, 119991, Russia

[3]Institute of Nanotechnology and Microelectronics of the Russian Academy of Sciences bld. 11, Nagatinckaia Str., 16a, Moscow, 115487, Russia

*e-mail: ichkitidze@bms.zone

Abstract. Nanocomposite layers consisting of an acrylic paint and single-walled carbon nanotubes (~1.5 wt.%) have been investigated. The investigated samples had a disk shape with a diameter of 20 – 30 mm and a thickness of 2 – 50 μm. After exposure in water for 350 h, the layer mass remained almost invariable (a mass loss of $\leq$ 1.5%) and the layer samples exhibited high adhesion to glass substrates and a conductivity of ~ 40 S/m. The layers consisting of the nanotubes and acrylic paint exfoliated from the substrates for ~1 h. After heat treatment at a temperature of 140 °C, all the layers exhibited a semiconductor-type temperature dependence of the resistance. The prospects of using these layers in various medical products, e.g. implants for wireless energy transmission, have been discussed.
Keywords: acrylic paint; carbon nanotubes; nanocomposite layers; electrical conductivity.

1. Introduction

Carbon nanotubes (CNTs) have the unique properties, including the high strength, electrical and thermal conductivities. The nanocomposites, containing CNTs, have the high potential of application in biomedical systems, since even a minor CNT content ($C \leq 2$ wt.%) leads to the unique properties of these materials.

Of particular interest are biomaterials and biocompatible materials with the low C values [1]. In a nanomaterial made of plasticized starch and multi-walled CNTs (MWCNTs), the double tensile strength and Young's modulus values were found [2]. The similar variation was observed in chitosan [3] and albumin [4 – 6]. Meanwhile, the nanomaterials were characterized by the minor C values: 2 wt.% in [3], 3 wt.% in [4], and $\leq$ 0.1 wt. % in [4 – 6]. A polymer (polyurethane) matrix, filled with MWCNTs, exhibited the percolation threshold at C = 0.13 wt.% [7, 8] and a carboxymethylcellulose (CMC) matrix, the percolation threshold at a level of C = (0.1 – 0.25) wt.% of MWCNTs [8].

In type-I collagen, a 2-wt.% single-walled CNT (SWCNT) addition increases the conductivity of the material by several orders of magnitude (to $\sigma \sim$ (1.2 – 1.6) S/m [9]); in carrageenan and chitosan with 0.6 wt.% of SWCNTs, the σ value increases by six orders of magnitude and attains 3200 S/m [10].

http://dx.doi.org/10.18720/MPM.3722018_5

In the combinations of various biological materials (hyaluronic acid, chitosan, heparin, gelatin, spermidine, albumin, carrageenan, CMC, etc.) and CNTs in a concentration of higher than 20 wt.%, the conductivities $\sigma \geq 1$ kS/m can be obtained at the preferred unidirectional CNT orientation. The high conductivities (σ ~ 50 kS/m) were implemented in the nanocomposite layers, consisting of a CMC matrix from a biocompatible material and MWCNT or SWCNT fillers (1 – 5 wt.%) exposed to laser radiation and treated at temperatures of ≥ 300 °C [8, 11]. The nanocomposites, based on biomaterials and biocompatible materials, most frequently demonstrated the conductivity values acceptable for the development of different medical devices (electrodes for electrocardiographs and electroencephalographs, implants, etc.). However, they are often unstable in water and moist environment [9 – 11], which strongly limits their application in medicine.

In this work, we investigate the electrical conductivity of nanocomposite layers consisting of an acrylic paint matrix, filled with SWCNTs.

In the present work, the electrical conductivity of layers of composite nanomaterials is investigated in the matrix – acrylic paint and filler – single-walled nanotubes.

2. Samples and experimental methods

Single-walled carbon nanotubes were formed by arc-driven synthesis and had a diameter of ~1.5 nm and a length of ≥ 1 μm [13]. The carboxylated (functionalized) SWCNTs in the form of a thick aqueous dispersion (paste) are offered for sale. Some of their parameters are given in Table 1.

Table 1. Some parameters of SWCNT.

Manufactures	NPF OOO "Uglerod ChG" [13]
View	Powder (purity ≥ 95 %)
Concentration of SWCNT	2.5 %
Density, g/cm^3	1.7 – 1.9
Bulk density, kg/m^3	0.1
Specific surface, m^2/g	~ 200 – 400

It can be seen that the SWCNT volume content is high (≥ 95%). It should be emphasized that the specific surface of individual SWCNTs is ~1300 m^2/g; however, since they are highly aggregated, their specific surface amounts to (200 – 400) m^2/g. Then, the average nanotube strands can attain 5 – 15 nm in diameter and 1 – 10 μm in length.

Figure 1 shows electron microscopy images of the layer consisting of only nanotubes. One can see different SWCNT strands with a maximum thickness of several tens of nm.

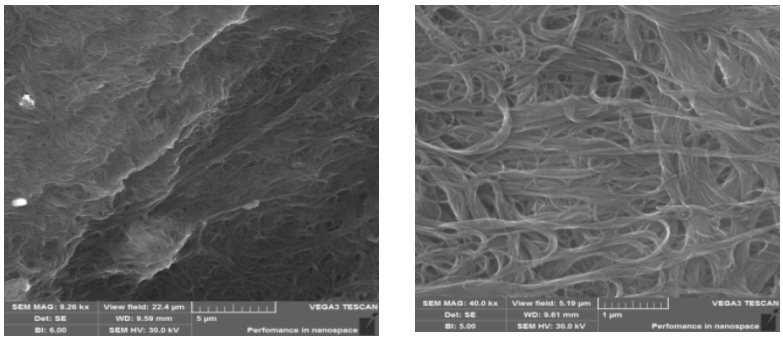

a *b*

Fig. 1. Electron-microscope images of films from SWCNT, scales: *a* – 5 μm; *b* – 1 μm.

The nanomaterial matrix was an acrylic paint (AP) (TU2331-034-05751640-2006) added with SWCNTs. The AP/SWCNT suspension was thoroughly mixed in a magnetic stirrer for 24 h and dispersed in a Qsonica Q700 ultrasonic disperser for 30 min. Before deposition onto substrates, the suspension was processed in an ultrasonic bath for 60 min.

The suspension contained 50 wt.% of the AP and 50 wt.% of the SWCNT paste and was characterized by the high viscosity (up to the glycerine level). The suspension was deposited by silk screening onto the substrates made of polyethylene terephthalan (PET, Petri dishes, or plates with thicknesses from 0.1 to 0.3 mm), and glass. The samples were disks with a diameter of 20 – 30 mm and a thickness of 2 – 50 μm. The typical samples, formed in a Petri dish, are shown in Fig. 2. The AP used had blue colour, so the layers prepared from the AP/SWCNT suspension acquired a black colour with a slight shade of blue.

The three sample groups were prepared: AP layers (group I), SWCNT layers (group II), and AP/SWCNT layers (group III). Three layers were deposited on the substrates of each type; each sample group included six sample layers.

It is important to estimate the composition of dried AP/SWCNT nanocomposite layers. For this purpose, we measured a solvent mass loss in the prepared layers, i.e., masses m_l and m_d of the indicated layers on glass and PET substrates in the liquid and dried states, respectively. The mass loss with respect to the mass in the liquid state (m_l) was determined as $m_w = (m_l - m_d)/m_l$. The obtained average values are m_w = 52% for group-I samples, 97.1% for group-II samples, and 51% for group-III samples. The SWCNT masses in the dried layers (100 – 97.1)% = 2.9% (group II), obtained by us, are similar to a nanotube relative mass of 2.5% in the paste, presented by the manufacturer (Table 1). Using the obtained m_w data, we found the dried nanocomposite layer composition to be 95 wt.% AP/5 wt.% SWCNTs.

Fig. 2. Appearance of AP/SWCNT layers in Petri dishes.

The dependence of resistance R on temperature t was measured in a thermostat in the temperature range of t ~ 20 – 200 °C. The temperature growth (drop) rate was controlled in the range of (0.5 – 1.0)°C/min. The specified temperature was held with an accuracy of ±1°C.

The sample resistance was measured by a two- or four-probe method. All the electrical measurements were performed in the current source mode. To do this, strip and square samples were prepared. The resistivity and conductivity of the samples were determined from their geometrical sizes and resistance.

3. Results and discussion

For all the sample groups, the layer mass loss was controlled after multiple immersions of the samples in water with the subsequent drying. The samples were immersed in water and kept there for 1, 12, 48, 96, and 192 h. Each time, the samples were taken from water, dried, and weighed. The total time of exposure in water was ~350 h. This experiment was carried out for

the layers deposited onto glass substrates. After ~1 h of exposure in water, the AP and SWCNT layers (group-I and II samples) exfoliated from the substrates, but the mass loss experiments were continued. The AP/SWCNT nanocomposite layers remained on the substrates throughout the experiment without changing the appearance and reducing the degree of adhesion to the glass substrates. The analogous behavior of mass loss in water was observed for the layers deposited on PET substrates.

The total layer mass loss relative to the initial mass after the last immersion and drying was 3% for group-I samples and 1.63% for group-III samples, while the layers of the group-II samples were completely destructed. Thus, the AP layers are easily destructed and lose their mass in water faster than the AP layers with small SWCNT additions (the nanocomposite 95 wt.% of AP/5 wt.% of SWCNTs). Meanwhile, the adhesion of the AP/SWCNT layers is higher than that of the AP layers.

Figure 3 shows breakage patterns of the AP/SWCNT nanocomposite layer. One can clearly see carbon nanotubes uniformly distributed in the bulk of the sample (Fig. 3a) and nanotube strands (Fig. 3b). Nanotubes are connected with each other, which can be important for the electric current flow in the investigated material.

The resistance variation with temperature for the group-I samples was not recorded, since their resistances were beyond the capability of a measuring device (200 MΩ). This value, recalculated to the conductivity with regard to geometrical sizes, was found to be ~10^{-4} S/m.

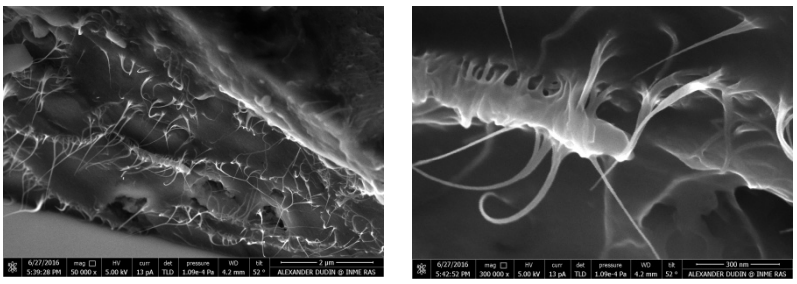

a *b*

Fig.3. Electron-microscopic images of the AP/SWCNT layer, scales: *a* – 1 μm; *b* – 300 nm.

Figure 4 shows typical temperature dependences of $R(t)/R_0$ for the group-II and III samples; $R(t)$ is the resistance variation with temperature and R_0 is the sample resistance at the beginning of heating. The values and qualitative behaviour of the curves depended on the measurement mode (heating or cooling). In particular, for group-II and III samples No. 1 on glass substrates, we obtained R_0 = 0.81 Ω and R_0 = 1016 Ω, respectively, at t = 22 °C (Fig. 4a). During heating, different behaviours of the curves are observed: metallic for the nanotube layers (group II) and semiconductor for the nanocomposite layers (group III). During cooling, the layers of both groups exhibit the semiconductor behaviour. In addition, the conductivities σ_0 of the samples, calculated from the R_0 data and geometrical sizes, were found to be strongly different: σ_0 ~ 20 kS/m for group-II samples and σ_0 ~ 15 S/m for group-III samples.

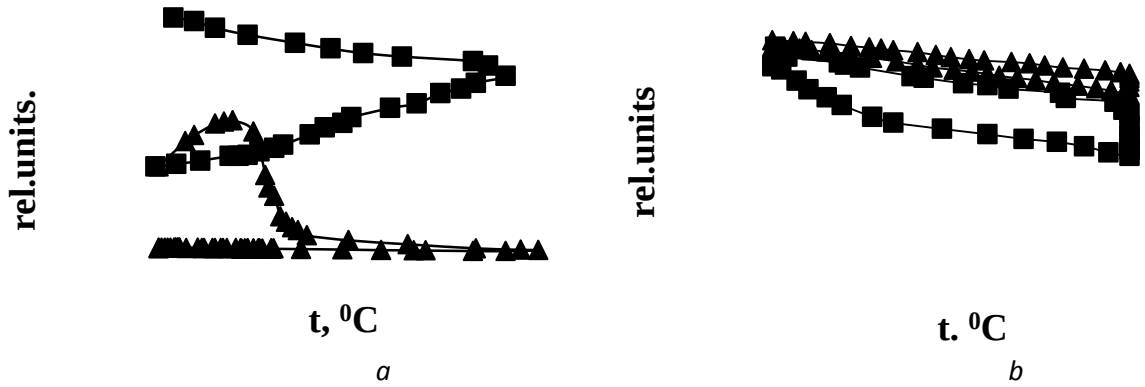

Fig. 4. Temperature dependences of the resistance of the layers: (a) sample No.1, the first heating, ▲ – AP/SWCNT layers, ■ – SWCNT; (b) sample 2, the third heating, annealing, cooling, ▲ – AP/SWCNT layers, ■ – SWCNT.

The $R(t)/R_0$ curves of the AP/SWCNT layers contain the maximum at a temperature of $t \approx 45$°C, which disappears during sample reheating or annealing. The similar maximum for the nanocomposite layers, containing MWCNTs, was attributed to structural defects, contained in nanotubes [14].

Figure 4b shows the $R(t)/R_0$ curves for group-II and III samples No. 2 on glass substrates at t = 23 °C and R_0 = 0.68 Ω (σ_0 ~ 25 kS/m, group II) and R_0 = 495 Ω (σ_0 ~ 40 S/m, group III). The layers were subjected to the second heating/cooling cycle. The samples of both these groups were held at t = 140 °C for 6 h, which is shown in the $R(t)/R_0$ curves by vertical lines. It can be seen that the resistance of the group-II layers increases by a factor of more than 3 and the resistance of the group-III layers decreases by ~20% relative to the initial R_0 values.

It should be noted that the value of σ_0 ~ 40 S/m for the AP/SWCNT nanocomposite layers (group III) differs from the value of $\sigma_0 \leq 10^{-4}$ S/m of the initial AP material (group I) by more than five orders of magnitude. The $R(t)/R_0$ hysteresis upon numerous heating/cooling cycles of the samples from this group is insignificant (Fig. 3b). In particular, the maximum hysteresis $2[R(\uparrow) - R(\downarrow)]/[R(\uparrow) + R(\downarrow)]$ is no higher than 8%. Here, $R(\uparrow)$ and $R(\downarrow)$ are the sample resistances with increasing and decreasing temperature, respectively. For both group-II and III layers, the $R(t)/R_0$ curves after the second and next heating/cooling cycles exhibited only the semiconductor-type behaviour similar to that shown in Fig. 4b for the AP/SWCNT layer. In this case, the $R(t)/R_0$ hysteresis of the SWCNT layers was significant (≥ 30%).

The $R(t)$ behaviour of σ_0 value (in the order of magnitude) for the group-II and III samples can be related to the following circumstance. The effect of temperature and heat treatment in air leads to the formation of defects and the contact resistance growth at the contact points between CNTs. This stimulates the resistance growth and changes the metal-type conductivity for the semiconductor-type one in the group-II layers (SWCNTs). The heat treatment of group-III (AP/SWCNT) layers apparently reduces the average thickness of tunnel contacts between nanotubes. In this case, the nanotubes are located inside the composite and not exposed to air. Consequently, the contact resistance between them and the resistance of the layer decreases. Indeed, the conductivity model of a matrix with randomly distributed CNTs explains qualitatively an increase in the matrix conductivity with a decrease in the contact resistance between nanotubes.

4. Conclusion

Thus, we experimentally investigated the electrical conductivity of nanocomposite layers with a thickness of 2 – 50 μm. The nanocomposite consisted of an acrylic paint matrix, filled with single-walled carbon nanotubes. The main results of this study are:

- the high degree of adhesion of the layers to the glass substrates and low mass loss after exposure in water for 350 h;
- the high conductivity limit (~ 40 S/m) at the low nanotube content (95 wt.% AP/5 wt.% SWCNT) in the layers, which is higher than the conductivity of the initial acrylic paint material by more than 5 orders of magnitude;
- a decrease in the layer resistance and change of the temperature dependence of the resistance for the semiconductor type upon multiple heating/cooling cycles and heat treatment at a temperature of 140 °C;
- insignificant (≤ 8%) hysteresis of the temperature dependence of the resistance upon multiple heating/cooling cycles.

The electrical conductivity of the material is a decisive parameter in operation of most modern systems and sensors. In view of this, the investigated conducting nanocomposite layers are promising for applications as functional nanomaterials. They can be used, for example, as biomedical electrodes for body electronics and electrocardiography, elastomers for general and biomedical purposes (strain gauges, artificial muscle, etc.), and electroconductive systems for wireless energy transmission in body implants.

Acknowledgement. *This work was provided by the Ministry of Education and Science of the Russian Federation (Grant 20.9216.2017/6.7).*

References

[1] J.M. Tan, P. Aruselvan, S. Fakurazi et al. // *Jour. of Nanomaterials* **20** (2014) 917024.
[2] X. Cao, Y. Chen, P.R. Chang, M.A. Huneault // *Journal of Applied Polymer Science* **106** (2007) 1431.
[3] S.F. Wang, W.D. Zhang , Y.J. Tong // *Biomacromolecules* **6(6)** (2005) 3067.
[4] L.P. Ichkitidze, S.V. Selishchev, A.Yu. Gerasimenko, V.M. Podgaetsky // *Biomedical Engineering* **49(5)** (2016) 308.
[5] S.A. Ageeva, V.I. Eliseenko, A.Yu. Gerasimenko, L.P. Ichkitidze et al. // *Biomedical Engineering* **44(6)** (2011) 233.
[6] L.P. Ichkitidze, V.M. Podgaetsky, O.V. Ponomareva, S.V. Selishchev // *Izvestia VUZov Fizika* **3/2** (2010) 125 (In Russian).
[7] R. Zhang, A. Dowden, M. Baxendale, T. Peijs // *Composite Science and Technology* **69(10)** (2009) 1499.
[8] L.P. Ichkitidze, V.M. Podgaetsky, A.S. Prihodko et al. // *Biomedical Engineering* **47(2)** (2013) 68.
[9] C.M. Voge, M. Kfriolis, R.A. MacDonald, J.P. Stegemann // *Journal of Biomedical Materials Research* **86A(1)** (2008) 278.
[10] A.J. Granero, J.M. Razal, G.G. Wallace, M. Panhuis // *Journal of Materials Chemistry* **20(37)** (2010) 7953.
[11] L.P. Ichkitidze, S.V. Selishchev, A.Yu. Gerasimenko et al., *Patent RU* 2473368, 27.01.2013 (In Russian).
[12] J.Xu, W. Florkowski, R. Gerhardt et al. // *J. Phys. Chem. B* **110** (2006) 12289.
[13] A.V. Krestinin, A.P. Kharitonov, Yu.M. Shul'ga et al. // *Nanotechnologies in Russia* **4(1-2)** (2009) 60.
[14] A.A. Babaev, A.M. Aliev, E.I. Terukov, A.K. Fillipov // *High Temperature* **55(4)** (2017) 502.

Materials Physics and Mechanics 37 (2018) 146-152 Received: December 22, 2017

MAGNETIC FIELD SENSOR FOR NON-INVASIVE CONTROL MEDICAL IMPLANTS

L.P. Ichkitidze[1,2]*, M.V. Belodedov[3], S.V. Selishchev[1], D.V. Telishev[1,2]

[1]National Research University of Electronic Technology,

bld. 1, Shokin Square, Zelenograd, Moscow, 124498, Russia

[2]I.M. Sechenov First Moscow State Medical University,

bld. 4, Bolshaya Pirogovskaya Str., 2, Moscow, 119991, Russia

[3]National Research University of Technology (BMSTU), ul. Baumanskaya, 2-ya, 5/1, Moscow, 105005 Russia

*e-mail: ichkitidze@bms.zone

Abstract. The magnetomodulation differential weak magnetic-field sensor, based on the Bi-2223 high-temperature superconducting ceramics has been investigated. The high magnetic-field resolution (~20 pT) and wide measurement range (125 – 140 dB) have been obtained. The possibility of using this sensor for noninvasive control of magnetic particles or implanted medical electronic devices in biological objects at a distance of up to 30 mm from the skin surface is discussed.

Keywords: high-temperature superconducting ceramic; magnetic-field sensor; magnetic-field resolution; noninvasive control; medical implants.

1. Introduction

Weak magnetic fields ($B \leq 10$ nT) are currently measured using different systems, including superconducting quantum interference devices (SQUIDs), combined magnetic field sensors (CMFSs), nuclear magnetic resonance laser pump magnetometers, and ferroprobe transformers (FTs) [1]. Among these systems, SQUIDs, which have been already commercially produced, have the highest sensitivity [2 – 4]. However, they are brittle, expensive, and do not detect the absolute value in the measured magnetic field.

The absolute value of magnetic field can be directly measured using FTs and CMFSs. The former, however, have serious drawbacks, specifically, the large measuring error in the weak-field range ($B \leq 1$ nT) and the narrow passband (≤ 1kHz) and dynamic measurement range $D_r \leq 60$ dB [5, 6]. The CMFSs still have been developed and tested [7 – 9], but in future their modifications containing nanosized elements can become competitive with SQUIDs [2 – 4].

A high-temperature superconducting (HTS) ceramic material investigated here consists of numerous grains with the Josephson junctions, formed between their boundaries. The magnetization curve (dependence of the magnetic flux ϕ on external field B) of such a Josephson medium is characterized by the strong nonlinearity, which increases near critical temperature T_c and was used to design the so-called magnetomodulation sensor (MMS) of weak magnetic fields ($B \leq 10$ nT). In the previous works, the MMSs were designed on the base of a Y-123 HTS ceramic material with $T_c \sim 90$ K. At a working temperature of $T \sim 77$ K (the liquid nitrogen boiling point), the $\phi(B)$ dependence of the Y-123 ceramics is strongly

http://dx.doi.org/10.18720/MPM.3722018_6

nonlinear; therefore, the sensor, fabricated from this material, is characterized by the high magnetic-field sensitivity $S = dU / dB$, where U is the response signal [10 - 13]. At the same time, the Y-123 ceramic-based sensors have certain drawbacks, e.g., the narrow measurement range ($|B| \leq 0.3$ mT), low magnetic-field resolution $\delta B \geq 50$ pT and magnetic-flux resolution $\delta\phi \geq 10\ \phi_0$ ($\phi_0 = 2.07 \times 10^{-15}$ Vb is the magnetic flux quantum), and the limited dynamic range ($D_r \leq 110$ dB). In addition, such sensors degrade in air under normal storage conditions. In contrast to the Y-123 ceramics, the Bi-2223 bismuth HTS ceramic material is stable and has $T_c \sim 105 – 108$ K [14]; therefore, MMSs based on it are expected to have the higher performances as compared with the Y-123-based sensor [12,13].

In this study, we investigate a weak magnetic-field sensor based on the Bi-2223 HTC ceramics with a working temperature of $T \sim 77$ K. The minimum size of iron magnetic grains that could be detected by the MMS under study is estimated.

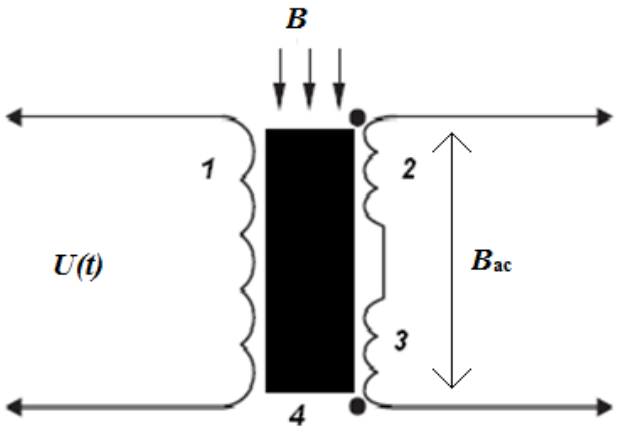

Fig. 1. Coils and core MMS: 1 – excitation coil, 2 and 3 – signal coils, connected in series and opposite to each other, 4 – cylindrical core of ceramic Bi-2223. The measured B is directed parallel to the z-axis, $U(t)$ is the registered variable signal.

2. Experimental

The main MMS element, i.e., a magnetic-field sensitive cylindrical rod, was fabricated from the Bi-2223 ceramic powder, which was tableted and annealed in accordance with the well-developed ceramic technology [14]. Cylindrical rods with a length of 18 – 20 mm and a dimeter of ~ 4 mm were cut from the prepared tablets. Two coils were tightly wound over almost the entire sample length (~16 mm); the exciting coil, consisting of two identical back-to-back sections each, containing 200 turns, was covered by a signal coil, containing 400 turns. The back-to-back identical halves of the exciting coil ensure operation of the investigated MMS in the differential regime, which automatically eliminates the effect of odd response harmonics on the signal winding. A superconducting cylindrical rod (sensor core) was positioned vertically along the z-axis; the x and y directions lied in the horizontal plane (Fig. 1).

All the measurements were performed in the geometry with the measured magnetic field $\vec{B}$ parallel to the z-axis of the cylindrical rod. Only the z projections of the background Earth's magnetic field B_b were taken into account, since the other two projections (x and y) of this field did not significantly affect the characteristics of the investigated MMS. The MMS

was mounted in a nitrogen cryostat so that the distance of the near sensor end to the outer cryostat surface was no larger than $d \sim 6 – 7$ mm.

The sensor rod had the low critical current density (≤ 10 A/cm^2) and $T_c \approx 105$ K. The measured weak dc magnetic field $\vec{B}$ was induced by the Helmholtz coils. All the measurements were performed at $T \sim 77$ K (liquid nitrogen temperature). The directions of field $\vec{B}$ and exciting magnetic field $\vec{B}_{ac}$ were collinear: $\vec{B} \| \vec{B}_{ac}$. The ac magnetic field was sinusoidal: $B_{ac} = B_m \sin(\omega t)$, where B_m is the amplitude, $\omega = 2\pi f$ is the cyclic frequency, f is the frequency, and t is the time. Sometimes, the field B_b was compensated to a level of ~1μT using the Helmholtz coils. The response signal U was detected by a selective nanovoltmeter with a selectivity of 40 dB/octave.

Figure 2 shows signals of the $U(t)$ response of the MMS to the exciting ac magnetic field with a frequency of f =10 kHz and an amplitude of $2B_m$ =1000 μT (peak–peak). The $U(f)$ dependences were recorded upon continuous variation in the frequency f. To exclude the sensor nonlinearity unrelated to its superconducting properties, the response was measured at room temperature $T \approx 300$ K (Fig. 2a).

It can be seen that in the normal state, all harmonics, except for the first one, are missing, which confirms the absence of unexpected nonlinearity of the sensor, which can be caused, e.g., by ferromagnetic parts of the sensor.

It follows from Figs. 2b and 2c that at $B_b \approx 1$ μT, the response contains only odd harmonics, while at $B_b \approx 50$ μT, all the harmonics are observed at T = 77 K. Such a behavior is typical of HTS ceramic materials and emphasizes their magnetic-field sensitivity. The higher harmonic amplitude decreased with increasing f and under voltages of ≤ 0.01 mV, the harmonics higher than the seventh order were not observed.

3. Results

Figure 3 shows a typical dependence of the second-harmonic amplitude U_2 on the applied dc magnetic field B.

It can be seen that the $U_2(B)$ dependence shifts along the horizontal axis by $B_b \sim 50$ μT (background Earth's magnetic field) and has the maxima at $B^* \sim \pm 700$ μT. The highest magnetic-field sensitivity $S_U = dU_2 / dB$ is attained in weak fields ($B \approx 0$). As the B value increases, S_U gradually decreases and at $B = B^*$ approaches the zero value. Thus, using the quasi-linear $U_2(B)$ dependence in weak fields $0 < B < 700$ μT, a high-sensitivity MMS can be designed on the basis of the Bi-2223 ceramics. It is worth noting that when the background Earth's magnetic field is compensated, i.e., at $B_b \leq 1$ μT, the S_U value additionally increases by more than 10%.

In the range of $|B| \leq 20$ μT, the $U_2(B)$ dependences are linear and the S_U value increases linearly with f. Indeed, it follows from Fig. 4 that S_U increases by a factor of 7.4 with a sevenfold increase in f.

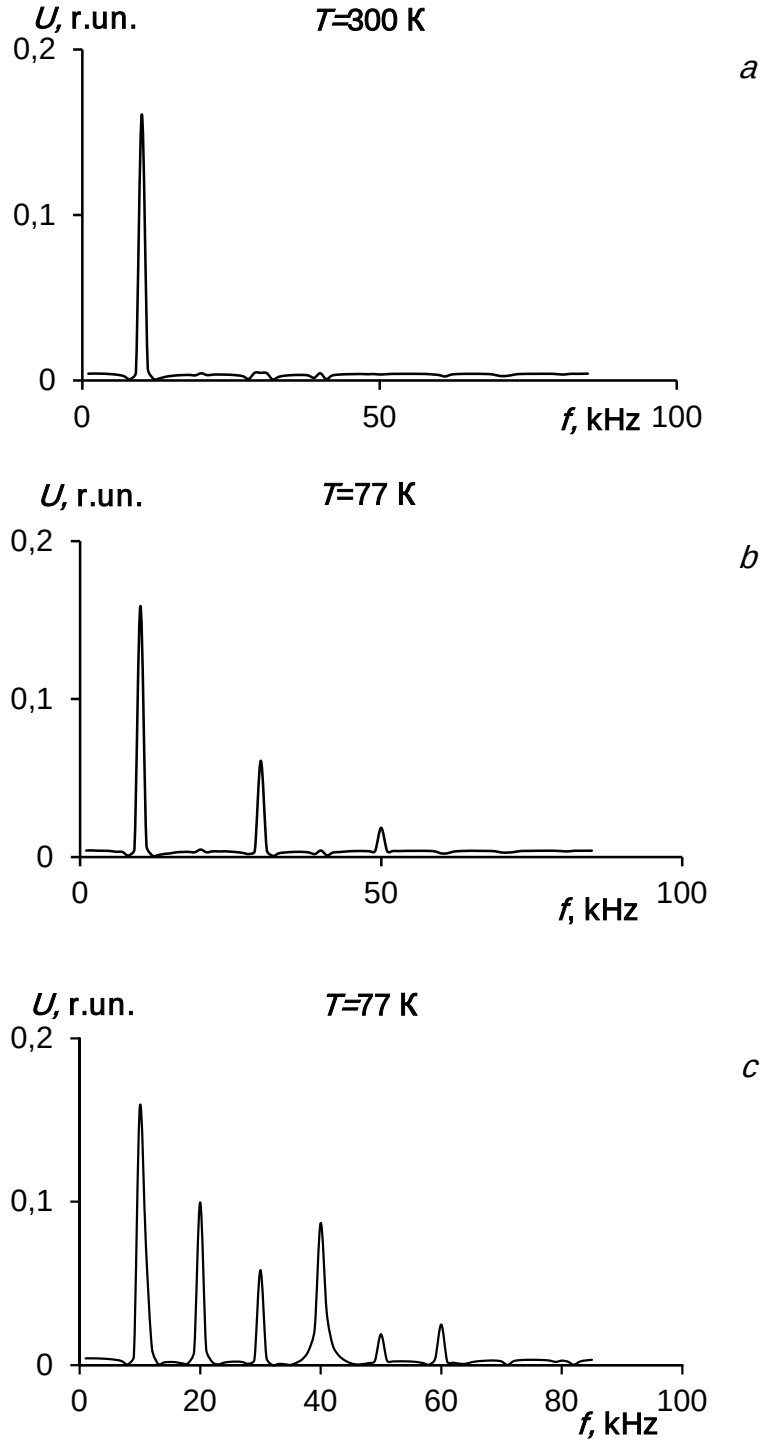

Fig. 2. Response U (relative units) of the sensor with f = 10 kHz and $2B_m$ =1000 μT (peak–peak) under different conditions: (*a*) T = 300 K, $B_b \approx 1$ μT; (*b*) T = 77 K, $B_b \approx 1$ μT; (*c*) T = 77 K, $B_b \approx 50$ μT.

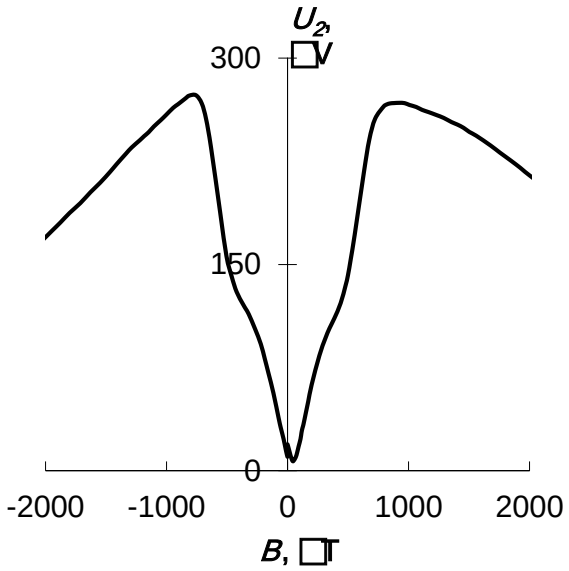

Fig. 3. Dependence $U_2(B)$ at f = 10 kHz and $2B_m$ = 600 μT (peak-peak). The background magnetic field of the Earth is uncompensated.

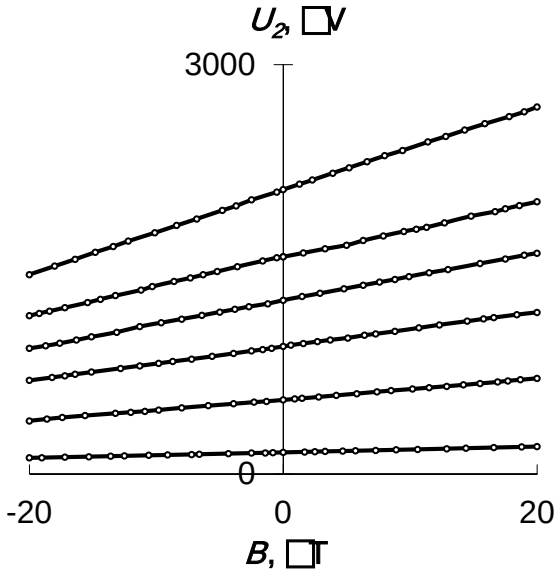

Fig. 4. Dependence $U_2(B)$ at $2B_m$ = 1000 μT (peak-peak) and various f, kHz (bottom-up): 5; 10; 15; 20; 25; 35. The background magnetic field of the Earth is uncompensated.

4. Discussion

The dependence of magnetic flux ϕ on field B in a superconducting rod is an odd nonlinear function and can be expressed in the first approximation as

$$\phi = A_0\left(k_1 B - k_3 B^3 - k_5 B^5\right), \tag{1}$$

where A_0 is the rod cross-sectional area and k_1, k_3, and k_5 are the coefficients.

In Equation (1), it is necessary to take into account all the investigated magnetic fields B, B_{ac}, and B_b in both halves of the exciting coil. Then, the ϕ value is

$$\phi = A_0\left[\left(k_{11}\left(B + B_b + B_{ac}\right) - k_{31}\left(B + B_b + B_{ac}\right)^3 - k_{51}\left(B + B_b + B_{ac}\right)^5\right) + \right.$$
$$\left. + \left(k_{12}\left(B + B_b - B_{ac}\right) - k_{32}\left(B + B_b - B_{ac}\right)^3 - k_{52}\left(B + B_b - B_{ac}\right)^5\right)\right], \tag{2}$$

where k_{11}, k_{12}, k_{31}, k_{32} , k_{51}, and k_{52} are the coefficients, characterizing the first and second coil halves, respectively. In Equation (2), only the z projections of the magnetic fields are taken into account, since the other projections are negligible.

The signal, induced in the receiving coil, consisting of n turns is

$$U = -n\frac{d\phi}{dt}. \tag{3}$$

According to (1) – (3), the signal response at the second harmonic is

$$U_2 \approx An\omega B_m^2\left[12k_{30}\left(B + B_b\right) + 20k_{50}\left(B + B_b\right)^3 + 10k_{50}\left(B + B_b\right)B_m^2\right]\sin\left(2\omega t\right) + u_2, \tag{4}$$

where u_2 is the unbalance signal and A is the average cross-sectional area of the signal coil. In Equation (4), we made the designations:

$$k_{30} = \frac{k_{31} + k_{32}}{2}; \quad k_{50} = \frac{k_{51} + k_{52}}{2}; \quad \Delta k_{10} = k_{11} - k_{12}. \tag{5}$$

The u_2 value tends to zero with a decrease in the difference between two halves of the core, i.e., when the quantities Δk_{10}, $\Delta k_{30} = k_{31} - k_{32}$, and $\Delta k_{50} = k_{51} - k_{52}$ turn to zero.

The thorough analysis of Equation (4) showed that at $B_b >> B$, $\Delta k_{50}/k_{50} \geq 1\%$, and $\Delta k_{30}/k_{30} \geq 1\%$, and a nanovolmeter selectivity of ~40 dB/octave, the u_2 value approaches the response at the second harmonic, which leads to a decrease in the magnetic-field sensitivity S_U. In the opposite situation, i.e., at $B_b \approx 0$, the u_2 value is minimum and the S_U value is maximum. This conclusion explains the obtained experimental result, i.e., the S_U growth after compensation of B_b.

According to Fig. 3, we have $S_U \sim 50$ V/T at $f \approx 35$ kHz and $B_b \approx 50$ μT. Taking into account the minimum detected signal level $\delta U_2 \sim 0.001$ μV, we obtain the minimum detected field $\delta B \approx \delta U_2 / S_U \sim 20$ pT. This value is not limited by the internal magnetic noise level $\delta B \leq 1$ pT of the Bi-2223 HTS ceramic material [15]. Hence, the magnetic-field sensitivity of the investigated MMS can be further enhanced.

The dynamic measurement range at $|B| \approx 20$ μT and $\delta B \sim 20$ pT is $D_r \sim 125$ dB and, in the case of $\delta B \sim 1$ pT, it is $D_r \sim 150$ dB. The total measurement range at $|B| \approx 600$ μT and $\delta B \sim 50$ pT is very wide and attains 140 dB.

The MMS is a differential sensor, the magnetic-field sensitivity of which can be increased in two ways: via increasing the ω, k_{30}, k_{50}, and B_m values or decreasing the external magnetic fields, including industrial noise and background Earth's magnetic field, and the Δk_{10}, Δk_{30}, and Δk_{50} values. For example, according to Equation (4), with an increase in the frequency f from 35 to 500 kHz, the $U_2(B)$ and S_U values grow proportionally; therefore, the δB value decreases to $\delta B \sim 1$ pT. In this case, the increase in the reactive resistance to a level of 1 Ω cannot significantly affect the MMS characteristics.

Thus, the magnetomodulation sensor, based on the Bi-2223 HTC ceramic material, exhibits a magnetic-field resolution of $\delta B \sim 20$ pT, which can be reduced to a level of 1 pT or lower.

Modern medical implants, sensors, and biocompatible materials often contain electronic components and conducting or magnetic particles. In particular, the implanted coils are used for wireless energy supply to various electrical implants, stimulators, artificial blood circulatory systems, etc. [16, 17], or carbon nanotubes and nanomaterials, based on them, containing catalytic magnetic particles [18, 19]. Detection of their magnetic fields will open the way to the noninvasive control of their operation.

The estimations made here showed that the investigated MMS with $\delta B \sim 20$ pT can detect weak magnetic fields of spherical magnetic particles ~100 μT in diameter at a distance of 10 mm from the sensor. At $\delta B \sim 1$ pT, the same particles can be detected at a distance of 25 – 30 mm from the near MMS end. In addition, magnetic particles, located under skin at a depth of 4 – 20 mm, can be detected ($d \sim 6 - 7$ mm). These estimations are apparently valid for various implants, located at a depth of up to 20 mm under the skin.

5. Conclusions

The investigated differential weak magnetic-field magnetomodulation sensor, based on the Bi-2223 HTC ceramic material, has a number of parameters typical of ferroprobe transformers, including the possibility of measuring the absolute value of the magnetic field,

simple design and fabrication, high magnetic-field sensitivity, and an accompanying electronic system. The sensor has the benefits of HTS SQUIDs, i.e., the high magnetic-field sensitivity and magnetic-field resolution (~ 20 pT) and wide measurement range (125 – 140 dB). The design simplicity and stability against degradation are certain advantages of the proposed sensor over the HTS SQUIDs.

These magnetometers can compete with the HTS SQUID magnetometers in, e.g., biomedical applications, such as noninvasive control of magnetic particles or various medical implants in biological objects.

Acknowledgement. *This work was provided by the Ministry of Education and Science of the Russian Federation (Grant 20.9216.2017/6.7).*

References

[1] D. Robbes // *Sensors and Actuators A: Physical* **129(1)** (2006) 86.
[2] www.tristantech.com
[3] www.starcryo.com
[4] www.supracon.com
[5] L. Jian // *Measurement* **46** (2013) 710.
[6] L. Jian // *Measurement Science Review* **12(6)** (2012) 286.
[7] M. Pannetier-Lecoeur, L. Pakkonen, N. Sergeeva-Chollet et al. // *Applied Physics Letters* **98(15)** (2011) 153705.
[8] L.P. Ichkitidze, A.N. Mironyuk // *Physica C: Superconductivity* **472(1)** (2012) 57.
[9] L.P. Ichkitidze // *AIP Advances* **3(6)** (2013) 062125.
[10] C.M. Wilson, G. Johansson, A. Pourkabirian et al. // *Nature* **479(7373)** (2011) 376.
[11] A.I. Golovashkin, N.D. Kuzmichev, V.V. Slavkin // *Technical Physics. The Russian Journal of Applied Physics* **53(10)** (2008) 1314.
[12] M.V. Belodedov, S.V. Chernih // *Instrum. and Experimen. Techniques* **44(4)** (2001) 568.
[13] V.K. Ignatev, S.V. Chernih // *Instrum. and Experimen. Techniques* **39(2)** (1996) 272.
[14] Y.E. Grigorashvily, L.P. Ichkitidze, N.N. Volik // *Physica C* **435** (2006) 140.
[15] B. David, D. Grundler, S. Krey et al. // *Supercond. Sci. Technol.* **9** (1996) A96.
[16] A.A. Danilov, E.A. Mindubaev, S.V. Selishchev // *Progress in Electromagnetics Research B* **69(1)** (2016) 61.
[17] A.A. Danilov, E.A. Mindubaev, S.V. Selishchev // *Progress in Electromagnetics Research M* **44** (2015) 91.
[18] L.P. Ichkitidze, V.M. Podgaetski, O.V. Ponomareva et al. // *Izvestia VUZov. Physika* **53(3-2)** (2010) 125 (In Russian).
[19] L.P. Ichkitidze, V.M. Podgaetski, A.S. Prihodko et al. // *Biomedical Engineering* **47** (2013) 68.

Materials Physics and Mechanics 37 (2018) 153-158 Received: December 22, 2017

LAYERS WITH THE TENSORESISTIVE PROPERTIES AND THEIR POSSIBLE APPLICATIONS IN MEDICINE

L.P. Ichkitidze[1,2]*, A.Yu. Gerasimenko[1,2], V.M. Podgaetsky[1], S.V. Selishchev[2]

[1]National Research University of Electronic Technology,

bld. 1, Shokin Square, Zelenograd, Moscow, 124498, Russia

[2]I.M. Sechenov First Moscow State Medical University,

bld. 4, Bolshaya Pirogovskaya Str., 2, Moscow, 119991, Russia

*e-mail: ichkitidze@bms.zone

Abstract. Layers of different materials, including nanocomposites, containing carbon nanotubes, with the tensoresistive properties are discussed. The investigated layers are divided into two groups: without (group I) and with carbon nanotubes (group II). A group-I material that is the most suitable for fabrication of a tensoresistor is the elastomer with microchannel, filled with a conductive liquid. In group II, these are the (0.2 – 10)-μm-thick layers consisting of the carboxymethylcellulose matrix, filled with multiwalled carbon nanotubes (~5 wt.%). The investigated layers can be used as alternative tensoresistors for medical applications.

Keywords: carbon nanotubes; carboxymethylcellulose; nanocomposite layer; tensoresistor.

1. Introduction

In medicine, it is often necessary to control limb, joint, chest, thorax, hydrops, tumors etc. movements and soft tissue strain, e.g., during post-surgery recovery. This is made using various strain gauges. The simplest and most wide-spread strain gauges are based on the phenomenon of resistance variation under strain and called tensoresistors. The strain sensitivity of these devices is determined as $S = \delta R/\varepsilon$, where $\delta R = \Delta R/R_0$, R_0 is the initial resistance, ΔR is the absolute resistance variation under strain, $\varepsilon = \Delta l/l$, l is the initial length of a sensitive element, and Δl is the absolute variation in its length.

Conventional tensoresistors are fabricated from metal or semiconductor materials. Meander-shaped tensoresistors formed from a metallic foil have the low temperature resistance coefficient ($\alpha \leq 10^{-5}\,K^{-1}$) and relatively wide strain measurement range ($\varepsilon = \pm 5$ %), but the low strain sensitivity ($S \leq 10$). Semiconductor tensoresistors are characterized by the high sensitivity ($S \sim 100 - 200$), very low strain ($\varepsilon \leq 0.2\%$), and high temperature resistance coefficient ($\alpha \geq 10^{-3}\,K^{-1}$) [1]. Note that both the metal and semiconductor tensoresistors have insufficient elasticity and strongly restrict movements of a biological object, because their moduli of elasticity E exceed the value characteristic of a human skin by several orders of magnitude ($E \sim (25 - 220)$ kPa, $\varepsilon >> 1$ %) [2].

In this work, we briefly describe different layers with the tensoresistive properties (hereinafter, tensoresistors) that were designed using original methods and/or materials and their potential applications in medicine. The investigated devices are divided into two groups. Group I is formed from the tensoresistors that do not contain carbon nanotubes (CNTs) and group II, from the tensoresistors, containing CNTs or based on nanocomposites with CNTs.

http://dx.doi.org/10.18720/MPM.3722018_7

2. Layers – Group I

A great number of tensoresistors have been developed and fabricated using nanoparticles and nanotechnologies. However, the high strain sensitivity ($S \geq 100$) is often attained in a very narrow strain range ($\varepsilon \leq 1$ %), which is not suitable for medical applications. Indeed, to control movements of human body parts, a strain of $\varepsilon \geq 10$ % is usually required. In [3], the materials, based on ZnO nanowires characterized by $S \approx 1250$ and $\varepsilon \leq 1$ %, were reported. In a hybrid material, consisting of ZnO nanowires, fixed on polysterene nano- and microfibers, the high ε values ($\leq$ 50 %) and relatively low S values (~100) were established [4]. A tensoresistor is encapsulated in a polydimethylsiloxane (PDMS) film and has the high moisture resistance. However, the excessively high resistance ($\geq 10^9$ Ω) and, consequently, high intrinsic noise level of the material significantly restrict the strain measurement accuracy.

The parameters $S \sim 10$ and $\varepsilon \sim (20 - 80)$ % were obtained in a tensoresistor, based on the thermoplastic elastomer, containing ~50 mass.% of soot [5]. The proposed sensor, however, rapidly loses its strain sensitivity ($S \leq 0.1$) at $\varepsilon \leq 10$ % and can probably be used to detect fabric strain.

The graphite layers deposited onto natural rubber substrates exhibit the tensoresistive effect with the high parameters: $S \sim 12 - 346$ and $\varepsilon \leq 246$ % [6]. Nevertheless, their $\delta R(\varepsilon)$ dependences are strongly nonlinear, especially in the range of $\varepsilon \geq 100$%. The strong nonlinearity of the $\delta R(\varepsilon)$ dependence is caused mainly by the behavior of pure rubber, i.e., by the strong nonlinearity of the stress induced during straining the rubber. Hence, the use of such layers as tensoresistors is complicated by the difficulty of brining the $\delta R(\varepsilon)$ curves to the linear shape with good accuracy.

In [7], an original tensoresistor consisting of a silicon elastomer with microchannels filled with a conductive liquid was developed to control movements of different human body parts. The strain (tension) increases the length and decreases the width of a microchannel and, thus, leads to the corresponding increase in its resistance. Testing of the tensoresistor showed that it has a strain of $\varepsilon \leq 300$ % and a sensitivity of $S \leq 3$ at bending angles of $\theta < 120°$; the strain measurement error was ~ 8 %. Obviously, this sensor is inapplicable to detecting movements of human body parts, where the angles can be in the range of $\theta \geq 120°$, e.g., in total finger, knee, or elbow flextions.

3. Layers – Group II

Carbon nanotubes (CNTs) have the unique properties, including high strength, heat and electric conductivity, and optical transparency. Nanocomposites with even minor (< 10 %) CNT additions acquire special characteristics. Depending on a fabrication technique used and nanomaterial composition, the tensoresistive effect in the CNT-based layers is either enhanced or suppressed. Indeed, the layers consisting of multiwalled CNTs (MWCNTs) added with $AgNO_3$ in a concentration of 2 – 10 g/l, deposited onto PDMS substrates, exhibit a stable resistance upon multiple bending in the angle range from −180° to +180° and have almost no tensoresistive properties [8].

Study of the MWCNT films, used as tensoresistors, showed the almost linear $\delta R(\varepsilon)$ dependence and absence of the hysteresis under loading and unloading in combination with the high stability of a signal, detected for 2-hour testing at $\varepsilon \leq 10$ [9]. Such a tensoresistor, however, appeared highly sensitive to various gases, moisture, and working temperature; i.e., it should be protected against environmental factors.

The tensoresistors in the form of thin films, containing aligned single-walled CNTs (SWCNTs) on flexible substrates, exhibit the excellent elasticity ($\varepsilon \sim 280$ %), but the very low sensitivity ($S \leq 0.8$), high hysteresis, and insufficient strain measurement accuracy [10].

A MWCNT film placed between natural rubber layers showed the higher strain sensitivity (S ~ 43) at ε ~ 620 % [6]. However, the $\delta R(\varepsilon)$ dependence for this film is approximately linear only at $\varepsilon \leq 100$ %.

A new type of the tensoresistor, based on SWCNTs, encapsulated in the PDMS layers, was proposed in [11]. The parameters of $S \leq 6.3$ and $\varepsilon \leq 10$ % and the moisture resistance higher than that of the tensoresistor without a protective layer were reported. For the MWCNT film-based tensoresistor, the linear $\delta R(\varepsilon)$ portions were observed at $\varepsilon \leq 0.1$ % and $S \leq 0.35$ [12]. A similar tensoresistor, based on grapheme, encapsulated between the PDMS films, showed the high sensitivity (S ~ 30), but the low ($\leq$ 1 %) ε value [13]. Such a tensoresistor can apparently be used for fragile (rigid) objects, but not in medicine, where the high strain ($\varepsilon \geq 10$ %) is needed.

The parameters suitable for monitoring the strain of human organs were obtained in different CNT/PDMS tensoresistor structures [14, 15]. However, these devices demonstrate the high nonlinear responses and hysteresis in combination with the insufficient elasticity. For these structures, we have E ~ 0.4 – 3.5 MPa [16 − 18], whereas epidermal applications require the materials with E ~ 25 – 220 kPa [2]). The modulus of elasticity of PDMS increases after adding CNTs; therefore, the discrepancy between elasticity values for human skin and the tensoresistor grows. In addition, absorption of water (moisture) by PDMS leads to the enhancing rigidity and aging. The material becomes fragile and its E value significantly increases over the modulus of elasticity of human skin. Indeed, to exactly detect human skin movements, it is necessary to use high-efficiency strain gauges, containing more elastic (soft) materials than PDMS. Many drawbacks of the tensoresistor, based on the CNT-containing film, encapsulated in the PDMS layers, were eliminated using the modified PDMS (the so-called Ecoflex silicone rubber). The CNT/Ecoflex PDMS tensoresistor is characterized by ε ~ 500 %, broad $\delta R(\varepsilon)$ linearity portions, and negligible hysteresis (ε < 150 %), as well as high stability and repeatability of a detected signal during multiple (~2000) loading/unloading cycles [19].

Both in the CNT/PDMS and CNT/Ecoflex PDMS structures, PDMS is polymerized by heat treatment at a temperature of 70 °C for 2 h. Certainly, this procedure complicates fabrication of the devices.

The thin (< 100 nm) SWCNT-containing films on flexible polyethylene naphthalate substrates exhibited the optical transparency and resistance variation with the bending angle θ [20]. The bending sensitivity $S_\theta = \delta R/\delta\theta$ was found to be ~0.08 %/deg at $\theta = \pm 180°$. Here, θ is the bending angle and $\delta\theta$ is the θ increment; at $\theta = 0$, there was no film bending.

The composite nanomaterials, containing CNTs, deserve high attention. For example, the films, consisting of polimethyl methacrylate (PMMA) matrix, filled with MWCNTs, exhibited a linear strain of $\varepsilon \leq 1$% at 0.75 wt.% of MWCNTs [21]. In [22], a 80-μm-thick buckypaper was fabricated from thermoplastic polyurethane (TPU) and MWCNTs and the value of $\varepsilon \approx 180$% at a ratio of 80:20 between TPU and CNTs was attained. The tensoresistor, however, had a very narrow region of the linear strain dependence of the output signal ($\varepsilon \leq 1$ %) and the low strain sensitivity ($S \leq 2$).

Study of many nanocomposites, included in epoxy polymers and CNTs, showed that with an increase in the MWCNT concentration between 1−10 mass.%, the conductivity σ increases from 10^{-2} to 10^{2} S/m and the S value decreases from ~22 to ~3 [23 − 25].

The layers, consisting of the carboxymethyl cellulose (CMC) matrix, filled with ~5 wt. % of MWCNTs, demonstrate the high conductivity ($\sigma \sim 10^4$ S/m), $\alpha \leq 10^{-5}$ K^{-1}, and S ~ 10 [26, 27]. Laser techniques and nanotechnologies make it possible to control the characteristics of a tensoresistor in wide ranges; in particular, the main parameter, i.e., conductivity, can be changed within $\sigma \sim 10^{-1} - 10^4$ S/m. The degradation testing of the

CMC/MWCNT layers showed no significant σ variations upon multiple bending of flexible substrates. In particular, upon layer bending by θ = ±180° with a bending radius of 1 mm for up to 10 cycles, the conductivity hysteresis was no larger than 20% relative to its initial value. The hysteresis decreased with increasing number of measurement cycles and was no larger than 8% after 300 cycles. The high strain sensitivity (S_θ ~ 0.80 %/grad) was demonstrated on the CMC/MWCNT nanocomposite layers with thicknesses of 0.2 – 10 μm. This is higher than the parameter of S_θ ~ 0.08 %/grad reported in [20]. The layers did not exfoliate from substrates upon multiple bending, did not crack, and kept their initial exterior.

Various strain gauges, containing CNTs, were reviewed in [28 − 31]. Their operation is based on the measurements of resistance or capacitance of strained layers. In the first case, these are tensoresistors and the presented examples can be added with our group-II sensors. In the second case, the gauges are capacitive and usually consist of three layers; the flexible layer is placed between two MWCNT layers. Despite the acceptable parameters (S_θ ~ 0.2 %/grad and ε ≤ 100 %), the repeatability of the characteristics is complicated.

Above we described some tensoresistors that are promising for medical applications. Of special importance is their use as miniature epidermic strain or pressure gauges for controlling the recovery after complex surgery and tactile sense recovery. The authors of [32] carried out investigations in this direction: they formed miniature skin pressure gauge prototypes using a 3D printer [32]. However, the direct contact of the strain gauge with the human skin surface is allowed only at the high biocompatibility. Certainly, this approach is valid for the above-mentioned tensoresistors, including those based on CNTs.

Since CNTs and CNT-based nanocomposites are relatively new materials, the health and ecology risks have been thoroughly investigated. Numerous experiments with CNTs revealed both positive and negative effects. The positive effects of CNTs are the possibility of vector drug delivery to different (including brain) organism parts [33 − 36] and neuron and neurite growth assistance [37, 38]. The negative effects are acceleration of the destruction of duplex DNA fragments [39] and blood thrombocyte aggregation [40].

By now, the following aspects, concerning CNTs, have been established [41 − 45]: (i) pure CNTs are more dangerous than functionalized ones; (ii) the CNT toxicity significantly weakens in a composite nanomaterial; (iii) the CNT toxicity is lower than the toxicity of asbestos particles; (iv) in a biological medium, oxidative fermentation and biodegradation of CNTs occur; and (v) citrullination in cells can be indicative of cytotoxicity of CNTs at the early diagnostic stages [46]. The bovine serum albumin molecules are adsorbed and uniformly cover the SWCNT surface layer by layer; bovine fibrinogen molecules behave similarly. Thus, the modified SWCNTs appear almost nontoxical [47 − 49].

4. Conclusions

The overwhelming majority of diagnostic and therapeutic devices and systems require various sensors, including strain gauges. In particular, they are used to control the recovery after surgical operations or test thigmesthesia. In this work, we discussed some types of the layers with the tensoresistive properties and possibility of designing original medical tensoresistors on their base. The analyzed materials were divided into two groups: without CNTs (group I) and with them (group II).

- The group-I device, the most promising for medical applications, is an original tensoresistor, which represents a silicone elastomer, containing microchannels, filled with a conductive liquid [7]. Such a tensoresistor detects small bendings (θ < 120°) of human body parts with an error of 8%.

- The group-II tensoresistors, which are based on thin films, containing aligned SWCNTs on flexible substrates, exhibit the excellent elasticity (ε ~ 280 %), but very low strain sensitivity ($S \leq 0.8$), high hysteresis, and low strain measurement accuracy [10]. The

MWCNT film, placed between the natural rubber layers, demonstrated the highest strain sensitivity (S ~ 43) at ε ~ 620 % [6]. However, their $\delta R(\varepsilon)$ dependences are approximately linear only at $\varepsilon \leq 100$ %.

- In many cases, the CNT films were encapsulated between flexible PDMS layers. The tensoresistors of this type exhibit the highest parameters, including the maximum strain of ε ~ 500 % and the approximately linear dependence of the relative resistance variation on ε in the range of ε < 150%, as well as the stability and repeatability of the detected signal upon multiple loading/unloading cycles (~ 2000) [19].

Nevertheless, the above-mentioned gauges cannot be directly laminated onto a complex curvilinear human skin surface to control the skin surface dynamics with high accuracy. This limitation is related to the fact that the PDMS polymerization requires heat treatment at temperature of 70 °C for 2 h.

- In epoxy nanocomposites, the high strain sensitivity (~22) is implemented at the low MWCNT concentration (~1 wt.%) [23 − 25].

- The layers based on a nanocomposite, consisting of CMC and MWCNTs, showed the quite acceptable parameters, i.e., the high electrical conductivity (10^{-1} – 10^{-4} S/m) and bending sensitivity of ~ 0.80 %/grad.

In most cases, the region of tensoresistor linearity should be broadened, which is a complex problem. To do this, it is necessary to take into account not only the substrate elasticity, but also transparency of tunnel contacts at the points of nanotube adjustment in the CNT-containing layers [50]. In some cases, the above-described tensoresistors have the characteristics suitable for applications in medicine. However, their safety at the lamination onto the human skin has still been investigated and the results of these investigations are of crucial importance [32]. In addition, it should be taken into account that the tensoresistors need to be protected from moisture, temperature, gases, and other effects during their operation.

Thus, the results obtained yield a promising outlook of fabrication of the tensoresistors containing carbon nanotubes or nanocomposites based on them.

Acknowledgement. *This work was provided by the Ministry of Education and Science of the Russian Federation (Grant 20.9216.2017/6.7).*

References

[1] http://www.hbm.ru/pic/pdf/1372416324.pdf
[2] X. Liang, S.A. Boppart // *IEEE Trans. on Biomedical Engineering* **57(4)** (2010) 953.
[3] J. Zhou, Y. Gu, P. Fei et al. // *Nano Lett.* **8(9)** (2008) 3035.
[4] X. Xiao, L.Y. Yuan, J.W. Zhong et al. // *Adv. Mater.* **23** (2011) 5440.
[5] C. Mattmann, F. Clemens, G. Tröster // *Sensors* **8(6)** (2008).
[6] S. Tadakaluru, W. Thongsuwan, P. Singjai // *Sensors* **14** (2014).
[7] Y. Menguc, Y-L. Park, E. Martinez-Villalpando et al. // *IEEE International Conference on Robotics and Automation, Karlsruhe, Germany, May 6-10.* (2013) 5309.
[8] D. Jiang // *EMSL Department of Microtechnology and Nanoscience (MC2)* (Chalmers University of Technology, SE-412 96 Gothenburg, Sweden, 2015), p.55.
[9] D. Jung, G.S. Lee // *Journal of Sensor Science and Technology* **22(5)** (2013) 315.
[10] T. Yamada, Y. Hayamizi, Y. Yamamoto et al. // *Nature Nanotechnology* **6** (2011) 296.
[11] Y. Liu, Q. Sheng, S. Muftu et al. // *Transducers, Barcelona, Spain, June 16-20* (2013) 1091.
[12] S.M. Vemuru, R. Wahi, S. Nagarajaiah, P.M. Ajayan // *J. Strain Analysis* **44** (2009) 555.
[13] Y. Wang, L. Wang, T. Yang et al. // *Adv. Funct. Mater.* **24** (2014) 4666.
[14] A. Mata, A.J. Fleischman, S. Roy // *Biomed Microdevices* **7(4)** (2005) 281.

[15] Q. Qin, Y. Zhu // *ACS Nano* **5(9)** (2011) 7404.
[16] Q. Fan, Z .Qin, S. Gao et al. // *Carbon* **50(11)** (2012) 4085.
[17] A. Mata, A.J. Fleischman, S. Roy // *Biomed Microdevices* **7** (2005) 281.
[18] J. Lu, M. Lu, A. Bermak // *7th IEEE Conf. on Nanotechnology, Hong Kong, China, August 2-5* (2007) 1240.
[19] M. Amjadi, Y.J. Yoon, I. Park *// Nanotechnology* **26** (2015) 375501.
[20] K.F. Akhmadishina, I.I. Bobrinetskii, R.A. Ibragimov et al. // *Inorganic Materials* **50(1)** (2014) 23.
[21] K. Grabowski, P. Zbyrad, A. Wilmanski, T. Uhl // *7th European Workshop on Structural Health Monitoring. La Cite, Nantes, France, July 8-11* **1** (2014) 1768.
[22] B. Ashrafi, K. Laqua, Y. Martinez-Rubi et al. // *31st Annual Technical Conference of the American Society for Composites. Williamsburg, Virginia, USA, September 19–22* **1** (2016) 307.
[23] N.Hu, Y.Karube, M.Arai et al. // *Carbon* **48** (2010) 680.
[24] G. Yin, N. Hu, Y. Karube et al. // *Compos. Mater.* **45** (2011) 1315.
[25] N. Hu, T. Itoi, T. Akagi et al. // *Carbon* **51** (2013) 202.
[26] L. Ichkitidze, V. Podgaetsky, S. Selishchev et al. // *Materials Sciences and Applications* **4(5A)** (2013) 1.
[27] L.P. Ichkitidze, V.M. Podgaetsky, A.S. Prihodko et al. // *Biomedical Engineering* **47(2)** (2013) 68.
[28] L. Weiwei // *FIU Electronic Theses and Dissertations* (2016) 3025.
[29] X. Li, C.A. Levy // *Sensors & Transducers Journal* **7** (2009) 5.
[30] Yu. Liu // *Electrical Engineering Dissertations* (2012) 156.
[31] A.A. Krechetov // *Vestnik Mashinostroenia* **8** (2015) 50 (In Russian).
[32] S-Z. Guo, Qiu Kaiyan, F. Meng et al. // *Advanced Materials* (2017) 1701218.
[33] E. Andreoli, R. Suzuki, A.W. Orbaek et al. // *J. Mater. Chem. B* **2(29)** (2014) 4740.
[34] E. Dillon, M.S. Bhutani, A.R. Barron // *J. Mater. Chem. B* **1B** (2013) 1461.
[35] H. Kafa, JT-W. Wang, N. Rubio et al. // *Biomaterials* **53** (2015) 437.
[36] J. Liu, F. Appiax, O. Bibari et al. // *Nanotechnology* **22(19)** (2011)195101.
[37] I. Bobrinetsky, A. Gerasimenko, L. Ichkitidze et al. // *American Journal of Tissue Engineering and Stem Cell* **1(1)** (2014) 27.
[38] N. Alegret, E .Santos, A. Rodriguez-Fortea et al. // *Chem. Phys. Lett.* **525-526** (2012) 120.
[39] S.H. Lacerda, J .Semberova, K. Holada et al. // *ACS Nano* **5(7)** (2011) 5808.
[40] B.M. Mohamed, D. Movia, A.Knyazev et al. // *Sci. Rep.* **3** (2013) 1124.
[41] B.L. Allen, G.P. Kotchey, Y. Chen et al. // *J. Am. Chem. Soc.* **31** (2009) 17194.
[42] C. Farrera, K. Bhattacharya, B. Lazzaretto et al. // *Nanoscale* **6** (2014) 6974.
[43] F.T. Andon, A.A. Kapralov, N. Yanamala et al. // *Small* **9** (2013) 2721.
[44] J.M. Tan, P. Aruselvan, S. Fakurazi et al. // *Journal of Nanomaterials* **2014** (2014) Article ID 917024.
[45] Y. Zhang, Y. Bai, B. Yan // *Drug Discovery Today* **15(11/12)** (2010) 429.
[46] B.M. Mohamed, D. Movia, A. Knyazev et al. // *Sci. Rep.* **3** (2013) 1241136.
[47] H. Haniu, N. Saito, Y. Matsuda, et al. // *Int. J. Nanomedicine* **9** (2014) 1979.
[48] A.Yu. Gerasimenko, A.A. Dedkova, L.P. Ichkitidze et al. // *Optics and Spectroscopy* **115** (2013) 283.
[49] L.P. Ichkitidze, M.S. Savelev, E.A. Bubnova et al. // *Biomedical Engineering* **49(1)** (2015) 36.
[50] O. Kanoun, C. Muller, A. Benchirouf et al. // *Sensors* **14** (2014) 10042.

Materials Physics and Mechanics 37 (2018) 159-167 Received: December 22, 2017

PIEZOELECTRIC BASED ENERGY HARVESTER EMBEDDED IN SHOE FOR WEARABLE ELECTRONICS

Sultan Singh, Vijay Kumar Gupta*, Sujoy Mukherjee

Mechanical Engineering Department, PDPM IIITDM Jabalpur, MP, 482005, India

*e-mail: vkgupta@iiitdmj.ac.in

Abstract. Piezoelectric based energy harvesting has become a popular research interest for last few years. This is due to the increasing demand for low-powered portable and wearable electronic devices such as health monitoring sensors. This paper presents two polyvinylidene fluoride (PVDF) based energy harvesters, which can be embedded in shoes to generate electric energy while human walking. One of the harvesters is specially designed as a sandwich structure, placed under the ball of foot, while the other one has curved or oval-shaped structure, placed under the heel of foot. Both harvesters are developed and deployed appropriately in the sole to couple maximum mechanical stress to the piezo-material and achieve high power output. The system was analysed, using mathematical modelling and results are verified by performing experiments in the lab. It has been observed experimentally that sandwich structured harvester produces 4.9 μW across a capacitor of 10 μF while walking at a speed of two step/second (2 Hz). However, for the same capacitor, the curve-shaped harvester produces up to 5.625 μW power. Integrated output power of both energy harvesters was 9.625 μW.

Keywords: piezoelectric; energy harvesting; PVDF; walking motion; smart materials.

1. Introduction

Energy harvesting technique has been an area of immense interest in research area of Harvesting energy from the energy sources such as heat, light, vibration and motion is an agreeable approach for acquiring the clean and sustainable energy. Energy harvested from vibrations and oscillations for instance low frequency vibration is the best method of energy harvesting [1]. The research motivation of this work is due to need of reduction in power requirement of low power consuming electronic devices, such as wearable and bio MEMS devices. A certain amount of electric current or voltage can be retrieved on application of mechanical strain on piezoelectric materials. Mechanical strain can be produced from different sources such as human body movements, seismic vibrations, machine bed vibrations and acoustic sound generally available everyday [2]. Two energy harvester designs using polyviyldine fluoride (PVDF) have been discussed in this work. One of the sandwiched structures is placed under the ball of the foot. Other one is curved shaped structure and placed under the heel of the foot. Modelling and experiments have been performed for both energy harvesters. Also, comparison of two polyvinylidene fluoride (PVDF) based energy harvesters have been done, which can be embedded in shoes to generate electric energy while human walking. In 2005 Sodano and Inman et al. [5] identified piezoelectric material as a tool for energy generation. They experimented the abilities of a circuit comprising a rectifier and a storage capacitor, when a steel ball impacted a plate bonded with PZT. In 2006 Sodano and Inman et al. [6] studied and developed a piezoelectric system to harvest the energy while

http://dx.doi.org/10.18720/MPM.3722018_8

human walking and power a 12-bit RFID at 310 MHz. They developed a PZT bimorph. The peak output power from that PZT bimorph in d_{31} bending mode under heal was 8.3 mW and from PVDF stave under toes was 1.3 mW.

Overview of Energy Harvesting System. The piezoelectric energy harvesting shoe system is able to harvest the energy from two points of contact during walking, which is shown in Fig. 1. The first point is the 'Contact Phase', which will obtain at the time of heel strikes during foot landing. At this point, energy is harvested by energy harvesting shoe system through compression of the piezoelectric material. The second point is the 'Propulsive Phase', which will obtain when the ball of the foot bends after landing the tip of the shoe to propel the person forward. The system consists of placing two piezoelectric (PVDF) energy harvesters at those two appropriate points for harvesting the maximum output energy.

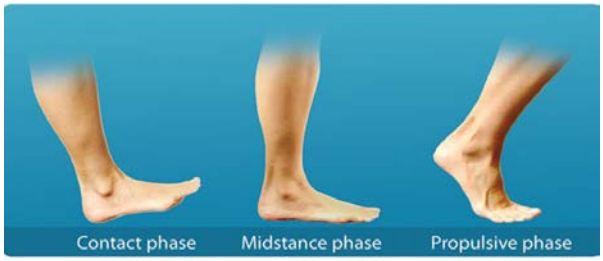

Fig. 1. Foot phase description while walking.

2. Design of sandwich type piezoelectric energy harvester

The main structure of this piezoelectric energy harvester is a sandwich type structure, where a multilayer Polyvinylidenefluoride (PVDF) film stack is sandwiched between two wavy surfaces [13]. One of these surfaces is a movable upper plate and other one is a fixed lower plate as shown in Fig. 2. Double PVDF film stack is fixed on the lower plate, and these PVDF Films are connected in series to obtain maximum output voltage.

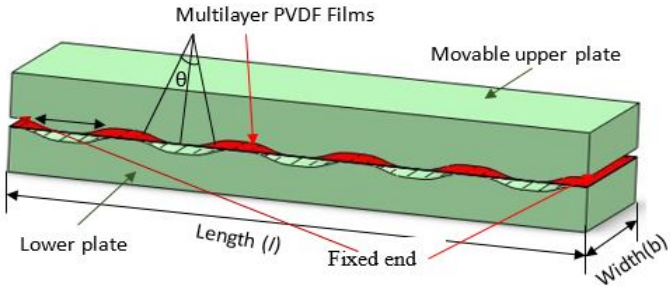

Fig. 2. Solid work model of energy harvester.

Working mechanism of energy harvester. The energy harvester works, when the upper movable plate of the piezoelectric energy harvester is subject to a compressive force, produced by human foot. The upper plate of energy harvester moves down and the PVDF film is stretched along the longitudinal (*1*-axis) simultaneously that is shown in Fig. 3. Due to stretching the PVDF film in longitudinal direction, strain is developed inside the film. This strain leads to a piezoelectric field inside every PVDF layer. The strain, developed in the PVDF film, drives the free electrons inside the each PVDF film. The external circuit is used to accumulate charge on the upper and lower surfaces of piezoelectric PVDF film, which has

the electrode. Then it induces the piezo potential in three-axis surfaces (electrodes) of every PVDF layer. When the foot force is released, then the upper movable plate moves up and the PVDF films relax and get original shape, therefore the piezopotential diminishes, and also releases the accumulated electrons on the surface of PVDF films. When human walks the dynamic force is produced by foot. This force acts on the upper plate that drives the electrons inside the piezoelectric layer surface and induces an alternating current (AC) output.

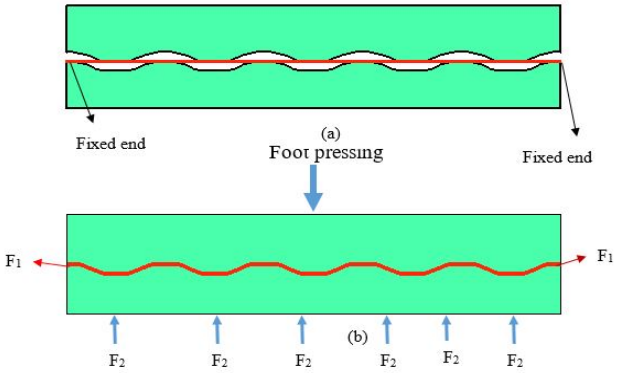

Fig. 3. Working mechanism of harvester.

The specially designed harvester's wavy surfaces are able to produce the large longitudinal deformation in the PVDF films and it reduces the thickness of piezoelectric energy harvester, which improves the energy harvesting performance and this harvester makes it possible to embed the harvester into a shoe.

Table 1. Design parameters of sandwiched type energy harvester.

Parameter name	Value	Description
L	70 mm	Harvester length or PVDF layer length
W	20 mm	Harvester width or PVDF layer width
T	28 μm	PVDF layer thickness
$A_1 = wt$	0.56 mm^2	Cross-section area of one PVDF layer
$A_3 = wl$	1400 mm^2	Three-axis surface area of one PVDF layer
N	2	Number of PVDF layers
l	11 mm	Chord length of arc-shaped groove
2θ	36°	Intersection angle of an arc-shaped groove
n = INT(l/L)	5	Number of arc-shaped groove

According to the elastic limit of the PVDF film, the design parameters of energy harvester have been developed (see Table 1). When movable upper plate moves down to the lowest position, both the tension of multilayer PVDF film F_1 and the resistive force F_2 against the upper plate, produced by (PVDF) film, reach maximum.

Mathematical modelling. Mathematical modelling of the harvester includes the equations for tension force F_1:

$$F_1 = NA_1\sigma_1, \tag{1}$$

where $\sigma_1 = \varepsilon_1 Y$ is the normal stress and for normal strain ε_1:

$$\varepsilon_1 = \left(\frac{\theta}{\sin\theta} - 1\right). \tag{2}$$

Equation (2) shows the dependence of the strain, generated in the harvester design, on the semi-intersection angle, θ [13], which is present in Fig. 4.

Since the elastic limit of PVDF is 2%, maximum permissible limit of θ is equal to 19.71°. Keeping a safety margin of 1.2 in the strain developed, for further analysis of θ, we adopted this limit as 18°. For simplicity of description, the frictions between the PVDF film and the wavy surfaces are ignored for calculating the resistive force.

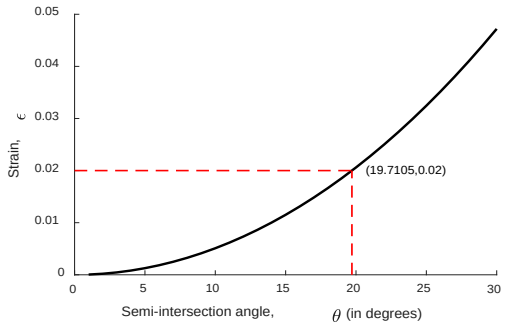

Fig. 4. Strain variation *vs* the semi-intersection angle of arc-shaped groove.

Resistive force F_2 is defined as:

$$F_2 = n \cdot 2F_1 \sin\theta = (l/L) \cdot 2NA_1\sigma_1 \sin\theta; \quad (3)$$

$$F_2 = 2Nwn(l/L)(\theta - \sin\theta)Y. \quad (4)$$

The constraint conditions for the design are presented as:

$$\varepsilon_1 = \left(\frac{\theta}{\sin\theta} - 1\right) \le \varepsilon_e; \quad (5)$$

$$F_2 = 2Nwn(l/L)(\theta - \sin\theta)Y \le \text{foot force}, \quad (6)$$

where ε_e is the elastic limit of the PVDF film, the value ranges of the above design parameters can be determined, based on the requirements of a specific design.

Energy extraction circuit. Power extraction circuit consists of two piezoelectric sources (MB10S), connected in series; rectifier with four Schottky diodes, used in high switching application; 1.2 MΩ resister and a 10 µF capacitor (see Fig. 5).

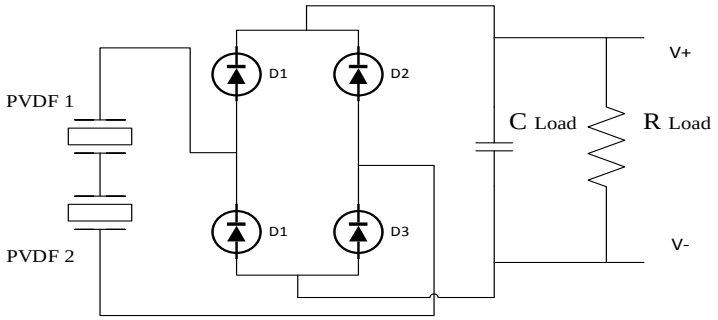

Fig. 5. Energy extraction circuit

Fabricated model of energy harvester. The fabricated model (see Figs. 6 and 7) consists of two rubber plates and two layers of PVDF films, glued with epoxy adhesive and sandwiched between two rubber plates therefore this harvester could be embedded under the foot force of shoe. The PVDF films have the electrodes and connection of PVDF films can be parallel and in series.

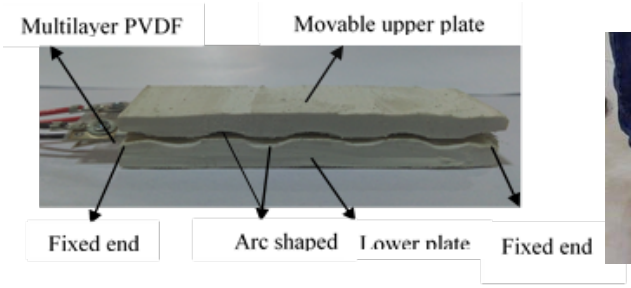

Fig. 6. Sandwiched structure.

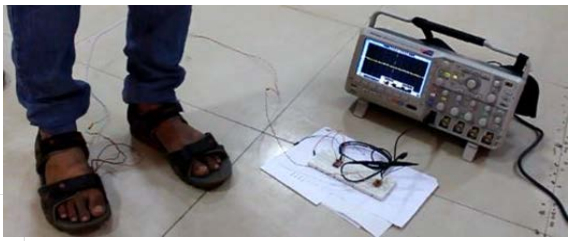

Fig. 7. Experimental setup.

Experimental results. In this experimental setup, a person of 60 kg weight wears the shoe/sandal and then walks at the speed of 2 steps per second (2 Hz).

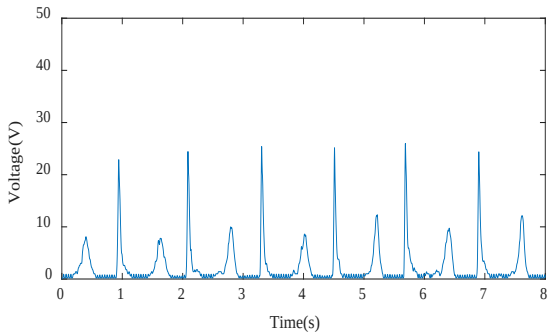

Fig. 8. Rectified voltage.

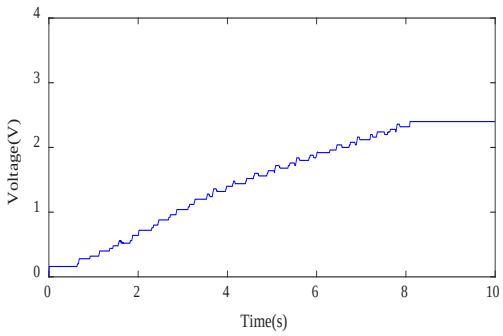

Fig. 9. Capacitor charging voltage.

Figure 8 shows the voltage across the 10μF storage capacitor. The capacitor will be fully charge after 15 steps and it induces approximately 2.5V DC output voltage (see Fig. 9).

3. Design and working mechanism of curved shaped piezoelectric energy harvester

When the piezoelectric energy harvesting device is pressed by external force in the middle, the PVDF and substrate are subjected to compressive and tensile stresses, respectively, therefore generating electric potential. In this harvester, the stress is produced in longitudinal direction and the electric field is generated in lateral direction. This curved piezoelectric generator consists of two separate curved piezoelectric generators, connected back-to-back, where each generator comprises a curved PI substrate and two polyvinylidene fluoride (PVDF) films [23]. The steel curved substrate is used to support the curved PI substrate and provide the appropriate flexibility during the human walking. The harvester consists of piezo 1 and piezo 2 which are made of PVDF and the electrodes of the both PVDF films are attached on both sides of the curved PI substrate, used in curved piezoelectric generator. Here, the curved piezoelectric energy harvester with top and bottom electrodes uses the d_{31} mode. This harvester can also use for other piezoelectric applications. The direction of the applied stress/strain is perpendicular to the induced electric field in this mode. Therefore, the induced voltage of the curve shaped piezoelectric generator can be calculated by using Equation (1).

Figures 10 and 11 shows the structure and working mechanism of the curved piezoelectric generator, where different stages of loading are shown: (a) initial state; (b, c) charge distribution during pressing; (d, e) charge distribution during force release; (f) three-dimensional schematic view of the curved piezoelectric harvester and wire connection of strained piezoelectric generator using high switching full wave rectifier.

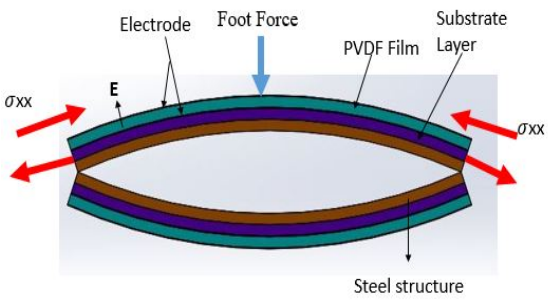

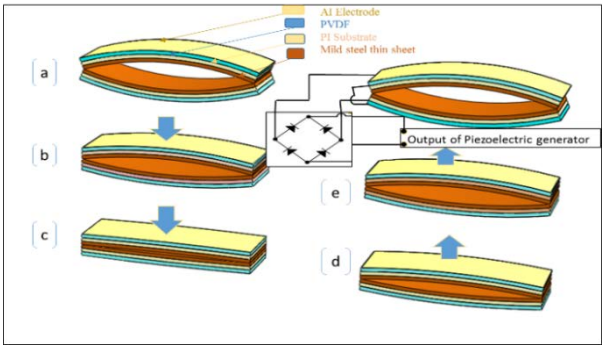

Fig.10. Model of curved structure. **Fig.11.** Work mechanism of curved energy harvester.

The curved shaped PI substrate structure of the curved piezoelectric power generator has two important roles. First, it effectively acts as a passive layer, when is subjected to the vertical force of the human. Since the PVDF film is very thin, it is unable to get the appropriate neutral plane of structure of piezoelectric generator and it also has a low Young's modulus. Therefore, PI substrate and steel substrate of the piezoelectric energy harvester should be appropriate thick to shift the neutral plane of the structure out of the piezoelectric PVDF film layer. On contrary, if the thickness of the piezoelectric PVDF film layer is very thick then the structure of energy harvester becomes more rigid, and subsequently it requires more force to generate the electric power. Secondly, the PI substrate also acts as an active layer that recovers the deformed piezoelectric PVDF film layer back into its original shape, like a leaf spring in a commercial automobile.

This harvester design also allows that the piezoelectric PVDF film is subjected to only tensile or compressive stress during the complete testing (pressing and releasing of human foot force). Because of this reason, the curved piezoelectric energy generator enhances the output power. This is because the proper thickness of the substrate layer makes the neutral plane shift from PVDF to its inside.

Mathematical modeling of curved piezoelectric harvester. When the piezoelectric energy harvesting device is pressed by external force in the middle of the device, the PVDF and substrate are subjected to compressive and tensile stresses, respectively, and voltage in 31 mode is defined as [23]

$$V_{31} = \sigma_{xx} g_{31} t\,, \qquad g_{31} = \frac{d_{31}}{\varepsilon_r \varepsilon^T}\,, \tag{7}$$

where, t is the piezoelectric PVDF film thickness, g_{31} is the piezoelectric voltage coefficient, d_{31} is the module of piezoelectric material and ε_r is the relative permittivity of PVDF.

The electric charge, induced on the surface of PVDF film by d_{31} mode is given as

$$Q = d_{31} C_{11}^E \int_A S_1 dA\,, \tag{8}$$

where A is the electrode area and C_{11}^E is the stiffness matrix of component. The charge, produced in piezoelectric generator, is a function of strain, induced in the generator. For an impact type piezoelectric energy generator, the quasi-static analysis gives better result. Therefore, charge equation of curved piezoelectric generator is given as

$$Q = b d_{31} C_{11}^E \left(\frac{t + t_1 + t_2}{3}\right) \int_0^l \frac{\partial^2 w}{\partial x^2} dx\,, \tag{9}$$

where b is the width of energy harvesting device and w is the z-components of displacement vector at a point on the neutral surface.

Table 2 presents design parameters of curved piezoelectric energy harvester.

Table 2. Design Parameters of curved piezoelectric energy harvester.

Parameter	Description	Value
t	PVDF film thickness	28 μm
t_1	Thickness of PI substrate layer	0.25 mm
t_2	Thickness of steel plate	0.15 mm
w	Displacement	10 mm
b	Width of harvester device	22 mm
L	Length of harvester device	72 mm

Fabricated model of energy harvester. Figure 12 shows a curved piezoelectric energy harvester, which is placed under the heel in the shoe/saddle. This harvester has two PVDF films, connected in series. The electrodes of the piezoelectric films are connected to power extraction circuit. Readings shows in the digital storage oscilloscope (Fig. 13).

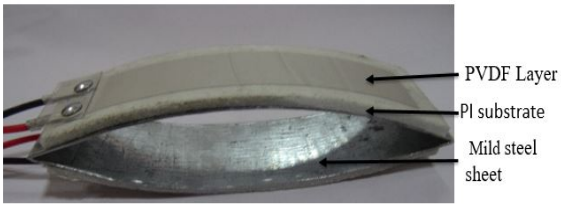

Fig. 12. Experimental model.

Fig. 13. Experimental setup.

Experimental results. In experiment, the harvester is appropriately placed in the shoe/sandal and the setup is worn on foot of a person with weight of 60 kgF. The person is then walks with the speed of approximately 2 steps/s.

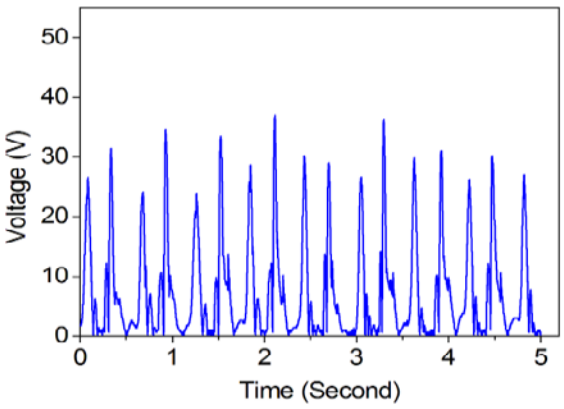

Fig. 14. Rectified voltage.

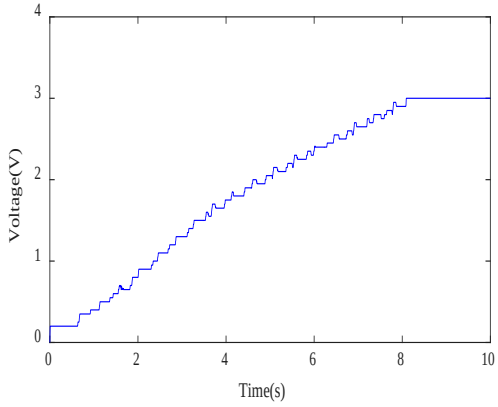

Fig. 15. Capacitor charging voltage.

Figure 14 shows the voltage across the 10 μF storage capacitor. The capacitor will be fully charge after 15 steps and it induces 3V DC output voltage (see Fig. 15).

4. Combination of both energy harvesters

While walking, the heel part of foot lands with much higher impact force. So in order to absorb this force effectively, the oval-shaped harvester was deployed as its structure can withstand wide range of deflection (see Fig. 16). Hence, the rapid deflection in the piezo-material resulted in high peaks of output voltage as apparent in Fig. 17. On the contrary, the forefoot is a flexible part, which experiences gradual load while walking. This makes it

suitable for low deflection applications. Moreover, the sandwich type harvester had been precisely designed to produce higher strain in PVDF film with low deflection in its structure. Therefore, it was placed under the forefoot for energy harvesting.

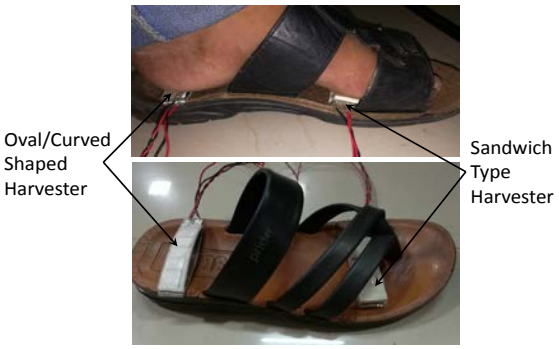

Fig. 16. Combination of both energy harvesters.

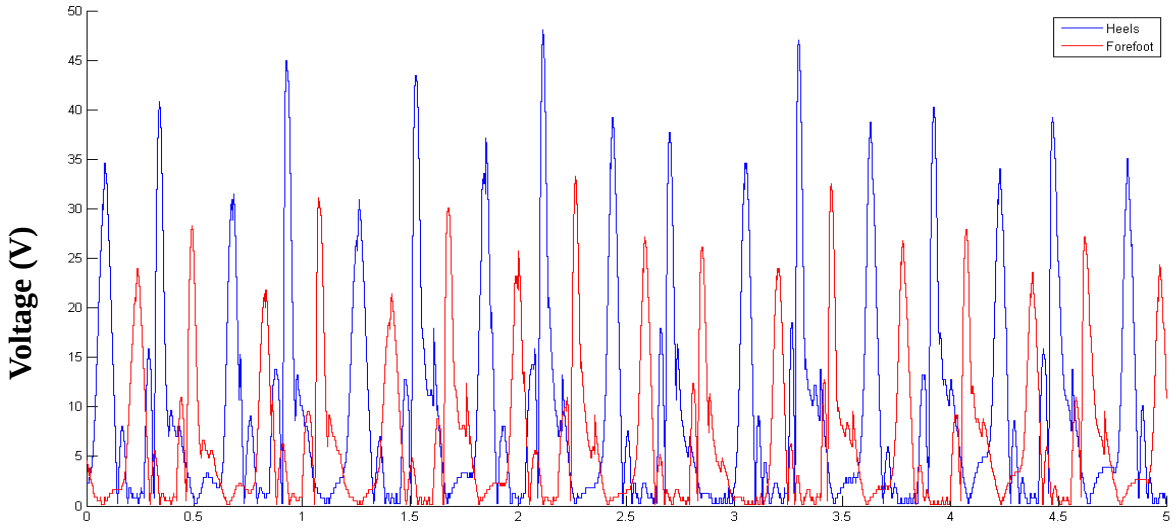

Fig. 17. Integrated Rectified voltage of combined energy harvester.

Firstly, the heel of foot makes contacts with ground and foot force gradually increases on the curved shaped structure. As steps progresses, the active force acting on this harvester decreases and shifts to the sandwiched type harvester placed under the fore-foot. This causes decay in voltage across the former harvester and increase in voltage across the latter.

5. Conclusions

The energy harvester, which is placed under the ball of foot, the rectified output voltage is obtained as 21 V and voltage across the 10 µF capacitor is obtained as 2.5 V. The output voltage across the capacitor is used to calculate the energy generation and generated output power is 3.9 µW. The energy harvester, which is placed under the heel of the foot, the rectified output voltage is obtained as 30 V. Output voltage across the 10 µF capacitor is obtained as 3 V and generated output power was 5.625 µW. The integrated average voltage output of the design is equal to 6.5 V. Subsequently, the average power output obtained was 9.625 µW.

References

[1] A.D. Kuo // *Science* **309** (2005) 1686.

[2] L.C. Rome, L. Flynn, E.M. Goldman, T.D. Yoo // *Science* **309** (2005) 1725.

[3] S.R. Anton, H.A. Sodano // Smart Mater. Struct. **16** (2007) 1.

[4] M. Renaud, P. Fiorini, R. Van Schaijk, H.C. Van // *Smart Mater. Struct.* **18** (2009) 035001.

[5] C.A. Howells // *Energy Convers. Manag*. **50** (2009) 1847.

[6] Y. Song // *J. Clin. Rehabil. Tissue Eng. Res.* **13** (2009) 9109.

[7] E. Klimiec, W. Zaraska, K. Zaraska, K.P. Gąsiorski, T. Sadowski, M. Pajda // *Microelectron. Reliab*. **48** (2008) 897.

[8] M. Pozzi, M. Zhu // *Smart Mater. Struct.* **21** (2012) 055004.

[9] G. Zhu, P. Bai, J. Chen, W.Z. Lin // *Nano Energy* **2** (2013) 688.

[10] J. Xie, C. Lee, H. Feng // *J. Micro Electro Mechancal. Syst.* **19** (2010) 317.

[11] K. Ishida, T.C. Huang, K. Honda, Y. Shinozuka, H. Fuketa, T. Yokota, T. Sakurai // *IEEE J. Solid State Circuits* **48** (2013) 255.

[12] J. Zhao, Z. You // *Sci. World J.* **2014** (2014) 893496.

[13] J. Zhao, Z. You // *Sensors* **14(7)** (2014) 12497.

[14] S. Niu, X. Wang, F. Yi, Y.S. Zhou, Z.L. Wang // *Nature Communications* **6** (2015) 8975.

[15] W. Jung, M. Lee, S. Baek, S. Yoon // *Nano Ene*rgy **22** (2016) 514.

[16] D. Nikolov, E. Manolov, D. Pissoort // Electronics **11** (2012) 11,

[17] C. Capaday, R.B. Stein // *J. Physiol*. **392** (1987) 513.

[18] A Proto, M Penhaker, D Bibbo, D Vala, S Conforto, M Schmid // *Sensors* **16(4)** (2016) 524.

[19] Woo-Suk Jung, Min-Jae Lee, Min-Gyu Kang // *Nano Energy* **13** (2015) 174.

[20] Yingzhou Han, Yalu Cao, Jingjing Zhao, Yajiang Yin, Liangchen Ye, Xiaofeng Wang, Zheng You // *Sensors* **16(9)** (2016) 1502.

[21] K. Boby, P.K. Aleena, C.V. Anumol, J.A. Thomas, K.K. Nimisha // *IJEIT* **3(10)** (2014) 264.

[22] Anjana Jain, P. Siva Subba Rao, Jayanth Kumar // *ISSS National Conference on MEMS, Smart Materials, Structures and Systems September 06-07, 2013, Pune, India* (2013)

[23] W. Jung, M. Lee, M. Kang, H. Gyu // *Nano Energy* **13(3)** (2015) 174.

[24] F. Yi, X. Wang, S. Niu, S. Li, Y. Yin, K. Dai, G. Zhang, L. Lin, Z. Wen, H. Guo et al. // *Sci Adv*. **2(6)** (2016) e1501624.

Materials Physics and Mechanics 37 (2018) 168-175 Received: December 22, 2017

ANALYZING THE OUTPUT CHARACTERISTICS OF A DOUBLE-CONSOLE PEG BASED ON NUMERICAL SIMULATION

A.N. Soloviev[1,2,3], I.A. Parinov[1], A.V.Cherpakov[1,3]*, V.A. Chebanenko[1,2], E.V. Rozhkov[1]

[1]Southern Federal University, Rostov-on-Don, Russia

[2]Southern Scientific Center of RAS, Rostov-on-Don, Russia

[3]Don State Technical University, Rostov-on-Don, Russia

*e-mail: alex837@yandex.ru

Abstract. A finite-element simulation of a two-cantilever piezoelectric generator (PEG) is considered. The generator had a bimorph arrangement of piezoelements. Finite element modeling was performed in ANSYS software. The PEG considered is part of an energy generation system, designed to convert mechanical energy from the environment into an electrical energy, with subsequent accumulation. The results of the modal analysis of the first 10 modes of oscillations are present. Harmonic analysis is performed, when damping is taken into account. With the given scheme of electrical connection of PEG elements and various active loads, the results of the output voltage and power for the first four modes are obtained.
Keywords: double-cantilever piezoelectric generator (PEG); finite-element simulation; ANSYS; modal analysis; harmonic analysis; output characteristics.

1. Introduction

In recent years, research has been actively performed on the development of piezoelectric converters of mechanical energy into electrical energy. This type of transducers was called piezoelectric generators (PEGs). The basic information on PEGs, as well as the problems arising at the development stages of energy harvesting devices, were given in review papers [1 – 4], as well as in the fundamental monograph [5].

Depending on the field of application, PEGs of various types have been created, in which a direct piezoelectric effect is used when excitation in the sensitive element is mainly longitudinal (d_{33}) [6 – 9] or bending (d_{31}) [10 – 14] oscillations.

The problem of estimating the energy efficiency of a cantilever type PEG was previously considered in [3, 5, 11, 12, 14]. It has been shown that the output power of PEG depends not only on the electrical characteristics of the piezoceramic materials (PKMs) of PEG sensitive elements, but also on the measurement technique of their output characteristics as well as on the parameters of the electrical circuit [20].

One of the ways to increase the energy efficiency of PEG is to expand the bandwidth of operating frequencies. Usually, a Cantilever type PEG works only on the first mode of oscillation, because the output electrical characteristics of the subsequent modes are small and not of interest for energy harvesting. This, in turn, indicates a narrow band of operating frequencies of PEG cantilever type. In addition, in real working environments, there are often oscillations of arbitrary shape, which are the result of applying oscillations with different frequencies, rather than purely harmonic with one frequency, which are usually used in experiments. Nevertheless, attempts are made to expand the band of PGE operating frequencies of the cantilever type by modifying the classical design and introducing various

http://dx.doi.org/10.18720/MPM.3722018_9

engineering solutions into it. This, in turn, not only affects the operating frequencies, but also affects the output electrical characteristics of the generator.

In [15], the authors proposed a so-called embedded cantilever in order to widen the bandwidth of the cantilever type PEG with attached mass. This device had two degrees of freedom, as well as two operating modes of oscillations. The constructive solution consists in using a cantilever, which includes one main cantilever beam and an internal built-in cantilever beam, each of which has piezoelectric transducers. The power, received by the authors, was 1.5 mW for the main beam and 0.8 mW for the internal (enclosed) beam.

In [16], a PEG with multi-cantilever piezoceramic elements was developed, operating at low frequencies. The device consisted of six piezoelectric consoles of different lengths with different masses at their free ends. Researchers have shown experimentally that it can operate at several low resonance frequencies. The maximum power, obtained by this generator was 2.5 μW, and can be increased by increasing the number of consoles.

In [17], the researchers developed a cruciform piezoelectric generator and investigated its output characteristics. The generator consisted of a thin centrally symmetric cross-shaped elastic substrate and four rectangular piezoceramic elements that were attached to the upper surface of the four blades of the substrate. The exciting force from the oscillation source was applied to the center of the substrate. For the substrate, four types of materials were used: aluminum, copper, brass and stainless steel SUS304. Of all materials, PEG on a SUS304 steel substrate showed the highest values of output voltage (4.42 V) and current (7.83 μA).

There are several ways of modeling PEG: mathematical model with lumped parameters [8, 14], mathematical model with distributed parameters [7, 9, 14] and finite element model [6,10,18,19]. In this paper, the finite element method will be used, since it is the most convenient for modeling and analysis of structural solutions.

The above brief analysis of known works has shown that the problem of creating an energy efficient construction of cantilever PEG in a whole is not yet solved, although it is quite relevant.

2. Formulation of problem

We analyze the output characteristics of a two-cantilever piezoelectric energy generator having a bimorph structure symmetrically, arranged with respect to the y-axis, to perform a modal and harmonic analysis.

3. Finite element modelling of PEG

Continuous models of composite elastic, electroelastic and electroacoustic medium. Piezoelectric energy harvesting device is a composite elastic and electroelastic solid, which makes small relative oscillations in the moving coordinate system. Rectilinear vertical motion of the system is given by the law $y(t)$ or, in case of the external force excitation, by $F(t)$ or pressure $\sigma(t)$, according to which the device's base is moving. In these conditions, the initial boundary value problem of linear electrodynamics theory is quite adequate mathematical model, which describes the functioning of such device [21].

In the present paper, we use the linear theory of elasticity and electrodynamics, based on the dissipation of energy, which is realized in the ANSYS software [22], as well as the equations of motion of liquids and gases in the acoustic approximation [23].

For piezoelectric medium, we have:

$$\rho\ddot{u}_i + \alpha\rho\dot{u}_i - \sigma_{ij,j} = f_i;\ D_{i,i} = 0, \tag{1}$$

$$\sigma_{ij} = c_{ijkl}(\varepsilon_{kl} + \beta\dot{\varepsilon}_{kl}) - e_{ijk}E_k;\ D_i + \varsigma_d\dot{D}_i = e_{ikl}(\varepsilon_{kl} + \varsigma_d\dot{\varepsilon}_{kl}) + э_{ik}E_k, \tag{2}$$

$$\varepsilon_{kl} = (u_{k,l} + u_{l,k})/2;\ E_k = -\varphi_{,k}, \tag{3}$$

where ρ is the density of the material; u_i are the components of the vector-function of displacement; σ_{ij} are the components of the stress tensor; f_i are the components of the vector of the density of mass forces; D_i are the components of the electric induction; c_{ijkl} are the components of the fourth rank tensor of the elastic moduli; e_{ijkl} are the components of the third rank tensor of piezoelectric coefficients; ε_{ij} are the components of strain tensor; E_i are the components of the electric field; φ is the electric potential; $э_{ij}$ are the components of the second rank tensor of the dielectric constants; $\alpha, \beta, \varsigma_d$ are non-negative damping coefficients (in ANSYS $\varsigma_d = 0$).

Modeling. The full-scale finite-element PEG model has a two-cantilever structure in the form of a bimorph, symmetrically arranged with respect to the *y*-axis (Fig. 1a). Thin symmetrical piezoelements are polarized in thickness. The gluing of piezoelements to the substrate is not taken into account. The geometric dimensions of the PEG are shown in Fig. 1a: the substrate has dimensions $l \times b \times h$ = 120 × 9.8 × 1 mm^3, the piezoelectric elements consist of two identical piezoelectric plates, polarized in thickness with dimensions $l_p \times b_p \times h_p$ = 54 × 6 × 0.5 mm^3. The center of the attached mass is fixed at a distance l_m from the clamp of the cantilever. The range of sizes l_m can vary from 65 to 110 mm. In the calculation it was assumed l_m = 65 mm. The electrical circuit of the PEG connection with the active load is shown in Fig. 1b. The value of the attached mass can vary from 3 to 25 grams. In the calculation, M = 3 g was adopted. The material of piezoceramic elements is PCR-7M. The main properties of the PEG structure are also given in Tables 1 – 3 [11]. The generator base was $l_x \times h_z \times b_y$ = 10 × 20 × 20 mm^3.

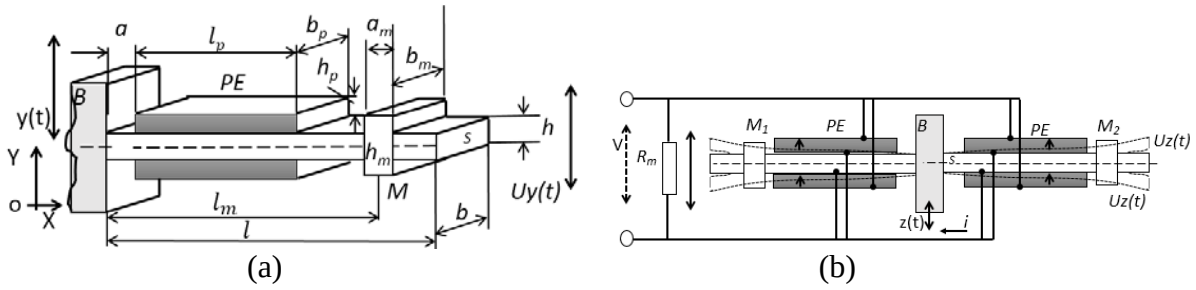

(a) (b)

Fig. 1. Electric scheme of compound PEG under active load.

Table 1. Characteristics of the dimensions of PEG elements.

Element	Parameter				
Piezoelement	l_p, mm	b_p, mm	h_p, mm		
	54	6	0.5		
Substrate	l, mm	b, mm	h, mm	a, mm	
	120	9.8	1	2	
Proof mass	M, gr	a_m, mm	h_m, mm	b_m, mm	l_m, mm
	3 – 25	7	6	29.8	65 – 110

Table 2. The elastic moduli C^E_{pq} (10^{10} Pa), piezoelectric coefficients e_{kl} (C/m^2) and relative permittivity $\varepsilon^{\xi}_{kk}/\varepsilon_0$ (at room temperature).

C^E_{11}	C^E_{12}	C^E_{13}	C^E_{33}	C^E_{44}	e_{31}	e_{33}	e_{15}	$\varepsilon^{\xi}_{11}/\varepsilon_0$	$\varepsilon^{\xi}_{33}/\varepsilon_0$
12.5	8.4	8.1	12.1	2.36	–9.0	28.3	17.9	1430	1350

Table 3. Mechanical properties of the structural materials.

No.	Element of PEG	Material	ρ, kg/m^3	E×10^{10} (Pa)	ν
1a, 1b	Substrate	fiberglass	1600	0.6	0.25
2a, 2b	Proof mass	plastic	2645	0.3	0.33
3a, 3b	Piezoelements	PCR-7M	7280	–	0.33
4	Base	steel	7700	21	0.33

The model scheme of the PEG structure is shown in Fig. 2a. Positions 1a, 1b show a substrate made of fiberglass; 2a, 2b are the attached masses; 3a, 3b is the piezoelectric element; 4 is the base of the generator.

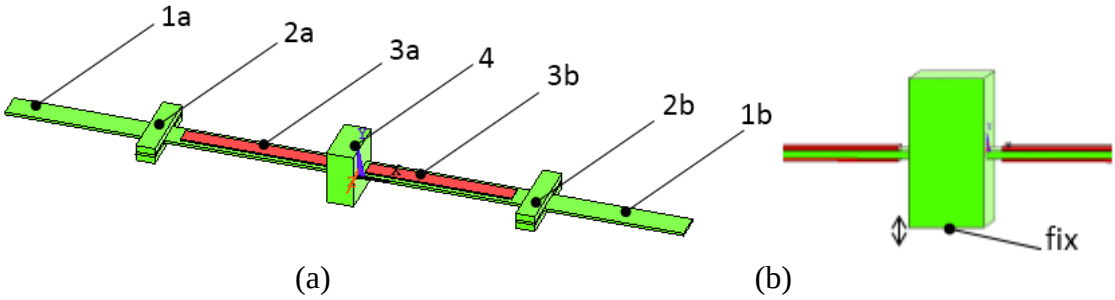

Fig 2. (a) Two-axis PEG model with the location of proof mass at l_m = 65 mm; (b) scheme of applying the load to the PEG base.

4. Results of calculations

With the help of the developed FE models in ANSYS software, based on the exact formulation of the problem (1) – (3), modal and harmonic analyses were performed.

Natural frequencies were calculated and their own forms of vibrations PEG. Fig. 3 shows their values and eigen forms of oscillations. The analysis of the first 10 vibration modes shows that 1 – 4, 9, 10 modes correspond to bending oscillations of the structure relative to the vertical *y*-axis (the vertical axis is shown in Fig. 3). For modes 1 and 2, it is shown that one of the plates is in the region making the maximum oscillation amplitudes, the second plate is in the conditional rest region. Mode 3 is antisymmetric with respect to the *y*-axis and mode 4 is axisymmetric about the *y*-axis. Modes 5 and 6 are modes of oscillations in the horizontal plane *Oxz* i.e. in the plane of the substrate and piezo plates of PEG. Mode 5 is axisymmetric, but mode 6 is an antisymmetric mode of oscillation. Modes 7 and 8 are the torsional modes of oscillations, respectively, of the left and right plates. All modes of oscillation are divided into pairs and each of them lies in the frequency range, which differ by no more than 0.5%.

Harmonic analysis of PEG oscillations with an active load for the first four modes of oscillations is performed. The damping coefficient was assumed equal to $\zeta = 0.031$ and was taken into account by the parameters MP, DMPR, for all 4 types of material properties in ANSYS. The active load was varied within $R = 5\times10^3 – 10^6$ Ω. The analysis of the results is shown in Tables 4 and 5. The dependences of the output voltage and output power of PEG on the value of the active load are shown in Figs. 4 and 5, respectively.

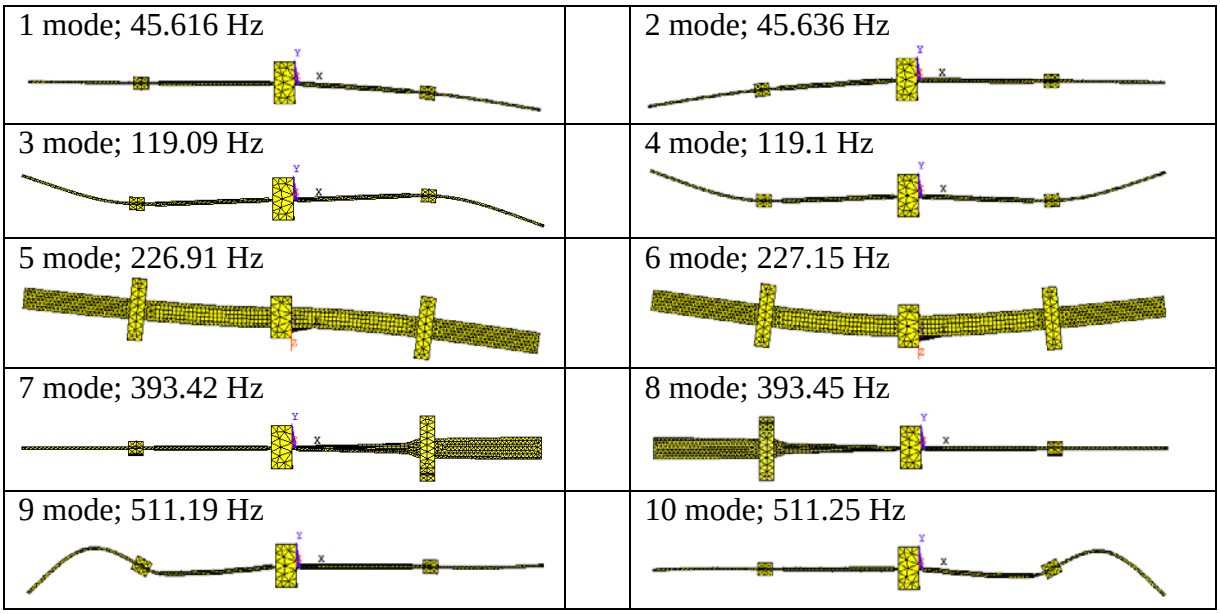

Fig 3. First ten modes of eigen forms of PEG with symmetric fixing of load oscillations.

Table 4. Output voltage of the PEG for location of proof mass lm = 65 mm; results are present for first four modes of oscillation.

Mode	Active load, R, 10^6 Ω						
	0.005	0.01	0.05	0.1	0.25	0.5	1
	Output voltage, U, V						
1	1.66	3.09	8.16	9.48	10.22	10.44	10.54
2	1.70	3.16	8.46	9.89	10.70	10.93	11.04
3	0.76	1.25	1.92	1.98	2.00	2.01	2.01
4	0.76	1.25	1.92	1.98	2.00	2.01	2.01

Table 5. Output power of the PEG when location of the attached mass was lm = 65 mm. The results are given for the first four modes of oscillation.

Mode	Active load, R, 10^6 Ω						
	0.005	0.01	0.05	0.1	0.25	0.5	1
	Output power, 10^{-6} W						
1	278.1	481.6	669.2	451.9	210.3	109.6	55.9
2	289.2	503.0	720.2	491.7	230.3	120.3	61.3
3	57.7	78.1	37.1	19.7	8.0	4.0	2.0
4	57.8	78.1	37.1	19.7	8.0	4.0	2.0

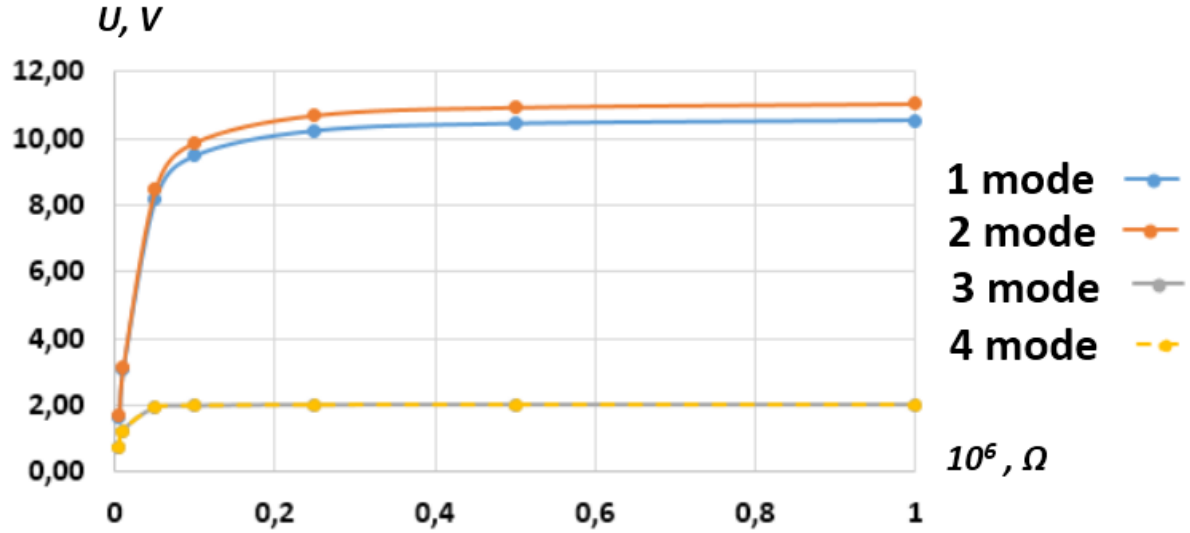

Fig 4. Dependence of output voltage on the load impedance for first four modes of oscillation.

5. Analysis of results

Analysis of the output voltage dependence on the value of active load shows that the voltage rises to a load value of 100 $k\Omega$. Its value for modes 1 and 2 is 9.48 V and 9.89 V, respectively, with R = 100 $k\Omega$. For 3 and 4 vibration modes, it is 1.98 V at R = 10 Ω. With a load of $R = 10^6$ Ω, the voltage for 1 – 4 modes is 10.54, 11.04, 2.01, and 2.01 V, respectively. Analysis of output power values, given in Table 5, shows that for this construction and fixation of PEG elements at location of proof mass l_m = 65 mm, the peak values of output power for 1st and 2nd modes of oscillation are achieved with an active load of R = 50 $k\Omega$ and are equal to 669 μW and 720 μW, respectively. For 3 and 4 modes, the peak value is attained at R = 10 $k\Omega$ and equal to approximately 78.1 μW.

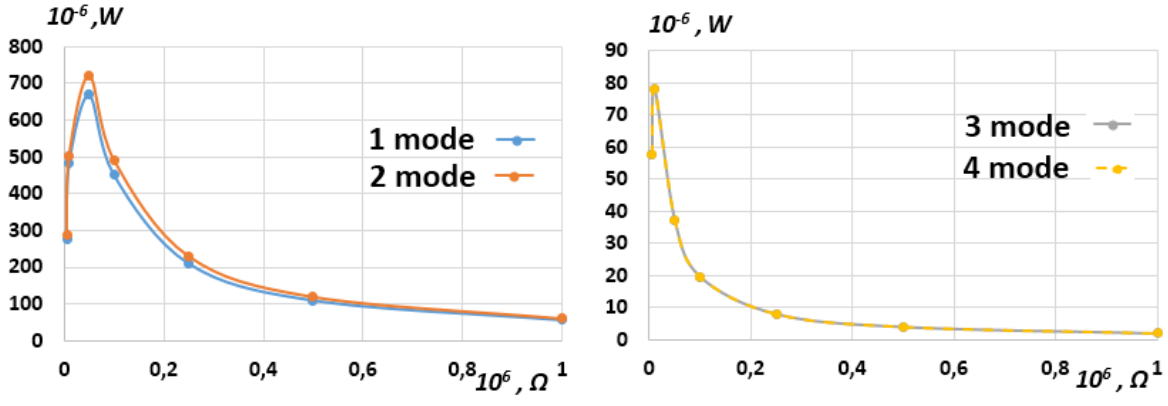

(a) (b)

Fig 5. Dependence of output power on load impedance for first four modes of oscillation.

6. Conclusions

By using FE analyses, we is simulated a double-cantilever PEG with proof masses having an axisymmetric execution structure. The proof mass was based in the region of the neighboring point of attachment of the piezoelement at l_m = 65 mm. A modal analysis of the natural oscillations of the PEG was also performed and showed need to use first four modes of oscillations. They have the bending character of the oscillations with respect to the vertical y-axis. For this oscillator model, the resonances were near the circular frequencies ω= 45.616 – 45.636 Hz for the 1st and 2nd modes of oscillations and ω = 119.09 – 119.1 Hz for the 3rd and 4th modes of oscillations. Taking into account these parameters, a harmonic

analysis of PEG oscillations with an active load and taking into account damping for the first 4 vibration modes is performed. The analysis shows that for 1 and 2 vibration modes, the maximum output power is achieved with a load resistance R = 50 $k\Omega$ and is 669 μW and 720 μW.

A more detailed analysis of the output power of PEG requires calculation with various values of proof mass, taking into account other properties of the substrate material and the dimensions of the piezoelements.

Acknowlegments*. The work was carried out with the partial support of the Ministry of Education and Science of Russia (No. Bch0110-11/2017-20), and RFBR (Nos. 16-08-00740, 17-08-00621, 17-08-01373).*

References

[1] A. Erturk, D.J. Inman, *Piezoelectric Energy Harvesting* (John Wiley & Sons, 2011).
[2] S.R. Anton, *Multifunctional Piezoelectric Energy Harvesting Concepts* (PhD Thesis. Virginia Polytechnic Institute and State University. Blackburn, Virginia, USA, 2011).
[3] A. Badel, D. Guyomar, E. Lefeuvre, C. Richard // *Journal of Intelligent Material Systems and Structures* **16(10)** (2005) 889.
[4] V.A. Chebanenko, V.A. Akopyan, I.A. Parinov, In: *Piezoelectrics and Nanomaterials: Fundamentals, Developments and Applications*, ed. by I.A. Parinov (Nova Science Publishers, New York, 2015) 243.
[5] D. Guyomar, M. Lallart // *Micromachines* **2(2)** (2011) 274.
[6] S. Shevtsov, V. Akopyan, E. Rozhkov, V. Chebanenko, C.-C. Yang, C.-Y. Jenny Lee, C.-X. Kuo, In: *Advanced Materials – Manufacturing, Physics, Mechanics and Applications*, ed. by Ivan A. Parinov, Shun-Hsyung Chang, Vitaly Yu. Topolov (Springer, Heidelberg, New York, Dordrecht, London, 2016), p. 534.
[7] A.N. Soloviev, V.A. Chebanenko, I.A. Parinov, In: *Analysis and Modelling of Advanced Structures and Smart Systems*, ed. by Holm Altenbach, Erasmo Carrera, Gennady Kulikov (Springer, Heidelberg, New York, Dordrecht, London, 2018). (In press).
[8] S. Zhao, A. Erturk // *Sensors and Actuators A: Physical* **214** (2014) 58.
[9] J. Wang, Z. Shi, Z. Han // *Journal of Intelligent Material Systems and Structures* **24(13)** (2013) 1626.
[10] A.N. Soloviev, I.A. Parinov, A.V. Cherpakov, V.A. Chebanenko, E.V. Rozhkov, L.V. Duong, In: *Proceedings of the First Structural Integrity Conference and Exhibition (SICE-2016)*, ed. by R.V Prakash, V. Jayaram, A. Saxena (Springer, Heidelberg, New York, Dordrecht, London, 2017).
[11] V.A. Akopyan, Yu.N. Zakharov, I.A. Parinov, E.V. Rozhkov, S.N. Shevtsov, V.A. Chebanenko, In: *Nano- and Piezoelectric Technologies, Materials and Devices*, ed. by Ivan A. Parinov (Nova Science Publishers, New York, 2013), p. 111.
[12] V.A. Akopyan, I.A. Parinov, Yu.N. Zakharov, V.A. Chebanenko, E.V. Rozhkov, In: *Advanced Materials – Studies and Applications*, ed. by Ivan A. Parinov, Shun-Hsyung Chang, Somnuk Theerakulpisut (Nova Science Publishers, New York, 2015), p. 417
[13] A. Erturk, D.J. Inman // *Smart Materials and Structures* **18(2)** (2009) 025009.
[14] N.E. Dutoit, B.L. Wardle, S.G. Kim // *Integrated Ferroelectrics* **71(1)** (2005) 121.
[15] Hao Wu, Lihua Tang, Yaowen Yang, Chee Kiong Soh // *Journal of Intelligent Material Systems and Structures* **24(3)** (2013) 357.
[16] M. Rguiti, A. Hajjaji, S. D'Astorg et al. // *Optical Materials* **36(1)** (2013) 8.
[17] Jung-Hoon Lim, Choong-Hyo Park, Jong-Wook Kim et al. // *Journal of Electroceramics* **39(1-2)** (2013) 108.

[18] L.V. Duong, M.T. Pham, V.A. Chebanenko, A.N. Solovyev, Chuong V. Nguye // *International Journal of Applied Mechanics* **9(6)** (2017) 16.

[19] A.V. Cherpakov, V.A. Chebanenko, I.A. Parinov, S.-H. Chang, M.A. Jani, In: *Proceedings of the International symposium "Physics of lead-free piezoactive and relative materials (Analysis of current state and prospects of development), LFPM-2016", 12-15 September, 2016, Tuapse, Russia* **2** (2016) 265.

[20] A.A. Gusev, E.G. Avvakumov, V.P. Isupov, L.A. Reznichenko, I.A. Verbenko, A.I. Miller, A.V. Cherpakov, In: *Piezoelectric Materials and Devices,* ed. by Ivan A. Parinov (Nova Science Publishers, New York, 2011), p. 189.

[21] A.V. Belokon, A.V. Nasedkin, A.N. Soloviev // *Applied Mathematics and Mechanics*. **66(3)** (2002) 491 (In Russian)

[22] A.V. Nasedkin, *The wave field in anisotropic elastic media with complicated properties and methods of finite element dynamic analysis* (DrSc Thesis, RSU, Rostov-on-Don, 2001), p. 271 (In Russian).

[23] V.A. Krasilnikov, V.V. Krylov, *Introduction to Physical Acoustics* (Nauka, Moscow, 1984) (In Russian).

Materials Physics and Mechanics 37 (2018) 176-183 Received: December 22, 2017

PLASTIC FORMING MODEL FOR AXISYMMETRIC SHELLS

A.S. Yudin

I.I. Vorovich Institute of Mathematics, Mechanics and Computer Sciences,

Southern Federal University, Milchakov Str., 8-A, Rostov-on-Don, 344090, Russia

e-mail: yudin@math.sfedu.ru

Abstract. The mathematical model of plastic forming dome-like shells is present. The forming is performed by pressure from a flat circular plate, clamped along the contour. Point force can be applied in the center. The semi-inverse method is used to resolve this physical and geometrical nonlinear problem.

Keywords: large deformations; nonlinear mathematical model; semi-inverse method; forming of dome-type shells.

1. Introduction

Mathematical modeling of plastic changes in the shape of shells of rotation is actual for improving the technologies of plastic forming dome-like shells having a predetermined critical load of buckling under the action of uniformly distributed load from the bulge. The manufacturing of such shells is performed by free stretching by the pressure of the flat round plates, rigidly clamped on a circular contour.

2. Equations

The model is based on the equations that allow large displacements and angles of rotation, changing of the middle surface metric and compression of the material normal. Power approximation of the diagrams of hardening material and physical deformation ratio with a logarithmic relative elongation are used [1].

It is proposed that relative elongations e_k, $\varepsilon_k=e_{k|}|_{\zeta=0}$, $k=1, 2, 3$, is comparable to one; the compression of the material normal $e_3=\varepsilon_3$ is constant in thickness. Kinematic relations are of the form [1]:

$e_1=(\varepsilon_1+\zeta\kappa_1)$, $\kappa_1=\Phi_o'/\alpha_o-\delta_3K_1$, $\varepsilon_1=(w'\sin\Phi+u'\cos\Phi)/\alpha_o+\cos(\Phi-\Phi_o)-1$;

$e_2=(\varepsilon_2+\zeta\kappa_2)$, $\varepsilon_2=u/r_o$, $\kappa_2=(\sin\Phi_o)/r_o-\delta_3K_2$; $K_1=\Phi'/\alpha_o$, $K_2=(\sin\Phi)/r_o$.

$\gamma=\gamma_o/\delta_1$, $\gamma_o=(w'\cos\Phi-u'\sin\Phi)/\alpha_o-\sin(\Phi-\Phi_o)$.

Here Φ_o and Φ are the angles of the incline of material normal to the rotation axis before and after deformation; κ_1 and κ_2 are the characteristics of change of the main curvatures; $\delta_k=1+\varepsilon_k$, $k=1, 2, 3$. For the plate in the initial state, the incline angle of the axis of symmetry $\Phi_o=0$. The angle of the transverse shear γ is supposed small, and below is considered to be zero.

The differential system of equations for a plate, loaded with uniform pressure, has the dimensionless form:

$$d\overline{T}^o/d\xi=\alpha_o\xi\delta_1\delta_2 p\cos\Phi,\quad d\overline{\Psi}^o/d\xi=\alpha_o\overline{N}_2^o-\alpha_o r_o\delta_1\delta_2 p\sin\Phi,$$

$$dM^o/d\xi=\alpha_o M_2^o\cos\Phi+\alpha_o r_o\delta_1\overline{Q}^o/\varepsilon_*,$$

http://dx.doi.org/10.18720/MPM.3722018_10

$dw/d\xi = \alpha_o \delta_1 \sin\Phi$, $du/d\xi = \alpha_o(\delta_1 \cos\Phi - 1)$, $d\Phi/d\xi = \alpha_o K_1$, (1)

where

$\overline{T}^o = r_o \overline{V}^o$, $\overline{\Psi}^o = r_o \overline{H}^o$, $M^o = r_o M_1^o$;

$\overline{V}^o = \overline{N}_1^o \sin\Phi + Q^o \cos\Phi$, $\overline{H}^o = \overline{N}_1^o \cos\Phi - Q^o \sin\Phi$,

$\overline{N}_1^o = \overline{V}^o \sin\Phi + \overline{H}^o \cos\Phi$, $\overline{Q}^o = \overline{V}^o \cos\Phi - \overline{H}^o \sin\Phi$; (2)

$\overline{N}_j^o = N_j^o + \varepsilon_*(K_1 M_1^o + K_2 M_2^o)/\delta_j$, $j = 1, 2.$ (3)

Here $\xi \in [0, 1]$ is the independent radial Lagrangian coordinate; p is the intensity of hydrostatic pressure; $\varepsilon_* = h_*/R_*$ is the thin-wall parameter; $\overline{V}^o$ and $\overline{H}^o$ are the internal efforts in the direction of the axis of symmetry and radius of the cylindrical coordinate system; M_1^o is the bending moment. The coefficient of Lame α_o is supposed equal to one.

Many metals and alloys at large plastic deformation behave as almost incompressible. Therefore, the condition $\delta_1\delta_2\delta_3 = 1$ is assumed to be satisfied.

The material properties are characterized by the diagram of loading, which is approximated by a power function in the area of hardening:

$\sigma = E\bar{e}$, $\bar{e} \le \bar{\varepsilon}_{0.2}$, $\sigma = C\bar{e}^{\,\eta} = E_s\bar{e}$, $\bar{e} \ge \bar{e}_{0.2}$, $\bar{e} = (2/\sqrt{3})\sqrt{\bar{e}_1^2 + \bar{e}_1\bar{e}_2 + \bar{e}_2^2}$,

where $\bar{e}$ is the logarithmic deformation intensity of an incompressible material; $\bar{e}_j = \ln(1 + e_j)$; C, η are material constants; $\sigma_{0.2}$, $\bar{\varepsilon}_{0.2}$ are the stress and strain of the conditional yield strength, E is the Young's modulus, $E_s = C\bar{e}^{\,\eta-1}$ is the secant modulus.

We use the physical ratio of the Davis – Nadai for an incompressible material, coupling stress and the logarithmic strain in the principle axes:

$\sigma_1 = (4/3)\Lambda(\bar{e}_1 + 0.5\bar{e}_2)$, $\sigma_2 = (4/3)\Lambda(\bar{e}_1 + 0.5\bar{e}_2)$.

Here $\Lambda = E$ in the areas of elasticity $\bar{e} \le \bar{e}_{0.2}$ and $\Lambda(\bar{e}) = E_c(\bar{e})$ in the plastic zones $\bar{e}_{0.2} < \bar{e} < \bar{e}_l$; $\tilde{\bar{e}} = \bar{e}/\bar{e}_l$, where, σ_l, $\bar{e}_l$ are the elastic limit stresses and strains.

Diagram of material properties is transferred to a single plane in the coordinates of the dimensionless stress $\tilde{\sigma} = \sigma/\sigma_l$ and the relative actual strains. These relations in dimensionless form take the view:

$\tilde{\sigma} = \sigma/\sigma_l$, $\bar{e} = \bar{e}_l\tilde{\bar{e}}$, $\tilde{\sigma}(\tilde{\bar{e}}) = \tilde{C}\bar{e}_l^{\eta}\tilde{\bar{e}}^{\eta} = \tilde{C}_l\tilde{\bar{e}}^{\eta}$, $\tilde{C} = \tilde{C}/\sigma_l$, $\tilde{C}_l = \tilde{C}\bar{e}_l^{\eta} = 1$,

$\tilde{E}_s(\tilde{\bar{e}}) = \tilde{C}\bar{e}_l^{(\eta-1)}\tilde{\bar{e}}^{(\eta-1)} = \tilde{C}_E\tilde{\bar{e}}^{(\eta-1)}$, $\tilde{C}_E = \tilde{C}\bar{e}_l^{(\eta-1)} = 1/\bar{e}_l$.

Further, to simplify the notation a tilde (~) is deleted. When constructing two-dimensional equations, $\Lambda(\bar{e}) \approx \Lambda(\bar{\varepsilon})$ can be put. This is justified in the considered task of strong drawing. Then the formulae of the dependences of forces and moments on strain components in dimensionless form has the simpler form:

$N_1^o = (k_\sigma/\varepsilon_*)B_1(\bar{\varepsilon}_1 + 0.5\bar{\varepsilon}_2)$, $N_2^o = (k_\sigma/\varepsilon_*)B_2(\bar{\varepsilon}_2 + 0.5\bar{\varepsilon}_1)$, (4)

$M_1^o = -k_\sigma D_1(\overline{K}_1 + 0.5\overline{K}_2)$, $M_2^o = -k_\sigma D_2(\overline{K}_2 + 0.5\overline{K}_1)$, (5)

where

$\bar{\varepsilon}_j = \ln(1 + \varepsilon_j) = \ln\delta_j$, $\overline{K}_j = K_j/\delta_j$, $j = 1, 2$; $k_\sigma = \sigma_l/E_*$;

$\overline{B}_1 = \overline{B}/\delta_1$, $\overline{B}_2 = \overline{B}/\delta_2$, $\overline{D}_1 = \delta_3^3\delta_2\overline{D}$, $\overline{D}_2 = \delta_3^3\delta_1\overline{D}$,

$\overline{B} = (4/3)\Lambda(\bar{\varepsilon})h_o$, $\overline{D} = (1/9)\Lambda(\bar{\varepsilon})h_o^3$.

3. Method

Let us consider the stretching by the pressure of a flat circular plate of thickness h_p, clamped along the contour of radius r_p, with ellipsoidal dome (segment) of a given height w_a. The meridian segment corresponds to an arc of an ellipse with semi-axes a_e and b_e, the relationship $k_e = b_e/a_e$, and square of eccentricity $e_x^2=1-(k_e)^2$. This is true if $a_e > b_e$ (oblate ellipsoid). In the case of $a_e < b_e$ (elongated ellipsoid), $k_e = a_e/b_e$.

Under free stretching of the plate by hydrostatic pressure resulting dome passes through the stages of both a flattened and elongated ellipsoids of rotation. Previously, we have constructed a solution for only slightly flattened spheroids with the use of the smallness of the eccentricity, which was provided by additional force at the pole. It is necessary to develop the method for the purposes of the extension of control over the form, identification materials and evaluation of limit states.

Let the ellipsoid be formed by rotating the ellipse around *z*-axis. Consider two forms of the ellipse equation (the axial section of the ellipsoid). One of them is parametric:

$$r_1 = \varphi(\tau) = a_e \sin\tau,\ \ z = \psi(\tau) = z_e - b_e \cos\tau, \tag{6}$$

where z_e is the coordinate of the ellipse centre. In this case, polar coordinate r_1 is connected with the Lagrangian r, counted on the plate, through the radial component of displacement u: $r_1 = r + u$. Since the considered ellipsoids are closed at the top, then $\tau_0 = 0$. We denote the values of the parameter τ on the segment contour by τ_c. In the transition to dimensionless values, we propose: $h_*=h_p$, $R_*=r_p$, $E_*=\sigma_l$.

We define τ_c through the parameters of the ellipse and the plate. We have on the contour of the elliptical segment $r_1 = r_p,\ z = 0$. Then from (6) it follows:

$$\frac{r_p}{-z_e} = -\frac{a_e}{b_e}\tan\tau_c = -\frac{1}{k_e}\tan\tau_c,\ \ \tau_c = \arctan\left(\frac{k_e r_p}{z_e}\right).$$

The second form is the classical geometry in the axes r_1 and z of cylindrical coordinate system:

$$(r_1/a_e)^2 + (z+z_c)^2/b_e^2 = 1. \tag{7}$$

Here the radial coordinate r and r_1 change from *0* to r_p and dimensionless value $r_p=1$. Solving (7) with respect to z, we have:

$$z = f(r_1) = z_c - k_e\sqrt{a_e^2 - r_1^2},\ \ k_e = b_e/a_e \tag{8}$$

Under a parametric specification of the surface in the form of (6), its square is calculated by the integral:

$$S = 2\pi\int_{\tau_0}^{\tau_c}\varphi(\tau)\sqrt{(\varphi,_\tau)^2 + (\psi,_\tau)^2}\,d\tau. \tag{9}$$

In the case of form (6) after substituting expressions for derivatives of functions $\varphi,_\tau = a_e\cos\tau,\ \psi,_\tau = b_e\sin\tau$, integral (9) hass the form:

$$S = 2\pi a_e\int_0^{\tau_c} F(\tau)d\tau, \tag{10}$$

where

$$F(\tau) = (\sin\tau)\sqrt{(a_e\cos\tau)^2 + (b_e\sin\tau)^2}.$$

To define the surface in the form (8), the square is given by the integral:

$$S = 2\pi\int_0^{r_p} r_1\sqrt{1+(f(r_1),_{r_1})^2}\,dr_1. \tag{11}$$

Here, $f(r_1),_{r_1}$ is the derivative of the function. Explicitly

$$f(r_1),_{r_1} = k_e r_1 / \sqrt{(a_e^2 - r_1^2)} . \quad (12)$$

Let us denote:

$$\Pi(r_1) = r_1 \sqrt{1 + (f(r_1)_{r_1})^2} .$$

The volume of the shell with variable thickness $h(r_1)$, having a rotational ellipsoid as the middle surface, can be obtained, if the thickness is substituted in the integrals (10), (11):

$$V_o = 2\pi a_e \int_0^{\tau_c} h(\tau) F(\tau) d\tau , \quad V_o = 2\pi \int_0^{r_p} h(r_1) \Pi(r_1) dr_1 . \quad (13)$$

The assumption about the form of the distribution function of the thickness is important. The analysis of experimental data and the performed measurements has shown that for shells with small eccentricity, the thickness can be approximated by a quadratic dependence:

$$h(x) = h_p \{1 - \delta[1 - (x/x_c)^2]\} . \quad (14)$$

However, when choosing an independent argument, different variants are possible here. The independent variables are the radii r and r_1, the parameter τ, the angle of inclination of the normal Φ, the arc length of the curve l. For shells with a small e_x the best results are given by the dependence on Φ:

$$h(\Phi) = h_p \{1 - \delta[1 - (\Phi/\Phi_c)^2]\} . \quad (15)$$

The listed parameters are related one of others. From (6) it follows: $\tau = \arcsin(r_1 / a_e)$. It can be shown that τ and Φ are not identical and are related by the formulae:

$$\tau = \arctan\left(\frac{a_e}{b_e} \tan\Phi\right), \quad \Phi = \arctan\left(\frac{b_e}{a_e} \tan\tau\right). \quad (16)$$

These values can be identified only if $k_e = b_e/a_e$ is close to one.

Along with the angle of inclination of the normal Φ, it is also logical to use the arc length of the meridian as an independent coordinate. For lengths of arcs of the curve, we have the formula:

$$L(\tau) = \int_0^{\tau} F_1(\tau) d\tau, \quad L(r_1) = \int_0^{r_1} \Pi_1(r_1) d\tau , \quad (17)$$

where $F(\tau) = \sqrt{(a_e \cos\tau)^2 + (b_e \sin\tau)^2}$, $\Pi(r_1) = \sqrt{1 + (f(r_1)_{r_1})^2}$.

The full length of the meridian arc is $L_c = L(\tau_c) = L(r_p)$. Then, instead of formula (14), we can take the following:

$$h(r_1) = h_p \{1 - \delta[1 - (L(r_1)/L_c)^2]\} . \quad (18)$$

Variant (18) is more convenient for measurements in physical experiments.

For one-parameter approximation of the type (15), (18) coefficient δ can be determined directly, based on the condition of incompressibility. The volume of the original plate with radius r_p and thickness h_p will be $V_p = \pi r_p^2 h_p$. Since this is an incompressible material, so $V_o = V_p$. Applying the second of formulae (13), we get:

$$2\pi h_p \int_0^{r_p} \{1 - \delta[1 - (\Phi(r_1)/\Phi_c)^2]\} \Pi(r_1) dr_1 = \pi r_p^2 h_p . \quad (19)$$

The angle of inclination of the normal Φ is defined here as a function from r_1 using the formula $\tau = \arcsin(r_1 / a_e)$ and (16).

We consider (19) as an equation for determining the ratio δ. It follows from:

$$\delta = [\int_0^{r_p} \Pi(r_1)dr_1 - r_p^2/2] \Big/ \int_0^{r_1} [1-(\Phi(r_1)/\Phi_c)^2]\Pi(r_1)dr_1 . \quad (20)$$

If the number of coefficients in the formula for the thickness is more than one ($n_h > 1$), then the condition of incompressibility will give the equation of connection between them. Then n_h–1 coefficients of these coefficients will be independent control parameters for the functional constructed below.

Further, we can construct a functional equation, from which with the help of the iterative process, the radial component of displacement is determined. With this aim, the condition of incompressibility is applicable to sites of the dome and plate, determined by the total Lagrangian coordinate *r*. We have the equation:

$$\int_0^{r_1(r)} [h(r_1)\Pi(r_1)]dr_1 = r^2/2, \quad (21)$$

where a variable upper limit $r_1(r) = r + u(r)$, and r_1 under the integral is the variable of integration. The independent variable in equation (18) is the Lagrangian coordinate *r*. Here, we will not specify the form of the thickness function.

In the integral (18), we select the term that can be easily integrated in an explicit form. For this, we will add and subtract 1:

$$\int_0^{r_1(r)} [1-1+h(r_1)\Pi(r_1)]dr_1 - r^2/2 = r + u(r) - \int_0^{r_1(r)} [1-h(r_1)\Pi(r_1)]dr_1 - r^2/2 . \quad (22)$$

From here

$$u(r) = \int_0^{r_1(r)} [1-h(r_1)\Pi(r_1)]dr_1 + r^2/2 - r . \quad (23)$$

For Equation (23) a simple iterative process can be organized on the base of the principle of contracting maps known in functional analysis [2]. By giving a certain initial approximation $u_0(r)$ and calculating the right-hand side in (20), using it, we obtain the first approximation $u_1(r)$. Further, the process is repeated and for (k+1)-th step we have:

$$u_{k+1}(r) = \int_0^{r_{1k}(r)} [1-h(r_1)\Pi(r_1)]dr_1 + r^2/2 - r , \quad (24)$$

where $r_{1k}(r) = r + u_k(r)$. As initial approximation, we can take the function:

$$u_0(r) = k_u r(1-r) . \quad (25)$$

The coefficient k_u is determined by the application at the top of the dome of the incompressibility condition and proximity to the homogeneous strain state of the middle surface: $\varepsilon_1(0) \approx \varepsilon_2(0)$. It gives:

$$k_u = \frac{1}{\sqrt{1-\delta}} - 1 . \quad (26)$$

The process (24) converges quickly. For accuracy of few tenths of percent, less than five iterations are enough. After finishing the calculation process, the components of the deformation $\varepsilon_2(\tau)=u(\tau)/\xi$, $\delta_2(\tau)=1+\varepsilon_2(\tau)$, $\delta_1(\tau)=[\delta_2(\tau)\delta_3(\tau)]^{-1}$, $\varepsilon_1(\tau)=\delta_1(\tau)-1$, as well as internal forces and moments (2), (3) are determined.

Then the system (1) is integrated. From the first, second, fourth and fifth equations, the relations are defined as

$$\overline{T}^o(\tau) = pJ_{11}(\tau) + P_0/(2\pi), \quad \overline{\Psi}^o(\tau) = J_{21}(\tau) - pJ_{22}(\tau) + r_p H_c ; \quad (27)$$

$w(\xi)= -w_o+J_{41}(\xi),\ u(\xi)= J_{51}(\xi),$ (28)

where

$$J_{11}(\tau)=\int_0^{\tau}[\xi/\delta_3(\xi)]\cos\Phi(\xi)d\xi;\quad J_{22}(\tau)=\int_0^{\tau}[\xi/\delta_3(\xi)]\sin\Phi(\xi)d\xi,$$

$$J_{41}(\tau)=\int_0^{\tau}\delta_1(\xi)\sin\Phi(\xi)d\xi,\quad J_{51}(\tau)=\int_0^{\tau}\delta_1(\xi)\cos\Phi(\xi)d\xi,\quad J_{21}(\tau)=\int_0^{\tau}\overline{N}_2^o(\xi)d\xi. \tag{29}$$

Displacements (25) vanish on the boundary contour. Values P_0 and H_c are constants of integration. Thus P_0 has the meaning concentrated in the top of the force affecting the shape of the shell, H_c is the radial force, distributed along the contour.

From the third equation of the system (1), it is possible to determine the forming pressure dome of a given height w_o. This can be performed in two ways: differential and integral. Since the geometry of the resulting shell is parametrically known, it is possible to determine the moments and their derivatives through the shell curvatures and the obtained expressions for the relative elongations. This is the first approach, which gives the formula for the pressure p :

$$p=\frac{[J_{21}(\tau)+r_pH_c]\sin\Phi(\tau)-[P_0/(2\pi)]\cos\Phi(\tau)+\varepsilon_*J(\tau)/\delta_1(\tau)}{J_{11}(\tau)\cos\Phi(\tau)+J_{22}(\tau)\sin\Phi(\tau)}\approx const, \tag{30}$$

where

$$J(\tau)=M_1^o(\tau)\{1-[\delta_1(\tau)/\delta_2(\tau)]\cos\Phi(\tau)\}+\tau dM_1^o(\tau)/d\tau.$$

If we integrate the third equation of the system, we get the formula:

$$p=\frac{\tau M_1^o(\tau)+r_pM_c-J_{31}(\tau)-J_{33}(\tau)+J_{34}(\tau)+J_{36}(\tau)}{J_{32}(\tau)+J_{35}(\tau)}\approx const, \tag{31}$$

where

$$J_{31}(\tau)=\int_0^{\tau}M_2^o\cos\Phi(\xi)d\xi;\quad J_{33}(\tau)=\frac{P_0}{2\pi\varepsilon_*}\int_0^{\tau}\delta_1(\xi)\cos\Phi(\xi)d\xi,$$

$$J_{34}(\tau)=\frac{1}{\varepsilon_*}\int_0^{\tau}\delta_1(\xi)J_{21}(\xi)\sin\Phi(\xi)d\xi,\quad J_{36}(\tau)=\frac{H_g}{\varepsilon_*}\int_0^{\tau}\delta_1(\xi)\sin\Phi(\xi)d\xi,$$

$$J_{32}(\tau)=\frac{1}{\varepsilon_*}\int_0^{\tau}\delta_1(\xi)J_{11}(\xi)\cos\Phi(\xi)d\tau,\quad J_{35}(\tau)=\frac{1}{\varepsilon_*}\int_0^{\tau}\delta_1(\xi)J_{22}(\xi)\sin\Phi(\xi)d\xi.$$

The output of the expression (30) by a constant is controlled by the parameters P_0, H_c, e_x.. In (31), these values are added to the constant M_c, which appears when integrating the third equation. A larger number of control parameters make it more advantageous to apply the formula (31), especially when forming high lift shells.

In constructing the solution for thickness, the formula (18) was mainly used. A generalized solution was tested by comparison with the more analytical version, built for a slightly flattened ellipsoid [1].

4. Numerical experiments

Along with the main formula of approximation of the thickness function (variant 1), we also considered other variants with additional terms to improve the accuracy of the output of the functional (31) to a stationary value. The variants 2 – 8 of the formulae for the thickness are present as

$$h_2(r_1) = h_0[1-\delta(1-F_{lc}(r_1)^2) - g_h e_x^2 (1-F_{lc}(r_1))^2];$$
$$h_4(r_1) = h_0[1-\delta(1-F_{lc}(r_1)^2) - g_k e_x^2 (1-F_{lc}(r_1))];$$
$$h_3(r_1) = h_0[1-\delta(1-F_{lc}(r_1)^2) - g_g e_x^2 (1-F_{lc}(r_1)^4)];$$
$$h_5(r_1) = h_0[1-\delta(1-F_{lc}(r_1)^2) - g_3 e_x^2 (1-F_{lc}(r_1)^3) - g_4 e_x^2 (1-F_{lc}(r_1)^4)];$$
$$h_6(r_1) = h_0[1-\delta(1-F_{lc}(r_1)^2) - g_1 e_x^2 (1-F_{lc}(r_1)) - g_3 e_x^2 (1-F_{lc}(r_1)^3) - g_4 e_x^2 (1-F_{lc}(r_1)^4)];$$
$$h_7(r_1) = h_0[1-\delta(1-F_{lc}(r_1)^2)(1-g_e e_x^2 F_{lc}(r_1))];$$
$$h_8(r_1) = h_0[1-\delta(1-F_{lc}(r_1)^2)(1-g_e e_x^2 F_{lc}(r_1)) - g_e e_x^2 (1-F_{lc}(r_1))^2].$$

These variants allow to improve the accuracy of the output functional on the stationary value from 1 – 1.5% to 0.25 – 0.5%. As shown by numerical experiments, the fifth variant is the most preferable.

Let us consider the stretching of a flat circular plate of thickness h_p, clamped along the contour of radius r_p, by an ellipsoidal dome (segment) of a given height, w_a. When stretching is near the pinch circuit, a sharp bend appears, in the area of which the flat, clamped part of the plate passes into the dome. As experiments show, this zone is very narrow (about 0.5 of the thickness of the plate). Therefore, its size can be neglected and it could be assumed for the dome the radius of the reference contour is equal to the radius of the original plate. This area is conventionally cut off, and its force influence is replaced by reactions, namely vertical and horizontal linear forces and moment. These quantities appear naturally in the integration of the equilibrium equations.

The equations of the model and the calculation process are fulfilled in dimensionless form. In particular, in the normalization of displacements and pressure, the following formulae are used:

$$\{u, w\}_n = \{u, w\}_d / R_*, \quad p_n = p_d/(E_*\varepsilon_*), \quad \varepsilon_* = h_*/R_*. \tag{32}$$

Here u, w are the horizontal and vertical movements; h_*, R_* are typical small and large sizes; ε_* is a thin-wall parameter; indices n and d point the dimensionless and dimensional quantities, respectively. As characteristic quantities, $h_* = h_p$, $R_* = r_p$, $E_* = E$ (Young's modulus) or σ_v (tensile strength) were taken. The calculation results can be found both in dimensionless and dimensional forms.

We represent some results of calculations in the dimensional form, for the return to which formulae (32) are used. Let us consider a plate with a thickness h_p = 0.38 mm and radius of the reference circuit r_p = 100 mm, Young's modulus E=0.21·10^6 MPa, yield strength σ_{02} = 360 MPa, tensile strength σ_v=720 MPa, ultimate strain intensity $\bar{\varepsilon}_v = 0.615$, yield strain $\varepsilon_{02}=\sigma_{02}/E$ = 0.001714, ε_* = 0.0038. The diagram of the plastic properties of the material corresponds to stainless steel 12X18H10T. Such plates are used for the manufacture of the destructible elements of the devices that protect technological equipment and tanks from destruction by excess pressure [3].

When the pressure is stretched freely with no force, applied at the apex, the shell passes through the stages of a segment of a slightly flattened ellipsoid, a spherical dome and an elongated ellipsoid.

The Table 1 shows the matching values of the height of the dome w_a, the forming pressure p_f and the eccentricity e_x of the ellipsoidal shell meridian. The nonlinear dependence of p_f – w_a is also represented in Fig. 1 having the form that is observed in physical experiments.

Table 1. Values of the height of the dome w_a, the forming pressure p_f and the eccentricity of the ellipsoids.

w_a (mm)	p_f (MPa)	e_x
0.10	67	0.015
0.15	106	0.007
0.20	144	0.00
0.25	181	0.16
0.30	212	0.20
0.35	240	0.21
0.40	259	0.22
0.45	270	0.23
0.50	277	0.25

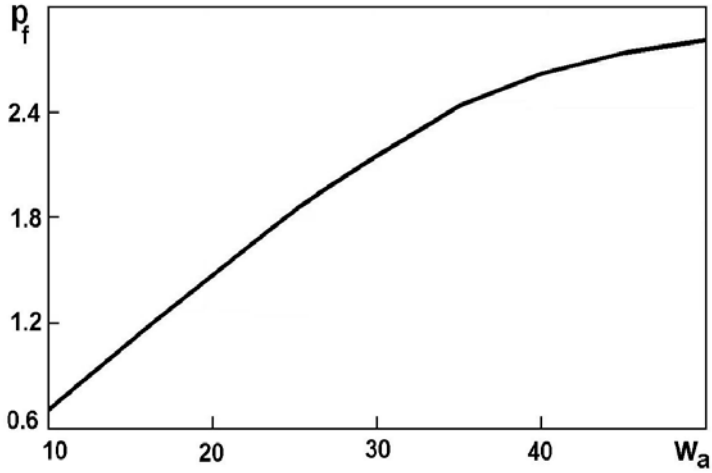

Fig. 1. Nonlinear dependence of pressure forming the dome height.

5. Conclusions

A more general form of the constructed algorithm makes it possible to consider variants for ellipsoids with fairly large eccentricities. The solution, where the power series expansion by eccentricity is used, follows from the generalized one as a special case. Although for more efficient calculations, this technique can be used for small eccentricities, a small amount of eccentricity is not assumed in the generalized approach presented here. This makes it possible to expand the possibilities of applying this semi-return method in the case of deformations of plastic materials close to the limiting ones.

Acknowledgement. *The work was carried out within the framework of the project of the basic part of state task of Russian Ministry of Education and Science No. BCh0110-11/2017-20.*

References

[1] A.S. Yudin, *Stability and Oscillations of Structurally Anisotropic and Artificial Shells* (Southern Federal University Press, Rostov-on-Don, 2011). (In Russian)
[2] L.P. Lebedev, I.I. Vorovich, *Functional Analysis in Mechanics* (Springer, NY, 2002).
[3] A.S. Yudin, N.V. Belikov, In: *Advanced Materials – Studies and Applications*, ed. by I.A. Parinov, S.H. Chang, S. Theerakulpisut (Nova Science Publishers, New York, 2015), p. 499.

Materials Physics and Mechanics 37 (2018) 184-191 Received: December 22, 2017

INVESTIGATION OF THE FEATURES OF STRESS-STRAIN STATE IN LAYERED CYLINDRICAL CONSTRUCTIONS, MANUFACTURED OF TRANSVERSE-ISOTROPIC MATERIALS, UNDER PULSE IMPACT

I.P. Miroshnichenko

Don State Technical University, Gagarin Square 1, Rostov-on-Don, 344000, Russian Federation

e-mail: ipmir@rambler.ru

Abstract. The paper is devoted to the numerical study and analysis of the characteristics of the stress-strain state in layered cylindrical constructions made of transversely isotropic materials under pulsed loading with a given spatial-temporal distribution.
Keywords: layered cylindrical structure; a pulsed impact; the stress-strain state.

1. Introduction

Currently, the widespread use of anisotropic composite materials in the force elements of the constructions of different goods increases the importance of the study of the features of their stress-strain state, caused by wave processes under local pulsed loading. These loads arises both as in exploring the constructions, as in diagnostics of their state by active acoustic methods of nondestructive testing.

The paper [1] presents detailed specific examples of the numerical investigation of the stress-strain state in layered cylindrical structures made of transversely isotropic materials, subjected to pulse loads arising due to the curvature of the construction surface and physical-mechanical characteristics of the materials of layers.

The aim of this work is the numerical study and analysis of the stress-strain state in layered cylindrical constructions made of transversely isotropic materials under pulsed loading with a given spatial-temporal distribution.

2. Statement of problem: initial data and relationships

Let us consider the problem of determining the stress-strain state in layered cylindrical construction, referred to a cylindrical coordinate system (see Fig. 1). Pressure pulses are applied to some *j*-th regions of outer ($r = r_N$) the surface of the construction. The internal surface ($r = r_0$) is free of stresses ("free boundary"), and the interfaces of the layers ($r = r_n;\ n = 1,2,..., N-1$) rigidly fastened to each other ("hard bonding").

The layers made of a transversely isotropic material, the axes of symmetry of these layers coincide with the *z*-axis, and the design is assumed to be sufficiently long that corresponds to the radiation conditions at the construction edges.

The fields of displacements and stresses in each layer of the considered construction are described by the equations of motion [2] and should satisfy the boundary conditions.

We obtain the solution of this problem, based on the generalized method of the scalarization of dynamic elastic fields in transversely isotropic media [3]. It allows one to

http://dx.doi.org/10.18720/MPM.3722018_11

describe the searched fields by using three potential functions φ, w, v, corresponding to quasi-longitudinal, quasi-transverse and transverse waves and being solutions of the Helmholtz equations.

To find the full distributions of displacements and stresses, it is used spectral method. The pulse load $p(\theta, z, t)$ is present by its spectral density, which in the case of independence of the spatial-temporal distribution of the impact on the *z*-coordinate (non-axisymmetric case) has the form:

$$P(\theta, \omega) = \int_{-\infty}^{\infty} p(\theta, t) e^{i\omega t} dt, \tag{1}$$

where ω is the circular frequency.

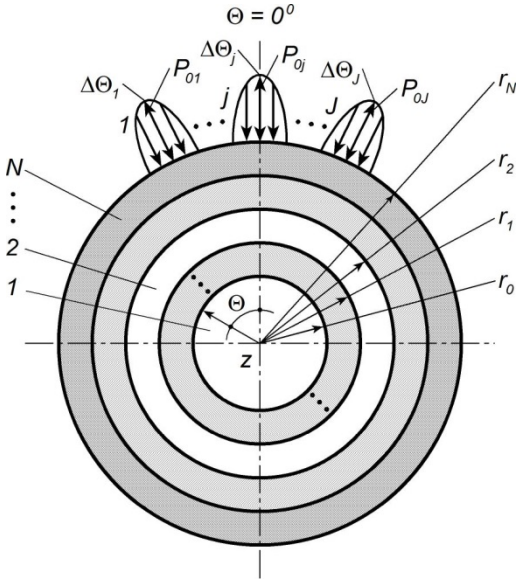

Fig. 1. Calculation scheme.

For example, under multipulse loading, if the distribution of each of the pressure pulses on coordinate θ has the semi-sine form, and the temporal dependence is given by the Gauss function, then the spectral density of this impact is defined as

$$P(\theta, \omega) = \sum_{j=1}^{J} \left[- p_{0j} \sqrt{\frac{\pi}{\beta_j}} e^{-\omega^2 / 4\beta_j} e^{i\omega t_j} \right] \left[a_{0j} + \sum_{m=1}^{M} a_{mj} \cos\left\{ m(\theta + \Delta\theta_j) \right\} \right], \tag{2}$$

where J is the number of pressure pulses; p_{0j}, τ_j, t_j are the amplitude, duration, and initial time of the action of the *j*-th pressure pulse, respectively;

$$\beta_j = \left(\frac{3.035}{\tau_j} \right)^2; \quad a_{oj} = \frac{\tau_{\theta j}}{\pi^2}; \quad a_{mj} = 2\pi\tau_{\theta j} [\sin(\pi x_{1j}) / \pi x_{1j} + \sin(\pi x_{2j}) / \pi x_{2j}];$$

$x_{1j} = \frac{m\tau_{\theta j}}{2\pi} - 0.5$; $x_{2j} = \frac{m\tau_{\theta j}}{2\pi} + 0.5$; $\tau_{\theta j}$ is the duration of the *j*-th pressure pulse in coordinate θ; $\Delta\theta_j$ is the position of the *j*-th pressure pulse relatively of $\theta = 0$.

In non-axisymmetric case, the expressions for the displacements and stresses, which presence in the boundary conditions due to the functions φ and v, have the forms:

$$U_r = \overset{(L)}{D}_1 \frac{\partial\varphi}{\partial r} + \frac{1}{r} \frac{\partial v}{\partial\theta};$$

$$U_\theta = \overset{(L)}{D}_1 \frac{\partial \varphi}{\partial \theta} - \frac{\partial \nu}{\partial r};$$

$$\sigma_{rr} = \overset{(L)}{d}_1 \varphi + \overset{(L)}{d}_4 \frac{\partial^2 \varphi}{\partial r^2} + (C_{11} - C_{12})\left(\frac{1}{r}\frac{\partial^2 \nu}{\partial r \partial \theta} - \frac{1}{r^2}\frac{\partial^2 \nu}{\partial \theta^2} \right);$$

$$\sigma_{r\theta} = \overset{(L)}{d}_4 \left(\frac{\partial \varphi}{\partial r \partial \theta} - \frac{1}{r^2}\frac{\partial \varphi}{\partial \theta} \right) + \frac{1}{2}(C_{11} - C_{12})\left(\frac{1}{r^2}\frac{\partial^2 \nu}{\partial \theta^2} + \frac{1}{r}\frac{\partial \nu}{\partial r} - \frac{\partial^2 \nu}{\partial r^2} \right), \tag{3}$$

where $\overset{(L)}{D}_1 = \dfrac{\overset{(L)}{g}{}^2 b_4}{b_3 - \overset{(L)}{g}{}^2 (1 - b_4)}$;

$b_3 = \omega^2 \rho / C_{11}$; $\quad b_4 = (C_{13} + C_{44}) / C_{11}$;

$\overset{(L)}{d}_1 = -\overset{(L)}{g}{}^2 a_1$; $\quad \overset{(L)}{d}_4 = 2a_2 \overset{(L)}{D}_1$; $\quad \overset{(T)}{d}_3 = 2a_2 \overset{(T)}{g} + 2a_4 \overset{(T)}{g}$;

$a_1 = C_{12}$; $\quad a_2 = (C_{11} - C_{12})/2$; $\quad a_4 = C_{44} - (C_{11} - C_{12})/2$;

C_{ij} are the moduli of elasticity.

The wave numbers $\overset{(L)}{g}$ and χ are defined as follows:

$$\overset{(L)}{g}{}^2 = A_1 - \sqrt{A_1^2 - A_2}\,;\ \chi^2 = 2\omega^2 \rho / (C_{11} - C_{12}), \tag{4}$$

where $A_1 = (C_{11} + C_{44})\omega^2 \rho / (2C_{11}C_{44})$; $A_2 = \omega^4 \rho^2 / (C_{11}C_{44})$; ρ is the density.

The formulae (3) and (4), obtained from the constitutive relations [3, 4], taking into account the assumptions on the position of the axes of symmetry of the material layers and the limitations on external load.

The common solution of Helmholtz equations for functions φ and ν is known:

$$\varphi = \sum_{m=0}^{\infty} \left[\varphi_m^+ H_m^{(1)}\left(\overset{(L)}{g}\, r \right) + \varphi_m^- H_m^{(2)}\left(\overset{(L)}{g}\, r \right) \right] \cos m\theta;$$

$$\nu = \sum_{m=0}^{\infty} \left[\nu_m^+ H_m^{(1)}(\chi r) + \nu_m^- H_m^{(2)}(\chi r) \right] \sin m\theta, \tag{5}$$

where φ_m^+, φ_m^-, ν_m^+, ν_m^- are the amplitudes of the *m*-th harmonic of the corresponding types of waves, traveling in opposite directions across the layers; $H_m^{(1)}$ and $H_m^{(2)}$ are the Hankel functions of the 1st and 2nd kind of *m*-th order.

When we define the fields at certain point *r* for each harmonic m and frequency ω, then the following condition is checked:

$$\omega << v_l m / r, \tag{6}$$

where v_l is the speed of quasi-longitudinal waves.

At violation of the condition (6), the functions φ and ν are presented in the form of solutions of the Laplace equations:

$$\varphi = \left(\varphi_m^+ r^m + \varphi_m^- \frac{1}{r^m} \right) \cos(m\theta);$$

$$\nu = \left(\nu_m^+ r^m + \nu_m^- \frac{1}{r^m} \right) \cos(m\theta). \tag{7}$$

This is due to the instability of the solution, caused by the presence of the singularity of the Hankel function for small arguments in the low-frequency part of the spectrum and considering a large number of spatial harmonics in the description of the pressure pulses, localized in small areas on the construction surface, when the Hankel functions of high order are used.

The calculation relationships to determine the fields of displacements and stresses in each layer were obtained in matrix form, similarly to those described in [4], with a subsequent transition from conjugate space to real space by performing the inverse Fourier transform.

The absorption of wave energy by the materials of the layers was set by adding to the wave numbers $\overset{(L)}{g}$ and χ imaginary components, $\overset{(L)}{g}{}''$ and χ'' being the absorption coefficients of the corresponding types of waves.

3. Results of numerical modeling at multipulse loading with given spatial distribution

By using the proposed method, we calculated distribution of the radial stresses $\sigma_{rr}(r,\theta)$ (see Fig. 2) in monolayer cylindrical structure ($r_1 = 1$ m; $r_0 = 0.1$ m; $\rho = 2700$ kg/m^3, $C_{11} = 107$ GPA; $C_{12} = C_{13} = 55.3$ GPA; $C_{44} = 25.9$ GPA; $\overset{(L)}{g}{}'' = 0.5$ m^{-1}; $\chi'' = 1$ m^{-1}) at time t, corresponding to the maximum amplitude for the given value r. These results were obtained on the outer surface of the construction at $r = r_1$ and at $r = 0.2$ m; upper and lower rows of plots in Fig. 2, respectively). Single pulse of pressure corresponds to Fig. 2 a, d and multiple pressure pulses with the duration of the $\tau = 2$ μs correspond to Fig. 2 b, c.

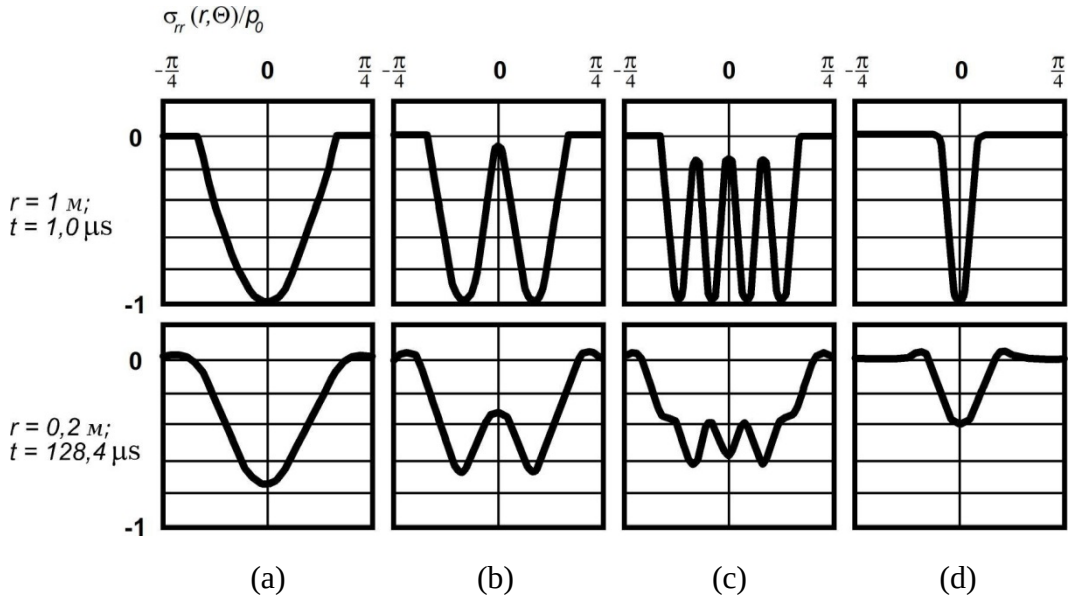

Fig. 2. Distributions of radial stresses $\sigma_{rr}(r,\theta)$ in the coordinate θ in the cylindrical construction: (a) $\tau_{\theta 1} = \pi/3$, $\Delta\theta_1 = 0$; (b) $\tau_{\theta 1} = \tau_{\theta 2} = \pi/6$, $\Delta\theta_1 = \Delta\theta_2 = \pm\pi/12$; (c) $\tau_{\theta 1} = \tau_{\theta 2} = \tau_{\theta 3} = \tau_{\theta 4} = \pi/12$, $\Delta\theta_3 = \Delta\theta_4 = \pm\pi/8$; (d) $\tau_{\theta 1} = \pi/12$, $\Delta\theta = 0$.

The integration was carried out, using the method of fast Fourier transform at $K = 12$ ($2^K = 4096$ is the section number of partitioning the integration interval).

The distribution of the radial stresses $\sigma_{rr}(r,\theta)$, shown in Fig. 2, were obtained for: (a) $\tau_{\theta 1} = \pi/3, \Delta\theta_1 = 0$; (b) $\tau_{\theta 1} = \tau_{\theta 2} = \pi/6, \Delta\theta_1 = \Delta\theta_2 = \pm\pi/12$; (c) $\tau_{\theta 1} = \tau_{\theta 2} = \tau_{\theta 3} = \tau_{\theta 4} = \pi/12$, $\Delta\theta_3 = \Delta\theta_4 = \pm\pi/8$; (d) $\tau_{\theta 1} = \pi/12$, $\Delta\theta = 0$.

Analysis of the simulation results (see Fig. 2) shows that at simultaneous loading by multiple pressure pulses, the pressure pulses with a small length τ_θ expand and merge due to the diffraction, at the far distance from the place of the pulse application (the external surface of the construction). The stress amplitude in this case is close to the load amplitude of a single pressure pulse with a large τ_θ.

Figure 3 shows the distributions $\sigma_{rr}(\theta)$, obtained at the interface ($r = r_1$) of the layers in two-layered cylindrical construction ($r_2 = 0.5$ m; $r_1 = 0.2$ m; $r_0 = 0.1$ m) at different times t. These moments of time correspond to the maximum amplitudes at pulsed loading with parameters similar to shown in Fig. 2d (Fig. 3a) and Fig. 2c (Fig. 3b).

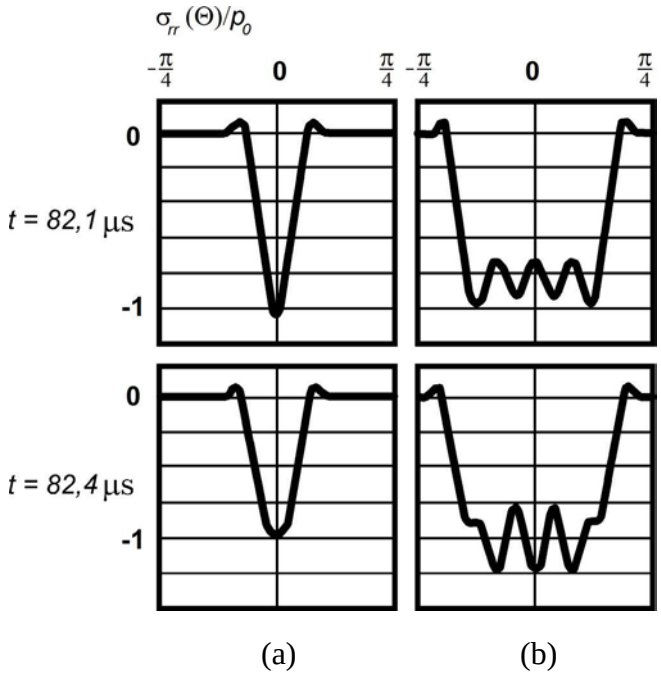

Fig. 3. Distributions of radial stresses $\sigma_{rr}(\theta)$ in the coordinate θ at the interface between layers ($r = r_1$) in two-layer cylindrical construction.

Physical-mechanical characteristics of the material of the inner layer coincided with those described above, and for the outer layer they had the following values: $\rho = 1400$ kg/m^3; $C_{11} = 19.2$ GPA; $C_{12} = C_{13} = 8$ GPA; $C_{44} = 5.6$ GPA; $g^{(L)''} = 1$ m^{-1}; $\chi'' = 2$ m^{-1}.

Analysis of these distributions shows that due to the interference, the time, corresponding to the maximum amplitude at simultaneous loading by multiple pulses of pressure, occurs later than at loading by single pulse of pressure.

4. Results of numerical modeling at multipulse loading with given temporal distribution

We studied the stress-strain state at multipulse loading with a given temporal distribution by using the proposed method. The dependences of radial stress $\sigma_{rr}(t)$ were calculated at the interface between layers ($r = r_1$) in two-layer cylindrical construction ($r_2 = 1.2 \cdot 10^{-2}$ m;

$r_1 = 6.0 \cdot 10^{-3}$ m; $r_0 = 3.0 \cdot 10^{-3}$ m, the relative thickness of the construction $\alpha = 0.75$, where $\alpha = (r_2 - r_0)/r_2$ [5]), at pulse loading (every pressure pulse is present in the form of the Gauss function with a duration of $\tau = 0.5$ μs with semi-sine shape on the outer surface ($r = r_2$) of a duration $\tau_\theta = \pi$, $\Delta\theta = 0$).

Physical-mechanical properties of materials of external and internal layers and the integration parameters coincide with the described in Section 3.

Figure 4 shows dependence of radial stress $\sigma_{rr}(t)$ at the interface between layers ($r = r_1$) in a two-layer cylindrical construction at loading by a single pulse of pressure in the form of the Gauss function. The upper part of the plot presents the temporal distribution of pulsed load on the outer surface of the construction ($r = r_2$).

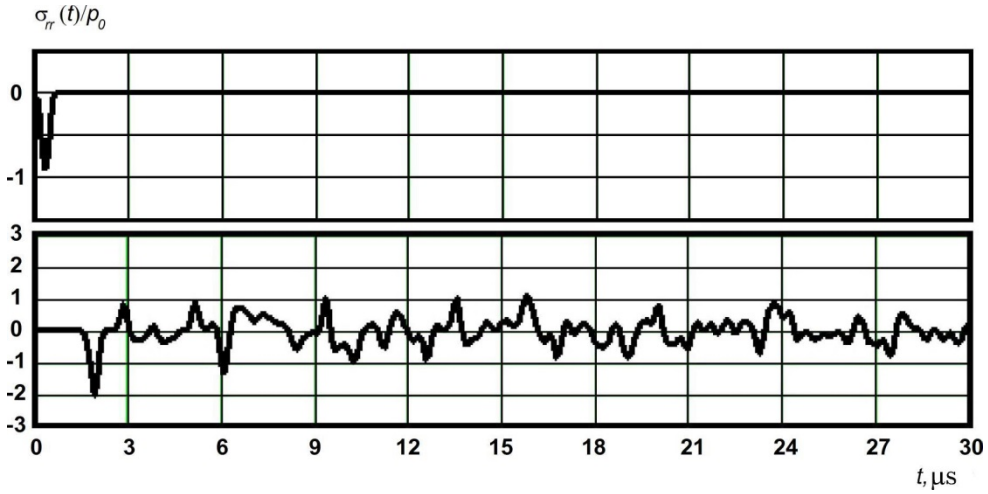

Fig. 4. Dependence of $\sigma_{rr}(t)$ at the interface between layers ($r = r_1$) in two-layer cylindrical construction at loading by single pulse of pressure in the form of Gauss function.

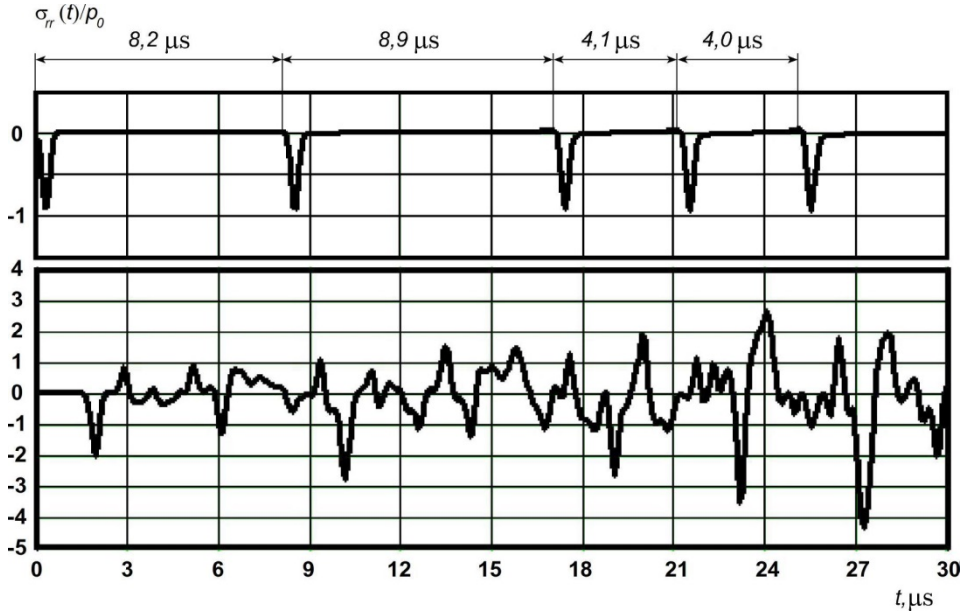

Fig. 5. Dependence $\sigma_{rr}(t)$ at the interface between layers ($r = r_1$) in two-layer cylindrical construction at repeated loading by pulses of pressure in the form of Gauss function.

Figure 5 shows the dependence of the radial stress $\sigma_{rr}(t)$ at the interface between layers ($r = r_1$) in two-layer cylindrical construction with repeated impacts of pressure pulses in the form of the Gauss function (5 identical pulses of pressure applied to the outer surface of the construction at time $t_1 = 0$ μs, $t_2 = 8.2$ μs, $t_3 = 17.1$ μs, $t_4 = 21.2$ μs, $t_5 = 25.2$ μs). The upper part of the plot presents the temporal distribution of pulsed impact on the outer surface of the construction ($r = r_2$).

The pointed temporal distribution of the pressure pulses is given in accordance with the recommendations of [5, 6], to achieve the maximum values of radial stresses $\sigma_{rr}(t)$ at the interface between layers ($r = r_1$) in the considered construction at limited number of pressure pulses. In this case, the pressure pulses were applied at intervals of time equal to the time intervals between maximum values of the radial stresses $\sigma_{rr}(t)$ of the same sign, obtained on dependence for the case of loading by a single pulse (see Fig. 4), but the order of application of these pulses must be reversed.

The analysis of these dependences shows that at a given temporal distribution of pulse impact, an increase by 4.3 times in the amplitude of the maximum radial stress takes place on the boundary of layers, compared to the maximum radial stress calculated for the case of single pulse of pressure.

The maximum amplitude of the radial stresses at the interface between layers of the construction may be increased up to 7.2 times compared to the maximum radial stresses, calculated for the case of single pulse of pressure, by using pressure pulses of rectangular shape instead of Gauss dependence.

Figure 6 shows dependence of change of radial stress $\sigma_{rr}(t)$ with time t at the interface between layers ($r = r_1$) in a two-layer cylindrical structure at loading by pressure pulse of a rectangular shape, and Fig. 7 presents a similar dependence with repeated loading by pressure pulses of rectangular shape. The upper part of the plots presents the time distribution of pulsed load on the outer surface of the structure ($r = r_2$) for each of the calculated cases.

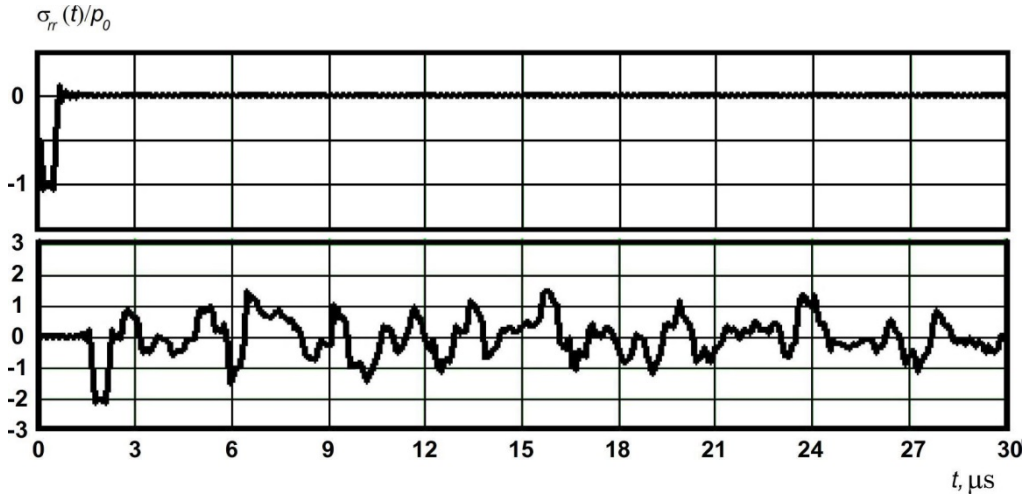

Fig. 6. Dependence $\sigma_{rr}(t)$ at the interface between layers ($r = r_1$) in two-layer cylindrical construction at loading by single pulse of pressure with rectangular shape.

The results of the numerical simulations clearly illustrate the features of the stress-strain state in layered cylindrical structures made of transversely isotropic materials under pulsed loading with a given spatial-temporal distribution and agree well with the results, published in the known papers, for example in [5, 6].

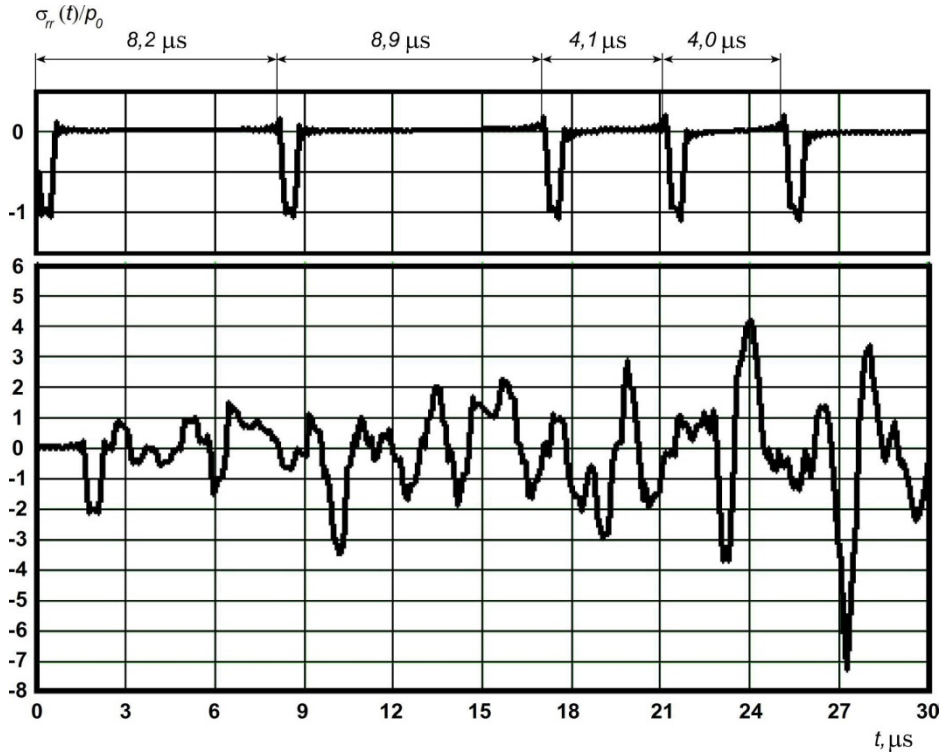

Fig. 7. Dependence $\sigma_{rr}(t)$ at the interface between layers ($r = r_1$) in two-layer cylindrical construction at repeated loading by pressure pulses of rectangular shape.

5. Conclusion

The results of calculations allow us to make conclusion on possibility of the application of developed method of calculating stress-strain state in layered cylindrical constructions, subjected to multiple local dynamic loads with high accuracy and taking into account the peculiarities of arising wave processes.

The above-described results is most appropriate to use at *a priori* and *a posteriori* analysis of the results of state diagnostics for advanced constructions made of new anisotropic layered composite materials, by using acoustic methods of nondestructive testing in mechanical engineering, shipbuilding, aircraft construction, etc.

Acknowledgement. *This research is supported by the Ministry of Education and Science of the Russian Federation and grant of the Russian Foundation for Basic Research № 16-08-00740.*

References

[1] I.P. Miroshnichenko, In: *Advanced Materials – Techniques, Physics, Mechanics and Applications. Springer Proceedings in Physics*, ed. by Ivan A. Parinov, Shun-Hsyung Chang, Muaffaq A. Jani (Springer Cham, Heidelberg, New York, Dordrecht, London, 2017), Vol. 193, p. 435.

[2] R.M. Christensen, *Mechanics of Composite Materials* (John Wiley & Sons, New York, 1979).

[3] V.P. Sizov // *Mechanics of Solids* **5** (1988) 55.

[4] V.P. Sizov, I.P. Miroshnichenko, *Excitation of Elastic Waves in Layered Anisotropic Structures* (LAP LAMBERT Academic Publishing, Saarbrucken, Germany, 2012).

[5] A.M. Petrov, V.P. Sizov // *Izvestiya VUZov. Mechanical Engineering* **2** (1985) 22.

[6] V.P. Sizov // *Izvestiya VUZov. Mechanical Engineering* **7–9** (1991) 33.

Materials Physics and Mechanics 37 (2018) 192-197 Received: December 22, 2017

ANALYSIS OF OSCILLATION FORMS AT DEFECT IDENTIFICATION IN NODE OF TRUSS BASED ON FINITE ELEMENT MODELING

A.N. Soloviev[1,2,3], I.A. Parinov[1], A.V.Cherpakov[1,3]*, Yu.A. Chaika[1,2], E.V. Rozhkov[1]

[1]Southern Federal University, Rostov-on-Don, Russia

[2]Southern scientific center of RAS, Rostov-on-Don, Russia

[3]Don State Technical University, Rostov-on-Don, Russia

*e-mail: alex837@yandex.ru

Abstract. The finite element modeling of the truss structure in ANSYS software is considered. The problem of the identification of defects in the truss rod construction was considered on the base of an analysis of the parameters of the vibration modes. A truss rod construction with two defects was modeled. The deflection and curvature of the vibration modes are analyzed. Defective elements are represented in the form of a change in the construction parameter of cross-section, localized in the vicinity of one of the junction nodes of the truss and fastening the rod. Modal analysis of the structure is carried out. The dependence of the eigen-frequencies and parameters of the vibration modes on the magnitude of the defect is considered. The analysis shows that the modal identification signs allow us to identify the defective node in the construction.

Keywords: truss structure; finite element modeling; ANSYS; oscillation forms; identification of defects; modal analysis.

1. Introduction

Some theoretical and experimental research approaches, and developed techniques for vibration diagnostics of rod structures are present in [1 – 5]. Analysis of this area allows us to make conclusions about its sufficient relevance.

In majority works, simple structural elements of a rod full-body or tube configuration with various structural defects are investigated, the most applicable of which is the defect model of crack-like configuration. Numerical analytical and experimental methods are used to analyze the vibration parameters and solve identification problems [5 – 8]. The most common method of identification is the use of resonance methods of free and forced oscillations and in part acoustic methods of control. Some modern approaches and algorithms to solve the problem of identifying defects, based on vibration diagnostics methods are present in [8 – 13]. The authors in these publications represent the solution of diagnostic problems, which is based on the use of correlation relationships between the parameters of the frequency spectrum of vibrations and the magnitude of damage to construction elements. In these studies, simple elements of the rod configuration are investigated. Approaches to the evaluation of damage, designs, based on the analysis of natural frequencies are an indirect sign of the assessment and cannot be applied to an accurate determination of the amount of damage to its elements.

http://dx.doi.org/10.18720/MPM.3722018_12

A more accurate method for identifying the parameters of defects is the method, based on the analysis of natural oscillations, and also the application of evolutionary algorithms presented, for example in [14, 15]. This approach allows us to find not only the magnitude, but also the exact localization of the defect in single construction element. Examples of modeling and analysis of vibrations of truss constructions with damage are present in [16 – 18].

The aim of the work is the identification of defects in the model of bridge truss construction with the rod configuration of its elements, based on the analysis of natural frequencies and vibration modes, using the finite element method in finite-element ANSYS software.

2. Modeling

As a research object, a model of a section of a bridge truss structure with rod elements was chosen (Fig. 1). The model of the truss structure can have multiple defects, located in certain nodes. The model has rigid fixation of displacements in all directions in the support nodes 3 and 4 of the fixing; moreover, vertical displacements are fixed in the nodes 1 and 2 of the model. At simplified modeling in ANSYS software, a rod-type finite element of the *Beam188* type is used as a structural element. The element is constructed on the base of the application of the Tymoshenko beam hypothesis. The cross-section of the element is rectangular full-bodied and have the sizes: a length of rod element is L = 250 mm, a height of cross-section is h = 8 mm, a width is b = 4 mm). Defects were modeled as a reduction in the cross-section on height and have a width of l_d = 1 mm, in the vicinity of the node of one of the rods of the lower belt of the construction (Fig. 1). The magnitude of the defect was calculated as the ratio of the height of the damaged (residual) cross-section to the original one: $t_d = (h - h_d)/h$.

For symmetry in the ZOX plane, the construction had two defects of the same configuration on both sides.

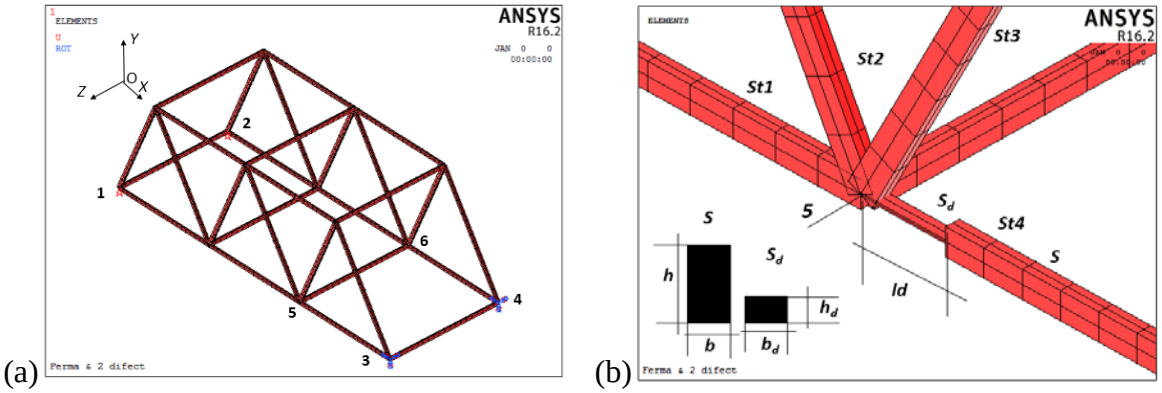

Fig. 1. Scheme of the model of truss construction (a) and the node with the defect model (b).

3. Model description

The natural oscillations of the model are considered and compared in two cases: (i) without damage at the nodes, and (ii) existence of defects with a size t_d = 0.875. The first ten eigen-frequencies were calculated with the defect value (Table 1). Forms of oscillations of the model are constructed, and deflections and curvature of the construction are obtained at the first eigen-mode of the oscillations. The analysis of the results shows that for the case with two defects in given places, the frequencies of the first 10 modes of oscillation vary within the range $\Delta\omega$ = – 0.32 to – 1.65%.

Figure 2 shows the first 10 forms of the eigen-modes of the vibrations of the defect model. Analysis of vibration modes shows that 1 – 6 modes of natural modes of the model differ from 7 – 10 modes of oscillations in that all the nodes of the model are displaced. For 7 – 10 oscillation modes, the nodes have minimal spatial displacements.

In the next step, the deformations in the direction of *z*-axis of the points of the rod truss were calculated at the first mode of oscillation in the vicinity of node 5, and the deflections and curvature were compared for the two cases of the models of the construction considered.

Table 1. Proper defect frequencies and their relative values.

Mode, i	Natural frequencies ω_i (Hz)		Relative frequencies
	$t_d = 0$	$t_d = 0.875$	$\Delta\omega_i$ (%)
1	11.05	10.9	–1.33
2	34.67	34.1	–1.65
3	57.08	56.9	–0.32
4	57.47	57.1	–0.64
5	76.12	75.3	–1.07
6	79.12	78.6	–0.65
7	161.02	159.4	–1.01
8	161.95	160.4	–0.96
9	179.43	177.0	–1.35
10	188.03	185.6	–1.29

Figures 2 and 3 show the projections on *x*-axis of the amplitudes of the vibration modes and the curvature of the first mode for rods near the node 5. The *x*-axes of the graphs shows the coordinates of the points for the oscillation amplitudes; along *y*-axes of the graphs, the projections of the amplitude values of the waveforms and curvature in the *z*-direction of the construction are presented.

Analysis shows that near node point, the oscillation amplitude difference in the *z*-direction for four rods is minimal, as can be seen from the graphical representation of the vibration forms (Fig. 3). At the same time, the analysis of the plots of curvature forms in the *z*-direction (Fig. 4) shows some discrepancy between the plots when their intersection point is restored. This sign may be sufficient grounds for detecting a defect in a construction node.

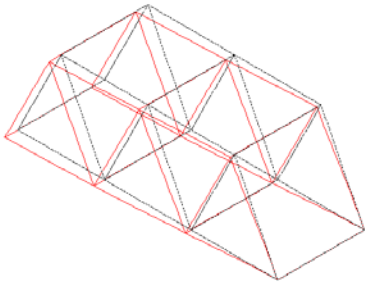

1 mode, ω_1 = 10.9 Hz

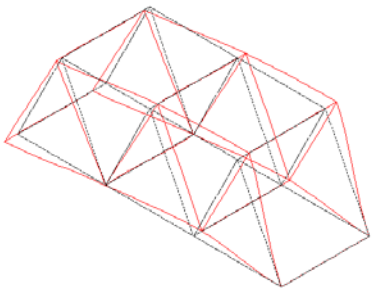

2 mode, ω_2 = 34.2 Hz

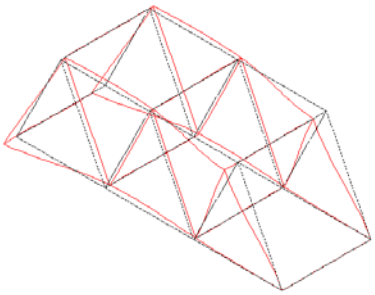

3 mode, ω_3 = 56.9 Hz

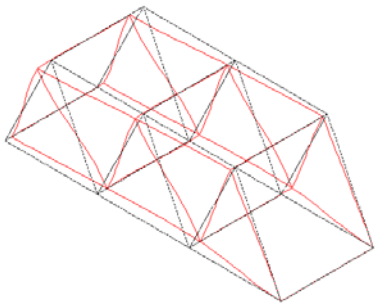

4 mode, ω_4 = 57.0 Hz

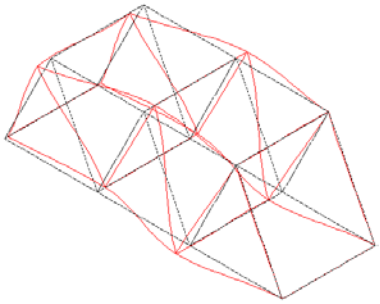

5 mode, ω_5 =75.3 Hz

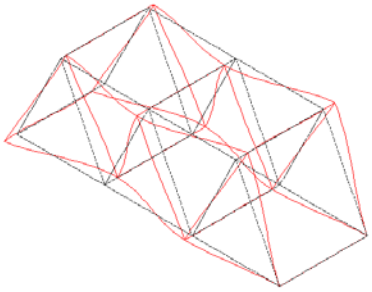

6 mode, ω_6 = 78.6 Hz

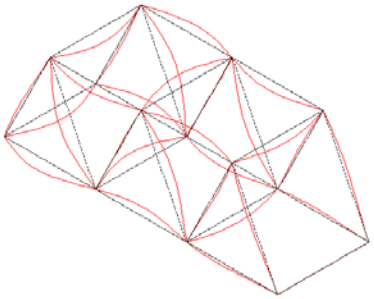

7 mode, ω_7 = 159.3 Hz

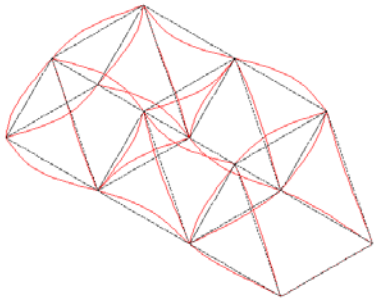

8 mode, ω_8 = 160.4 Hz

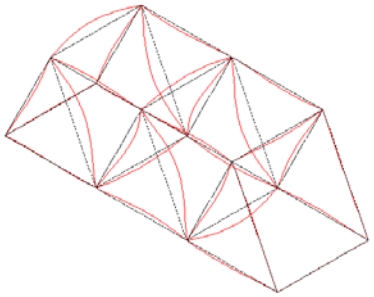

9 mode, ω_9 = 177.0 Hz

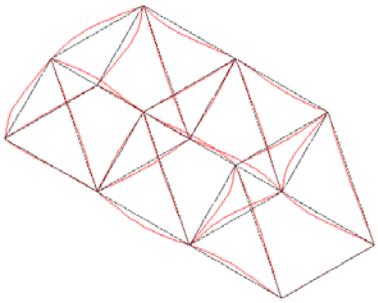

10 mode, ω_{10} = 185.6 Hz

Fig. 2. Eigen-forms for 10 modes of vibrations of the truss structure.

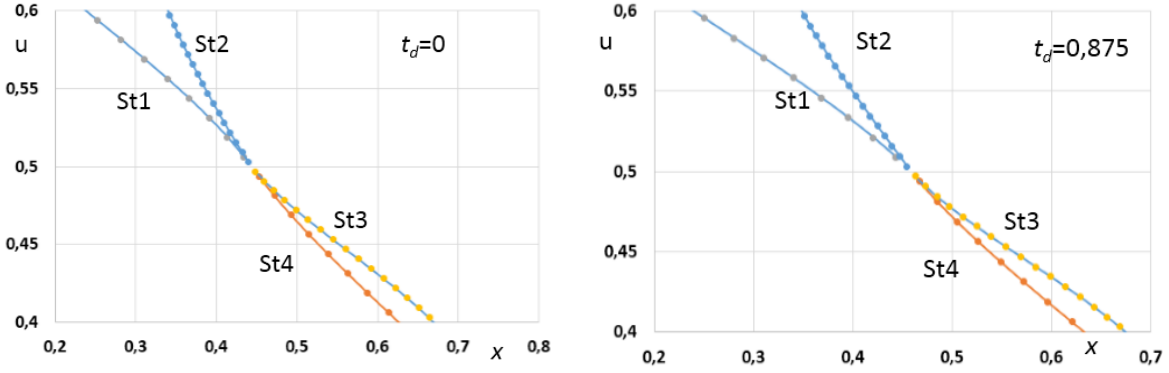

(a) (b)

Fig. 3. Shapes of the structure in *z*-direction near the node 5 for two cases of models.

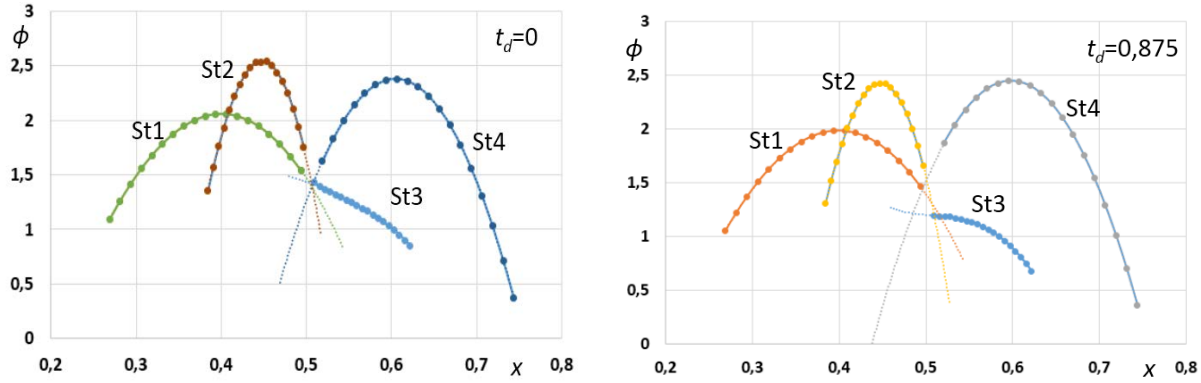

(a) (b)

Fig. 4. Curvature of vibration mode 1 in *z*-direction of the rod construction near the node 5 with two versions of models: (a) without defect; (b) with defects.

Conclusions

The study of vibration in truss rod construction can be applied to the assessment of the presence of defects in a construction node. At the beginning investigation of the curvature of the oscillation forms of the truss at various vibration modes, nodes with defects can be identified. The analysis of the curvature parameters can be applied to the evaluation of the damage value in the rod junction assembly.

Acknowledgements. *The work was carried out with the partial support of the Ministry of Education and Science of Russian Federation (No. Bch0110-11/2017-20), and RFBR (Nos. 16-08-00740, 17-08-00621, 17-08-01373).*

References

[1] Mohammad H.F. Dado, Omar A. Shpli // *Int. J. Solid and Structures* **40** (2003) 5389.
[2] M.I. Friswell // *Phil. Trans. R. Soc. A* **365** (2007) 393.
[3] A.O. Vatulyan, A.N. Soloviev, *Direct and Reverse Problems for Homogeneous and Heterogeneous Elastic and Electroelastic Solids* (Southern Federal University Press, Rostov-on-Don, 2008). (In Russian).
[4] V.A. Akopyan, E.V. Rozhkov, A.N. Soloviev, S.N. Shevtsov, A.V. Cherpakov, *Identification of Damages in Elastic Constructions: Approaches, Methods, Analysis* (Southern Federal University Press, Rostov-on-Don, 2015). (In Russian).

[5] A.V. Cherpakov, *Identification of Defects in Rod Constructions, Based on the Analysis of Vibration Parameters* (PhD Thesis, Don State Technical University, Rostov-on-Don, 2013).
[6] A.V. Cherpakov, A.N. Soloviev, V.V. Gritsenko, O.U. Goncharov // *Defence Science Journal* **66(1)** (2016) 44.
[7] M.A. Ilgamov, A.G. Khakimov // *Defectoscopy* **6** (2009) 83. (In Russian)
[8] O.V. Bocharova, V.A. Lyzhov, I.E. Andzhikovich // *News of SSC RAS* **9(2)** (2013) 11.
[9] A.V. Cherpakov, V.A. Akopyan, A.N. Soloviev // *Technical Acoustics* **13** (2013) 1.
[10] A.V. Cherpakov, V.A. Akopyan, A.N. Soloviev, E.V. Rozhkov, S.N. Shevtsov // *News of Don State Technical University* **11(3)** (2011) 312. (In Russian)
[11] A. Cherpakov, I. Egorochkina, E. Shlyakhova, A. Kharitonov, A. Zarovny, S. Dobrohodskaya // *MATEC Web of Conferences* **106** (2017) 04009.
[12] V. Akopyan, A. Soloviev, A. Cherpakov, In: *Mechanical Vibrations: Types, Testing and Analysis*, ed. by A.L. Galloway (Nova Science Publishers, N.-Y., 2011), p. 147.
[13] V.A. Akopyan, A.N. Kabelkov, A.V. Cherpakov // *University News. North-Caucasian Region. Technical Sciences Series* **5** (2009) 89. (In Russian)
[14] V.A. Akopyan, A.N. Soloviev, A.V. Cherpakov, S.N. Shevtsov // *Russian Journal of Nondestructive Testing* **49(10)** 579 (2013).
[15] A.A. Krasnoshchekov, B.V. Sobol, A.N. Soloviev, A.V. Cherpakov // *Russian Journal of Nondestructive Testing* **47(6)** (2011) 412.
[16] O.A. Burtseva, S.A. Chipco, O.K. Kaznacheeva, A.V. Cherpakov // *European Journal of Natural History* **4** (2012) 39.
[17] V.A. Akopyan, A.N. Soloviev, A.N. Kabelkov, A.V. Cherpakov // *University News. North-Caucasian Region. Technical Sciences Series* **1** (2009) 55. (In Russian)
[18] A.N. Soloviev, A.V. Cherpakov, I.A. Parinov, In: *Proc. of the 2015 Int. Conference on Physics and Mechanics of New Materials and Their Applications*, ed. by Ivan A. Parinov, Shun-Hsyung Chang, Vitaly Yu. Topolov (Nova Science Publishers, N.-Y., 2016), p. 515.

Materials Physics and Mechanics 37 (2018) 198-204 Received: December 22, 2017

MICROSTRUCTURE MODELLING OF BOTTOM ASH REINFORCED ALUMINUM METAL MATRIX COMPOSITE WITH STRESS RELAXATION

M. Abdulrahim*, Herlina, V.E.S. Pratiwi

Department of Industrial Engineering, University of 17 Agustus 1945 Surabaya, Indonesia

*e-mail: muslimin@untag-sby.ac.id

Abstract. It is studied stress relaxation at microstructure modeling, in particular percentage of rolling reduction and relaxation time at forming microstructure. For the specimen ingot is given a stress in hot-rolling method at temperature of 250 °C. The variable parameter is 1, 2 and 3% bulk reduction during rolling; loading duration is 0.5 – 3.5 s. Tensile test is used to measure the tensile strength. Knowing the initial time of grain formation, we state the initial and final moments of precipitate during recrystallization. The microstructure analysis is performed by using Scanning Electron Microscopy (SEM). The research results show that in the case of 1% bulk reduction during rolling, there is a microstructure recovery in the first 0.5 s, then recrystallization begins via 1 sec, the beginning of precipitation takes place after 1.5 s, and grain growth begins after 2.5 s. Corresponding results for 2% bulk reduction during rolling: recrystallization begins via 0,5 s, the beginning of precipitation takes place after 1 sec, and grain growth begins after 2.5 s. The results for 3% bulk reduction during rolling: the beginning of precipitation takes place after 0.5 sec, and grain growth begins after 1.5 s.
Keywords: microstructure modeling; stress relaxation; Scanning Electron Microscopy (SEM).

1. Introduction

The mechanical properties and microstructure formation are strongly influenced by the process of precipitation and grain size in final material microstructure, for which control and prediction of precipitation and recrystallization are necessary. One of the techniques that is cheap and produces accurate predictions is the stress relaxation technique [1].

The advantage of this microstructure modeling/prediction process is that cost of final good can be calculated [2]. Based on the microstructure modeling, we define: the grain size, the precipitate formed, the stress relaxation curve, the precipitation time and the crystallization time.

Composite materials as alternative materials are developed very rapidly. Some their advantages include: light, low and stable at high temperatures coefficient of thermal expansion (CTE).

The performed simulation process was able to control and predict changes in microstructure during the manufacture and to estimate the mechanical properties of the final good. This is very advantageous in planning the process of making the composite "Al 6061 - coal ash" due to reducing the cost of the "trial – error" process.

By using the methods of metallurgical physics, rolling technology, prediction and control of microstructure changes can be carried out quickly and precisely. One of the

http://dx.doi.org/10.18720/MPM.3722018_13

developed microcontrol structure technology is so-called the Structure Property Prediction and Control (SPPC) technique, which accelerates production process, reduces manufacturing cost and improves quality of good. The developed mathematical modelling the formation process of "Al 6061 – coal ash" includes modelling microstructure changes, namely grain growth and precipitation process [2]. To estimate of microstructure changes during thermomechanical manufacture process, many test methods have been applied. One of these method for optimization of thermo-mechanical processes is so-called stress relaxation [3].

2. Methods

Figure 1 shows a flowchart of the developed experiment.

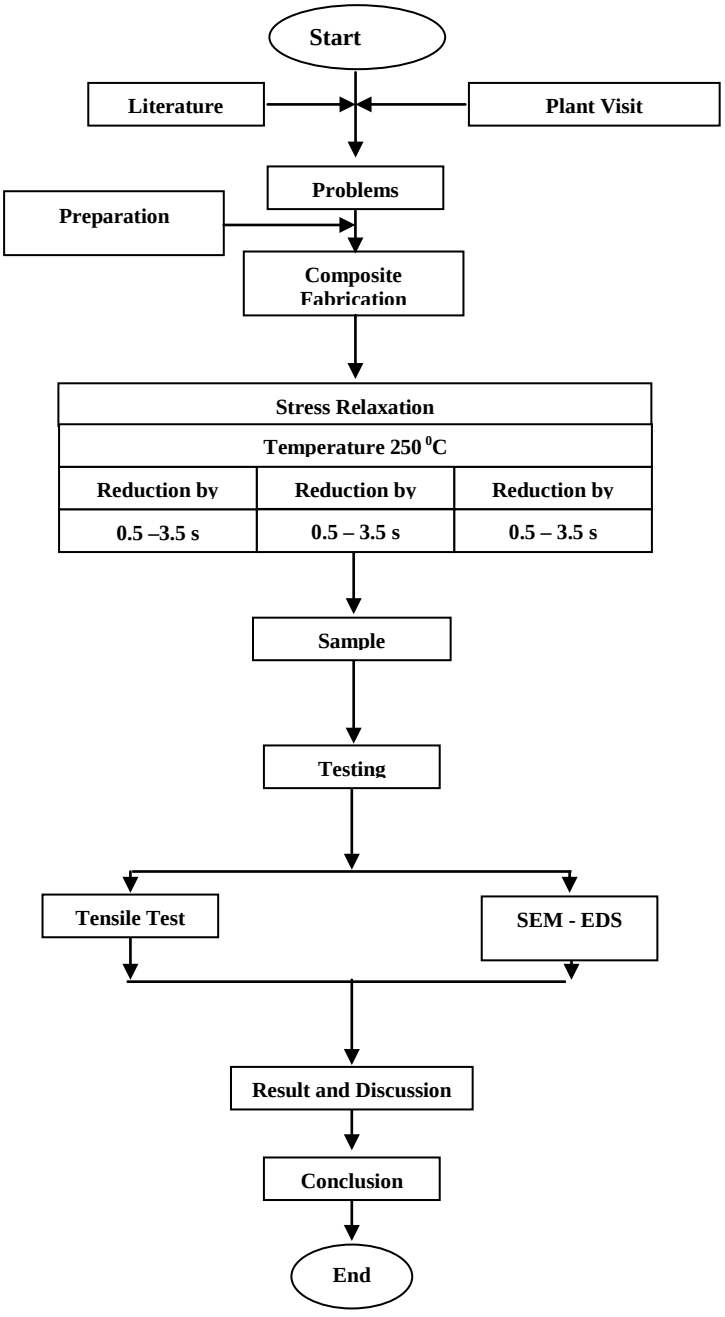

Fig. 1. Flowchart diagram of experiment.

3. Results and Analysis

The obtained results of tests on bulk reduction, stress relaxation at different stage of hot rolling are present in Tables 1 – 3 and Figs. 2 – 5.

Table 1. Tensile test results after hot rolling for 1% bulk reduction and stress relaxation time 0.5 – 3.5 s.

Relaxation (s)	Diameter (mm)	Square (mm^2)	Load (kgF)	Tensile Stress (kgF/mm^2)
0.5	4.9	18.848	163	8.648
0.7	5.0	19.625	168	8.561
1.0	4.6	16.611	145	8.701
1.2	4.9	18.848	135	7.163
1.5	5.0	19.625	131	6.675
1.7	5.2	21.226	168	7.915
2.0	4.8	18.086	167	9.233
2.2	5.3	22.051	199	9.025
2.5	4.9	18.848	186	9.868
2.7	4.6	16.611	148	8.910
3.0	5.2	21.226	144	6.784
3.2	4.7	17.341	112	6.459
3.5	5.0	19.625	114	5.809

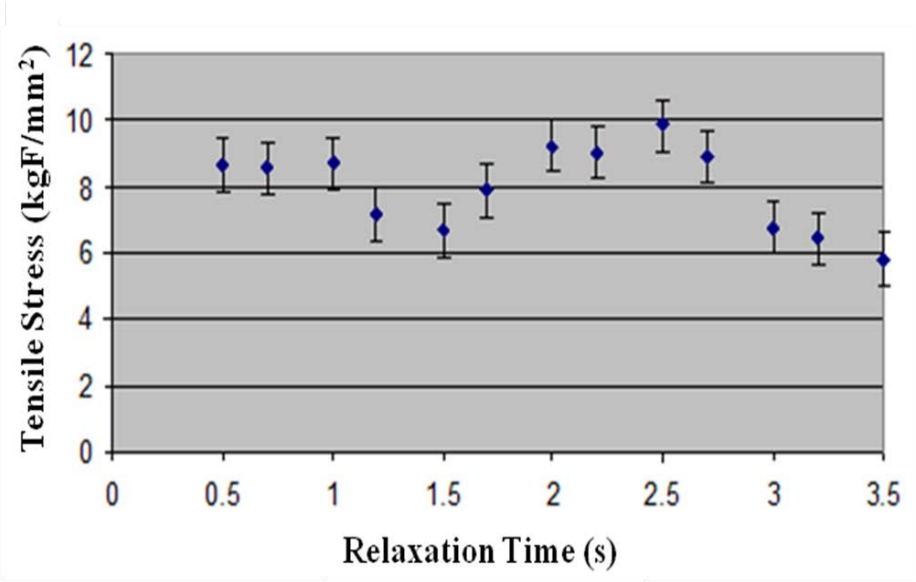

Fig. 2. Tensile stress *vs* relaxation time in 1% bulk reduction.

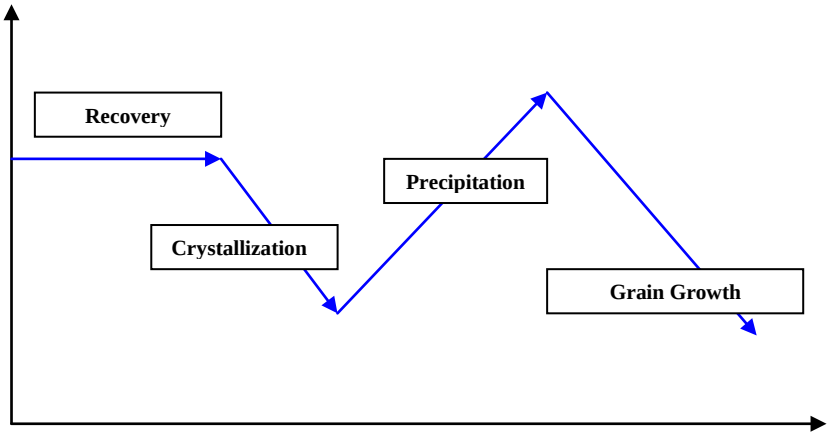

Fig. 3. Scheme of Stress Relaxation.

Table 2. Tensile test results after hot rolling for 2% bulk reduction, stress relaxation time 0.5 – 3.5 s.

Relaxation time (s)	Diameter (mm)	Square (mm^2)	Loads (kgF)	Tensile Stress (kgF/mm^2)
0.5	4.8	18.086	122	6.745
0.7	4.9	18.848	120	6.367
1.0	5.1	20.418	112	5.485
1.2	4.8	18.086	135	7.464
1,5	5.0	19.625	164	8.357
1.7	4.7	17.341	175	10.092
2.0	4.9	18.848	181	9.603
2.2	5.2	21.226	220	10.364
2.5	5.2	21.226	237	11.165
2.7	5.0	19.625	196	9.987
3.0	4.7	17.341	174	10.034
3.2	5.1	20.418	160	7.836
3.5	5.0	19.625	158	8.051

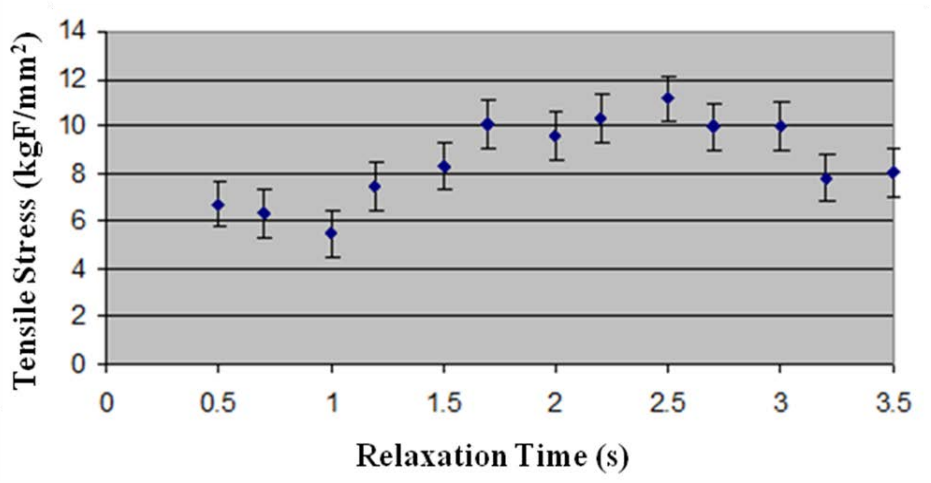

Fig. 4. Tensile stress *vs* relaxation time in 2% bulk reduction.

Table 3. Tensile test results after hot rolling for 2% bulk reduction, stress relaxation time 0.5 – 3.5 s.

Relaxation time (s)	Diameter (mm)	Square (mm^2)	Loads (kgF)	Tensile Stress (kgF/mm^2)
0.5	5.0	19.625	124	6.318
0.7	4.7	17.341	118	6.805
1.0	4.8	18.086	130	7.188
1.2	5.0	19.625	158	8.051
1.5	5.2	21.226	184	8.668
1.7	5.0	19.625	165	8.408
2.0	4.9	18.848	146	7.746
2.2	4.8	18.086	135	7.464
2.5	5.0	19.625	136	6.930
2.7	5.0	19.625	122	6.217
3.0	5.0	19.625	124	6.318
3.2	5.2	21.226	119	5.606
3.5	5.0	19.625	104	5.299

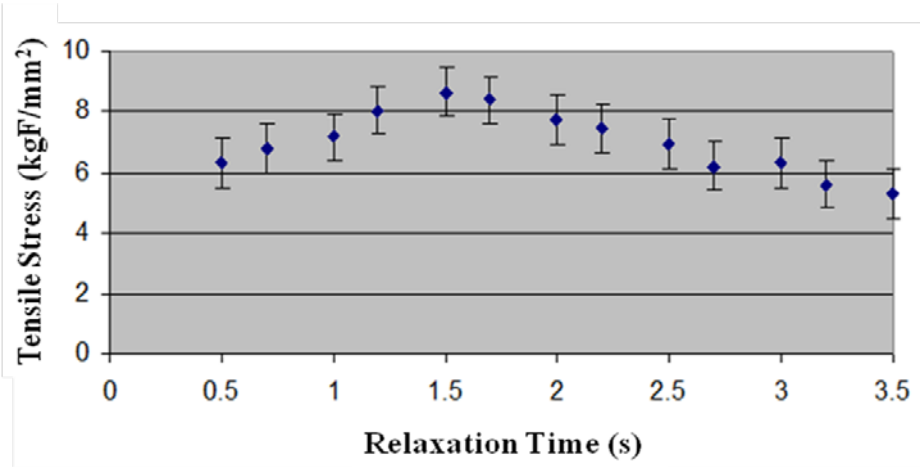

Fig. 5. Tensile stress *vs* relaxation time in 3% bulk reduction.

From the above tensile stress and relaxation data it can be concluded that in the range from 0.5 to 1 s, microstructure recovery takes place and recrystallization occurs from 1 to 1.5 s, and during 1.5 to 2.5 s occurs precipitation, but grain growth takes place from 2.5 to 3.5 s. The stress relaxation occurs after heating the specimen to a temperature of 250 °C ($0.4 – 0.5T_m$, where T_m is the melting point), then the relaxation process continues during from 0.5 to 3.5 s in following quenching.

The improvement of relaxation process could be caused by the hardening due to the formation of precipitates into matrix. The strength of the aging hardening alloy is determined by the interaction between moving dislocations and precipitates [2]. Barriers to precipitation in hardening alloys that block the movement of dislocations may be caused by: (i) strain around the precipitation zone and (ii) itself the zone or precipitate or both factors.

Clearly, that if the zone plays the main role, then the moving dislocations must cut it or move around it. Therefore, there are at least three causes of hardening, namely:

1. coherent hardening due to strain coherency;
2. chemical hardening, when dislocations cut precipitates;
3. dispersion hardening, when the dislocations move around or over the precipitates.

Figure 6 compares microstructure morphologies of various specimens.

Effect of bulk reduction during rolling could be estimated at morphology comparisons of samples. Fig. 6 presents example of morphology changes at 1% rolling reduction during 0.5 – 3.5 s. Effect of rolling reduction on recrystallization time can be estimated from the results for tensile stresses, presented in Figs. 2, 4 and 5. We can conclude that the percentage of rolling reduction, experienced by a material, greatly affects recrystallization time. The greater the rolling reduction leads to the acceleration of material recrystallization.

By knowing the time of recrystallization we can define the spacing between rollers at absence of material changes due to the precipitate formation during recrystallization. So we can adjust the distance between first and second rollers, taking into account that this distance should be overcome by the rollers for time no exceeding 1 s for 1% reduction, 0.5 s for 2% reduction, and from 0 to 0.5 s for 3% reduction.

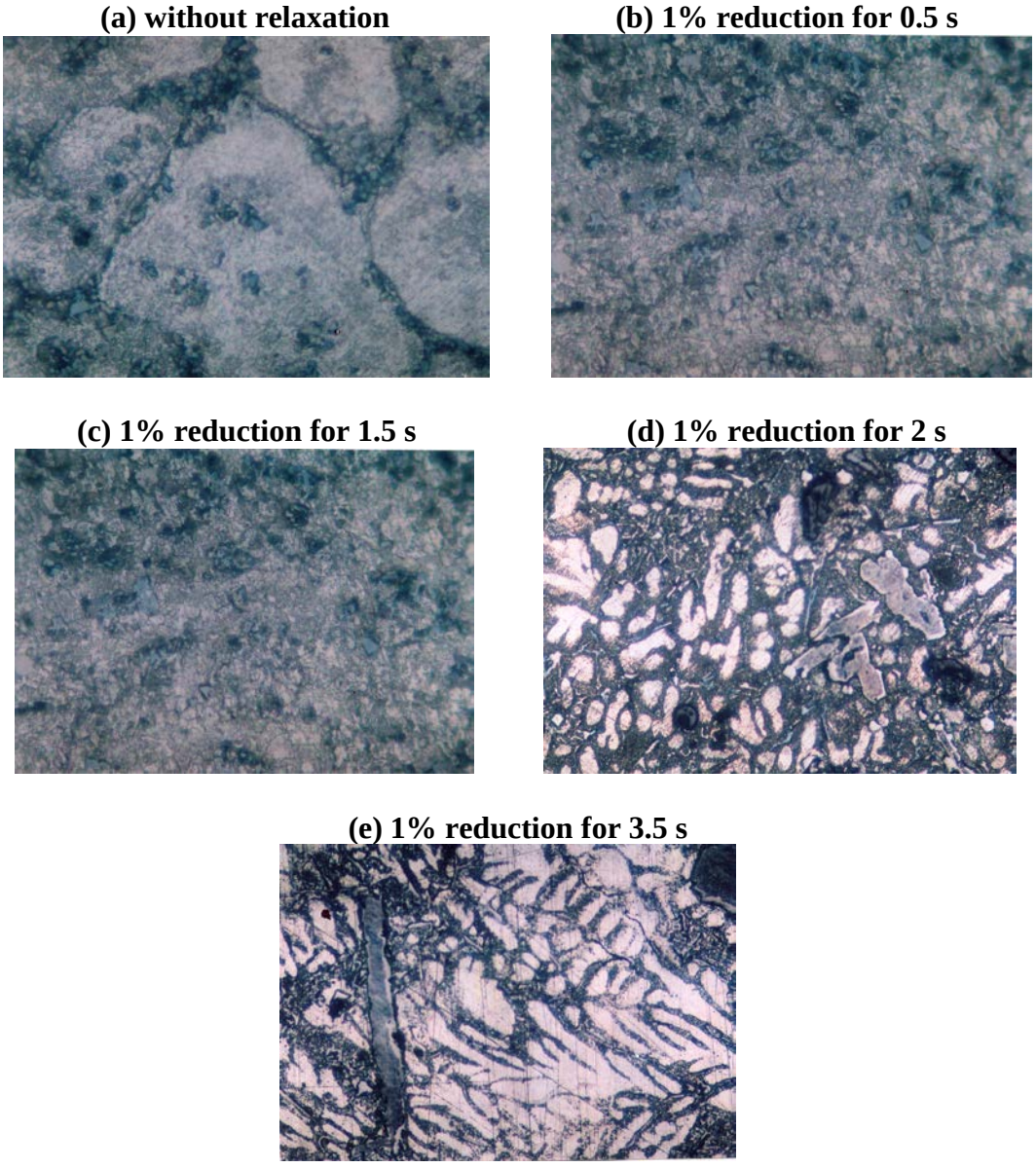

Fig. 6. Morphology comparison of samples.

4. Conclusion

1. The higher the bulk reduction by rolling, the faster recrystallization will take place.
2. From the morphology of microstructure, we can see the precipitate, formed by carbon, aluminum, and silicon.
3. By knowing recrystallization time, we can adjust the distance between rollers and determine the optimal value of the bulk reduction.

References

[1] R.W. Cahn, *Structure and Properties of Composites* (VCH, New York, 1993).
[2] E.S. Siradj // *Jurnal Universitas Indonesia* **XXXI** (2001) 5.
[3] E.S. Siradj // *Jurnal Teknologi Universitas Indonesia* **3** (1997).
[4] George E. Dieter, *Metalurgi Mekanik* (Pt Gelora Aksara Pratama, Jakarta, 1996).
[5] K.-E. Thelning, *Steel and its Heat Treatment* (Butterworths, London, 1984).
[6] Ohjoon Kwon // *ISIJ International* **32(3)** (1992) 350.
[7] Pat L. Mangonon, *The Principles of Materials Selection for Engineering Design* (Florida Institute of Tecnology, Melbourne, Florida, 1999).
[8] Shinroku Saito dan tata Surdia, *Pengetahuan Bahan Teknik* (Pt Pradnya Paramita, Jakarta, 1985).
[9] R.E. Smallman, R.J. Bishop, dan Djaprie Sriati, *Metalurgi Fisik Modern dan Rekayasa Material* (Erlangga, Jakarta, 2000).
[10] Wahid Suherman, *Pengetahuan Bahan* (Dikta Institut Teknologi Sepuluh Nopember, Surabaya, 1987).

Materials Physics and Mechanics 37 (2018) 205-211 Received: December 22, 2017

SUPERPLASTICITY OF BOTTOM ASH REINFORCED ALUMINUM METAL MATRIX COMPOSITE

H. Seputro[1]*, Ismail[1], S.-H. Chang[2]

[1]University of 17 Agustus 1945 Surabaya, Indonesia

[2]National Kaohsiung Marine University, Kaohsiung, Taiwan

*e-mail: harjoseputra@untag-sby.ac.id

Abstract. Superplasticity is a phenomenon that occurs in a material, which in certain conditions, at the strain rate and temperature, can show very high ductility and deformation. Superplasticity declares the strain extension between 100 – 1000 %. The purpose of this research was to obtain a composite material properties of superplasticity in Al 6061 reinforced by bottom ash coal. This research used uniaxial tensile test at high temperature. The variable parameters of this research are temperatures (500, 550, 600 °C) and tensile speed (10^{-5}, 10^{-6}, 10^{-7} m/s). The result of this research is the defined maximum extension of 200% at 600 °C, with tensile speed at 10^{-7} m/sec.

Keywords: aluminum; bottom ash; metal matrix composite; superplasticity.

1. Introduction

Superplasticity is a phenomenon, where in certain conditions, like a strain speed and temperature, the material can shows very high ductility and deformation [1]. Superplasticity properties is very important, because they help to calculate force that is needed in forming process. Al-bottom ash coal material has been produced [2], but the superplasticity properties did not know yet. So, this research is very important to find it.

Application of superplasticity consists in obtainment of the processing conditions that approximate end shape of sample. Additionally, the use of connecting technique of the diffusion bonding with forming superplasticity proposes a processing technique that results in the formation of structural components. These components, which be integrated as a whole, increase rigidity and at the same time approaching the final shape of components, reduce the cost of finishing processing [3].

2. Literature review

Metal matrix composites (MMCs). Metal matrix composites are combinations of two or more materials with one of which is a metal being a matrix. Reinforcements are commonly used are oxide ceramics, carbides and nitrides, whose the main function is to support the most part of applied load. At the same time, a function of the matrix is to possess the reinforcement as a whole and to re-distribute optimally external load to each of reinforcing elements.

The advantage of metal matrix composites over metal materials consists as follows [2]:

1. they are lighter compared to metals (reduced weight by 25 – 30%);
2. toughness to the torque is better;
3. hardness and the wear resistance is better;
4. thermal expansion is lower.

http://dx.doi.org/10.18720/MPM.3722018_14

Superplasticity. Superplasticity is one of the material properties that can be achieved at certain microstructure or specific test conditions. Certain microstructure includes very fine grain size and presence of two-phase structure is necessary to maintain a very fine grain size during testing. Materials, which show superplasticity behavior in certain conditions, have phase boundaries, moving through the stretching material during testing (e.g. at the application of thermal cycling).

There are several factors, influencing the occurrence of material superplasticity, so as strain rate and flow stress.

Strain rate and flow stress. Strain rate is defined as a speed or time required for stretching object from an initial length (L_0) to a final length, expressed as

$$\varepsilon' = d\varepsilon / dt . \quad (1)$$

The flow stress is the material property, explaining material resistance to its change, expressed in the form:

$$\sigma = K(\varepsilon^n). \quad (2)$$

Generally, the superplastic material is very sensitive to strain rate and for plastic flow in the solid, it is performed the relationship :

$$\sigma = K\varepsilon'^m , \quad (3)$$

where σ is the stress, ε' is the strain rate and m is the strain rate sensitivity. If m = 1, then the flow stress is proportional to strain rate and material behaves as a Newton viscous fluid.

Therefore, superplastic material has the characteristic features, connected with great value of m. For tensile specimen with length L, cross-section area A, and work load P, we can obtain:

$$\varepsilon' = -(1/A)dA/dt. \quad (4)$$

By substituting expression (4) into (3), we obtain:

$$dA/dt = (P/K)^{1/m}A^{[1-(1/m)]}. \quad (5)$$

Usually, for most of metals and alloys $m \approx 0.1 - 0.2$ and the rate of change A is very strongly depend on A, but cross-section rate does not depend on A, due to uniformity; then specimen geometry has no effect during deformation. The resistance to shrinkage is highly depends on m, and increases quickly, if $m \geq 0.5$. Let us consider the dependence of flow stress on strain:

$$\sigma = K(\varepsilon^n)\varepsilon'^m. \quad (6)$$

In this case, stability of shrinkage depends on factor $(1 - n - m)/m$, but value of n is usually no high. Constitutive material properties in superplasticity conditions can be used to determine the flow stress [1].

Influence of strain rate on flow properties. Increasing strain rate will improve tensile strength. At the same time, influence strain rate on strength will increase with increasing temperature. Yield strength and flow stress at low plastic strain are very dependent on the strain rate compared with the tensile strength.

Conventional strain rate is expressed using linear strain as

$$\frac{de}{dt} = \frac{d(L - L_0)/L_0}{dt} = \frac{1}{L_0}\frac{dL}{dt} = \frac{v}{L_0}. \quad (7)$$

Real strain rate $\frac{d\varepsilon}{dt}$ is defined as

$$\frac{d\varepsilon}{dt} = \frac{d\left[\ln(L/L_0)\right]}{dt} = \frac{1}{L}\frac{dL}{dt} = \frac{v}{L}. \quad (8)$$

From (7), (8) the real strain rate is connected with conventional strain rate in the form:

$$\frac{d\varepsilon}{dt} = \frac{L_0}{L}\frac{de}{dt} = \frac{1}{1+e}\frac{de}{dt}. \quad (9)$$

Generally, dependence between flow stress and strain rate at constant strain and temperature are defined as follow:

$$\sigma = C\left(\frac{d\varepsilon}{dt}\right)^{m}\Big|_{\varepsilon,T}, \tag{10}$$

where m is the strain rate sensitivity. Power *m* can be obtained from the angular dependence log σ – log ε, but simpler way consists in the testing of the rate change. The value *m* is determined by measuring the change of flow stress due to the change of $\frac{d\varepsilon}{dt}$ at constant values of ε and *T*:

$$m = \left(\frac{\partial \ln \sigma}{\partial \ln \dot{\varepsilon}}\right)_{\varepsilon,T} = \frac{\dot{\varepsilon}}{\sigma}\left(\frac{\partial \sigma}{\partial \dot{\varepsilon}}\right)_{\varepsilon,T} = \frac{\Delta \log \sigma}{\Delta \log \dot{\varepsilon}}. \tag{11}$$

The strain rate sensitivity of a metal at room temperature is very low (< 0.1), but *m* increases when the temperature rises, especially at above point ½ of the absolute melting temperature.

3. Methods

In the experimental study, we selected the following parameters:

1. temperature 500 °C, 550 °C, 600 °C.
2. tensile speed 10^{-5}, 10^{-6}, 10^{-7} (m/s).

Test sample. We used Hot Tensile Test Machine Uniaxial "Shimadzu" with test standard JIZ NO. 1. 220 TYPE 1A, the shape and dimensions of the test specimen are present in Fig. 1.

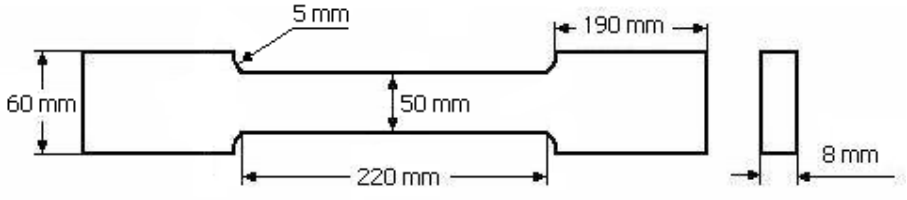

Fig. 1. Shape and sizes of specimen.

Testing Procedure.

1. Measurement of sizes (average diameters) of samples;
2. marking gauge length, namely distance between two points on the test specimen using etcher (cutter) or permanent marker;
3. replacing the specimen with caution in grip Shimadzu testing machine;
4. setting the tensile speed as desired;
5. turn the heater up to the desired temperature and held for some time;
6. start the machine and getting results in the form of graphic load and length;
7. measurement of the sizes of final length and cross-section;
8. marking on the plots of load and length the points of the maximum and fracture;
9. combining the plots of load and length transform them to stress-strain plot.

Figure 2 presents a flow chart for the experiment.

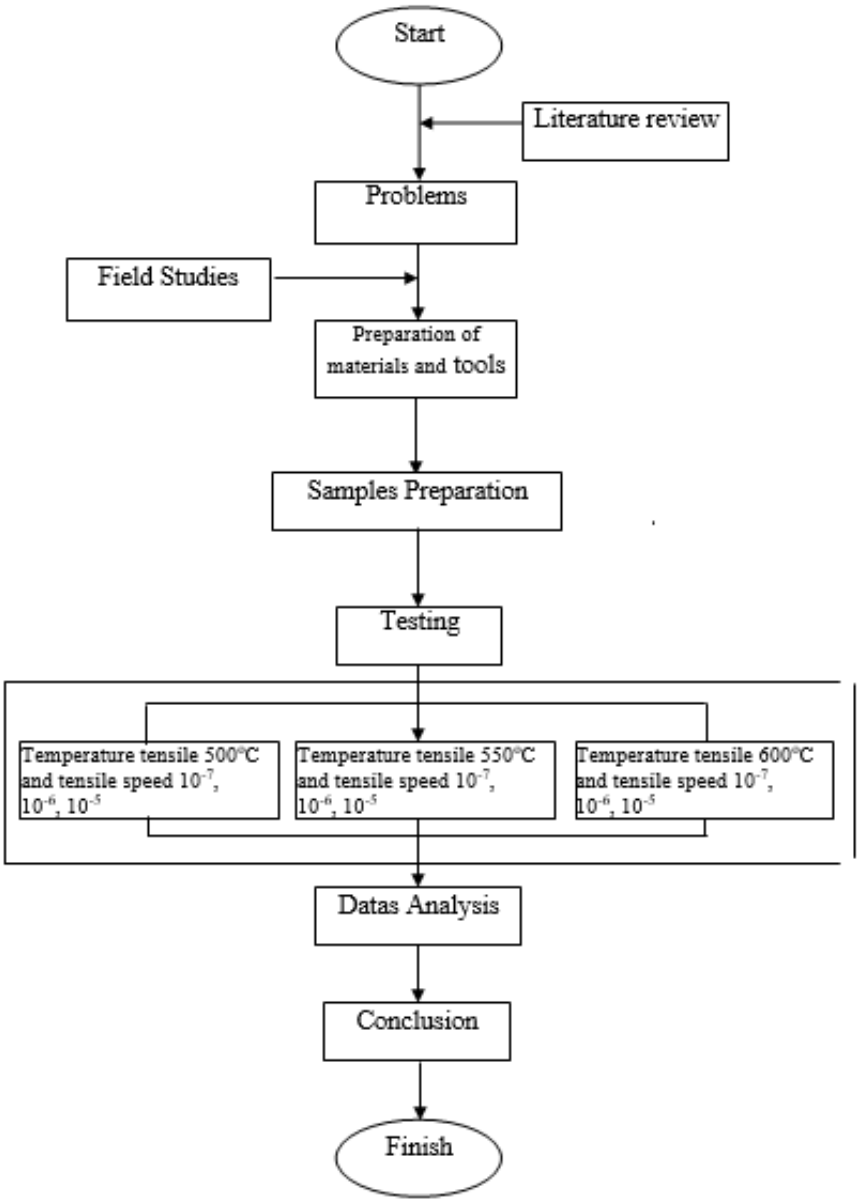

Fig. 2. Flowchart of experiment.

4. Result and Analysis

Tables 1 – 3 present results of hot tensile tests at temperatures of 500, 550 and 600 °C, and speeds of 10^{-5}, 10^{-6}, 10^{-7} m/s.

Table 1. Test results at temperature of 500 °C, and speeds of 10^{-5}, 10^{-6}, 10^{-7} m/s.

Parameter	Speed Tensile (m/s)								
	10^{-5}			10^{-6}			10^{-7}		
	A1	A2	A3	B1	B2	B3	C1	C2	C3
Maximum load (P_{max}), kgF	2035	2033	2036	2040	2039	2041	2047	2044	2046
Final length (l_f), mm	637	636	638	640	640	641	645	647	650

Final thickness, mm	6.5	6.4	6.5	6.4	6.3	6.2	6.3	6.2	6.3
Final wide, mm	21.25	21.61	21.22	21.48	21.82	22.14	21.65	21.93	21.48
Final area (A_f), mm^2	138.125	128.304	137.93	137.472	137.466	137.268	136.395	135.966	135.324
Tensile strength (σ_{TS}), kgF/mm^2	5.087	5.082	5.090	5.100	5.097	5.102	5.117	5.110	5.115
Strain (ε), %	189.545	189.091	190.000	190.909	190.909	191.364	193.182	194.091	195.455

Table 2. Test results at temperature of 550 °C, and speeds of 10^{-5}, 10^{-6}, 10^{-7} m/s.

Parameter	Speed Tensile (m/s)								
	10^{-5}			10^{-6}			10^{-7}		
	A1	A2	A3	B1	B2	B3	C1	C2	C3
Maximum load (P_{max}), kgF	2040	2038	2041	2045	2044	2046	2052	2049	2051
Final length (l_f), mm	644	646	645	649	648	650	653	652	655
Final thickness, mm	5.9	5.8	5.7	5.8	5.6	5.7	5.7	5.6	5.5
Final wide, mm	23.16	23.48	23.93	23.37	24.25	23.75	23.64	24.10	24.42
Final area (A_f), mm^2	136.644	136.184	136.401	135.546	135.800	135.375	134.748	134.960	134.31
Tensile strength (σ_{TS}), kgF/mm^2	5.100	5.095	5.102	5.112	5.110	5.115	5.130	5.122	5.127
Strain (ε), %	192.727	193.636	193.182	195.000	194.545	195.455	196.818	196.364	197.727

Table 3. Test results at temperature of 600 °C, and speeds of 10^{-5}, 10^{-6}, 10^{-7} m/s.

Parameter	Speed Tensile (m/s)								
	10^{-5}			10^{-6}			10^{-7}		
	A1	A2	A3	B1	B2	B3	C1	C2	C3
Maximum load (P_{max}), kgF	2045	2043	2046	2050	2049	2051	2057	2054	2056
Final length (l_f), mm	649	651	650	655	653	655	658	657	660
Final thickness, mm	5.2	5.2	5.1	5.1	5.0	5.0	4.9	4.8	4.7
Final wide, mm	26.07	25.99	26.54	265.34	26.95	26.87	27.29	27.90	28.36
Final area (A_f), mm^2	135.564	135.148	135.354	134.334	134.350	134.750	133.751	133.920	133.292
Tensile strength (σ_{TS}), kgF/mm^2	5.112	5.107	5.115	5.125	5.122	5.127	5.142	5.135	5.140
Strain (ε), %	195.000	195.909	195.455	197.727	196.818	197.727	199.091	198.636	200.000

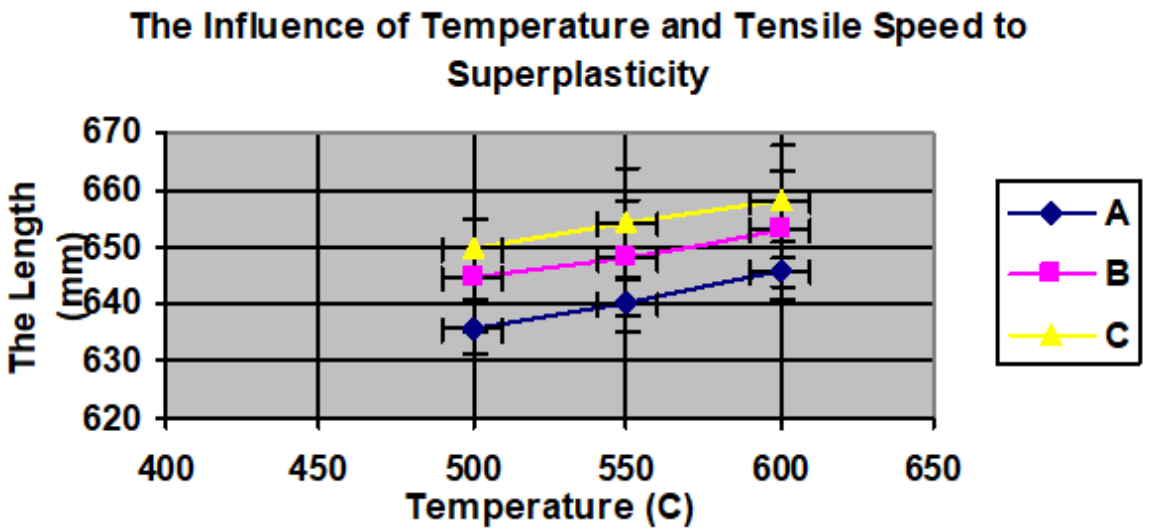

Fig. 3. Influence of temperature and tensile speed on length; tensile speed 10^{-5} m/s (A); 10^{-6} m/s (B); 10^{-7} m/s (C).

Temperature influence on length. Temperature greatly affects the properties of materials, especially the increase in ductility. Increased elasticity is due to the reduction of dislocations as result of the rearrangement of atoms (recrystallization). The effect of

temperature can be seen in Fig. 3, where higher temperature corresponds to the obtained higher extension. In the temperature range considered, superplasticity has occurred.

Influence of tensile speed on length. In the case of tensile rate, the slower tensile corresponds to the greater extension because the lower tensile rate provides opportunities for the material to slip or shear gradually. The influence of the tensile speed can be seen in Fig. 3.

5. Conclusion

1. The higher temperature leads to the longer length. The slower tensile speed causes the longer length. So, we obtained the maximum extension is 200 % at temperature of 600 °C with tensile speed 10^{-7}.
2. With maximum extension of 200% in this material, the superplasticity condition has been obtained.

References

[1] S.W. Agus Hadi, *Jurnal Saint and Teknologi Indonesia* (Humas – BPT/ANY, 2003).
[2] Azki Hakim, *Composite Material Technology* (2007).
[3] *ASM Metal Forming (*American Society for Metal, United States of America, 1995), p. 45.
[4] *ASTM Annual Book of ASTM Standards* (ASTM International: United States of America, 2000), p. 82.
[5] E. Dieter George // *Mechanical Metallurgy* **1** (1987) 297.
[6] Karl-Erik Thelning, *Steel and Its Heat Treatment, 2nd Edition* (Butterworths, London, 1984).
[7] Ir. Tata Surdia dan DR. Shinroku Saito, *Engineering Materials Knowledge*, *4th Edition* (Pradiya Paramita, Jakarta, 1999).
[8] Mel M. Schwartz, *Composite Materials Volume II; Processing, Fabrication, and Applications* (Prentice Hall PTR, Upper Saddle River, New Jersey, 1996).
[9] R.E. Smallman and R.J Bishop, *Modern Physical Metallurgy and Materials Engineering, 6th Edition* (Erlangga, Jakarta, 1999).

Materials Physics and Mechanics 37 (2018) 212-217 Received: December 22, 2017

STUDY OF BOTTOM ASH REINFORCED ALUMINUM METAL MATRIX COMPOSITE FOR AUTOMOTIVE PARTS

I. Wahid*, M. Nafi

Department of Mechanical Engineering, University of 17 Agustus 1945 Surabaya, Indonesia

*e-mail: ichlaswahid@untag-sby.ac.id

Abstract. Low cost and light materials nowadays are the requirements for industry, especially automotive. An aluminum based metal matrix composite (MMC) with bottom ash reinforcement is developed as input and ideas for automotive industry, because of its properties are equivalent with metals, however this MMC is lighter, cheaper, and easy to get. The objective of the study is creating automotive parts using Al metal matrix with bottom ash reinforcement composite. Al-bottom ash composite is formed by HAS method then necessary machining added. The tests performed to the composite are tensile test, hardness test, corrosion and microstructure. The result shows the number of mechanical properties in general, mechanical properties increased about by 30% compared with properties of standard propeller found in market. The microstructure images support the other mechanical destructive testing that Al-bottom ash composite can be used as an alternative as automotive parts.

Keywords: aluminum-bottom ash; automotive parts; mechanical properties; metal matrix composite.

1. Introduction

In recent years, very many projects performed in Indonesian universities directed to the manufacture of electric cars. The high electric car project is performed by the college, which also conducting research on components, used in the electric car, in order to be able to produce their own spare parts and compete with the latest models. Metal matrix composite (MMC) is one of the solutions that can be developed, because the MMC demonstrates a strong, light-weight and corrosion-resistant properties. This type of composite is a widely developed composite matrix of metal, which is aluminum matrix composite (AMC). Currently AMCs are used in the automotive industry for pistons, disc brakes, gears etc. [2].

The advantages of AMCs include their light weight, they have high hardness, high specific modulus and good wear resistance. One of the most important electrical components of a car is a disc cradle [1]. The amplifier component must have a higher elastic modulus than the matrix component [2]. There must be a strong surface bonding between the amplifier and matrix components.

According to the research that has been done, the selected treatment process includes the stages of solution treatment at 540 °C for 4 hours, quenching and aging process. The parameters used are temperatures of 100 °C and 200 °C with aging time of 1, 10 and 24 hours; then the samples were tested. Resulting conclusions touched of the effect of aging temperature from 100 °C to 200 °C on metal matrix composites, which can improve mechanical properties especially tensile strength and hardness. While the aging time from 1 hour to 24 hours may decrease tensile strength even, when hardness increases.

http://dx.doi.org/10.18720/MPM.3722018_15

2. Methods

Aluminum matrix composite with ash coal base consists of aluminum (93.5%), ash coal base (4%), silica sand (2%) and Mg (0.5%).

Casting process. Tools of casting process are casting furnace, K-type thermocouple, mold of the disc footer, mold of the test specimen.

The stages of casting:

1. preparing a cast stove;
2. heating the furnace to a certain temperature after the aluminum material is inserted into the already hot stove;
3. when aluminum has melted at a temperature of 600 °C (measured by thermocouple), the silica sand is mixed to separate the dirt/crust from the aluminum material;
4. after cleaning the aluminum material from the dirt/crust, the coal ash and Mg ash are mixed alternately and stirred;
5. liquid aluminum is poured into a preheated mold.

T6 heat treatment process. Tool of T6 heat treatment process are heating furnace with brand SELECTA and ability of heating up to 1200 ºC, thermometer, three coolants of medium, namely SAE oil 10-40, pure water and brine.

The steps of the T6 heat treatment process:

1. solution heat treatment at 540 ºC
2. quenching media with salt water, pure water, and SAE oil 40
3. artificial aging process with temperature of 180ºC and time variation from 1.3 to 5 h.
4. cooling to room temperature.

Metallographic testing. Metalography testing is first done by cutting the sample in accordance with the size of the specimen, then mounting the specimen so easily to hold it. The surface of the part tested is then smoothed using abrasive papers from the roughest grid to the finest grid, so in the end we can get a shiny specimen. To clean the surface, we polished it by using alumina. Prior to testing, etching solutions were used to dissolve grain boundaries on the surface of the specimen so that they could be seen using a microscope. Furthermore, observation of microstructure was performed by using metallurgical microscope. The microscope is set with standard way and has representative parts allowing to process necessary data.

Hardness testing. Tests were performed by using the Rockwell method. First, the surfaces of specimens were leveled off. Then the tool for the Rockwell hardness test was prepared, in particularly the diamond indentor with angle at tip of 120^{o}. Then it was touched onto the specimen surface with force of 150 kgF and held for 30 seconds. After that, the hydraulic valve is opened to restore the load to its original position.

Tensile testing. Specimen was prepared in accordance with JIS Z2201. The specimen was gripped by the upper and lower chucks. The button “Start” is used for automatical testing. The generated plot “stress – strain” is directly analyzed.

4. Results and analysis

Hardness testing. Figure 1 shows increasing in hardness value after T6 heat treatment. The highest increase in hardness corresponds to artificial aging for one hour in comparison with other considered cases. It can be concluded that the one-hour time of the treatment is the most optimal artificial aging time to increase material hardness.

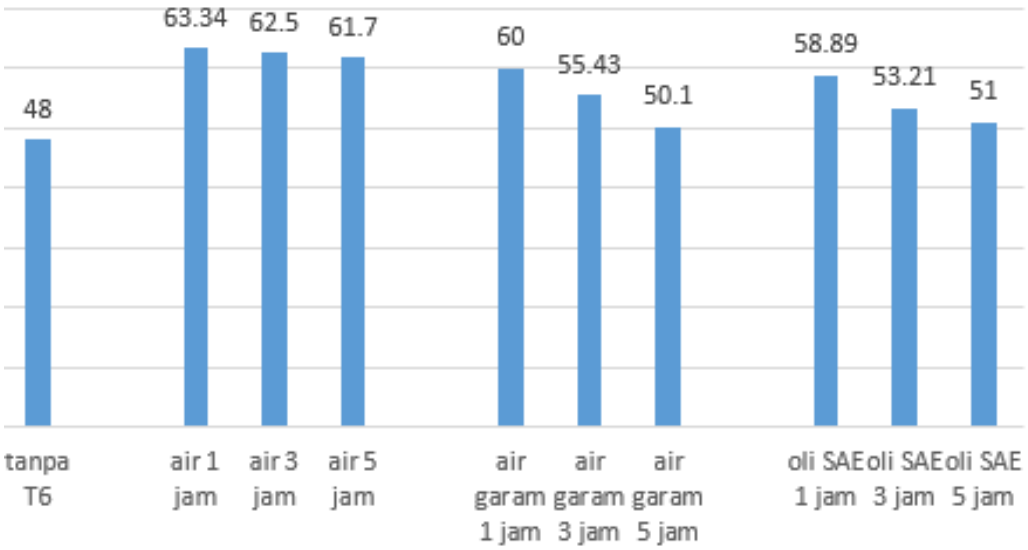

Fig. 1. Results of hardness tests.

Similar results were obtained for the cooling medium. The cooling medium with pure water is the best cooling medium for T6 heat treatment process, proved by its relatively close hardness values at each of the time cases, and the hardness value in the case of cooling by pure water is higher than for other cooling media. This proves Basuki's theory [4] about pure water cooling medium. The highest hardness value (63.34 HRc) was obtained for pure water cooling at artificial aging time for one hour.

Tensile testing. From Fig. 2 it can be concluded that T6 heat treatment has an effect on the increasing of strength value. The highest increase of the tensile strength can be seen predominantly in the artificial aging for one hour. While at comparison of cooling media, cooling by using pure water demonstrates the highest value compared with other cooling media. So, the case of cooling with pure water and artificial aging time of one hour is the most optimal decision.

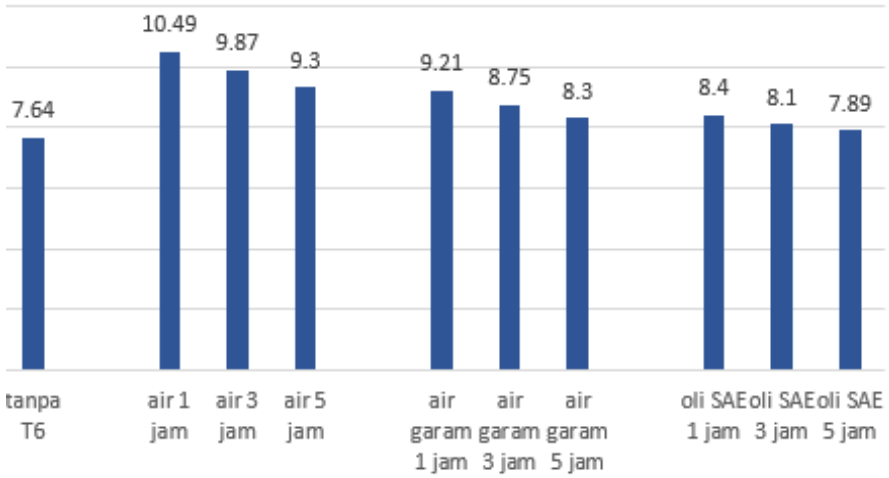

Fig. 2. Results of tensile tests.

In this tensile strength test, the highest tensile strength value (10.49 kgF/mm^2) was obtained for water cooling media with at artificial aging time of 1 hour. In a whole, there is coincidence of the behavior of mechanical properties: strength and hardness increase according to the theory of Dieter [5]. At increasing the strength, the hardness of a material also increases, accompanied by the decrease of its ductility.

Microstructure testing. Figures 3 – 6 present specimen microstructures for different cases of quenching medium and holding time. The calculated number of grains (G) and mean diameter of grains (D_m) are obtained by direct measurements in the figures.

Table 1 presents results for the tested microstructures on the disc cradle with estimation of the effect of aging time (1, 3, and 5 hours) and the cooling medium/quenching (brine, pure water and SAE 10-40 oil) on number of grains and the mean diameter of the granules on aluminum-ash coal base. In particular, we obtained the following results for holding time of 5 hours: (i) at the water cooling medium, the number of grains G = 5.47 and the mean diameter of the granules D_m = 55 μm; (ii) at the brine cooling medium, the number of grains G = 5.02 and the mean diameter of the granules D_m = 65 μm, (iii) at the SAE 10-40 hydraulic oil cooling medium, the number of grains G = 7.58 and the mean diameter of the granules D_m = 27 μm. In the case without T6 heat treatment, the number of grains G = 3.90 and the mean diameter of the granules D_m = 90 μm.

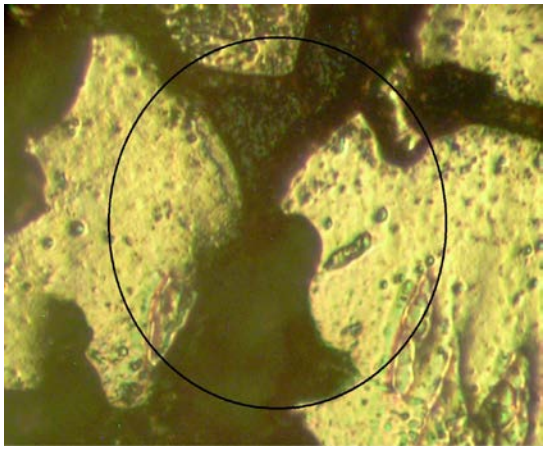

Fig. 3. Specimen microstructure for water is the quenching medium and holding time – 1 h; number of grains, G = 4.85, mean diameter of grains, D_m = 65 μm.

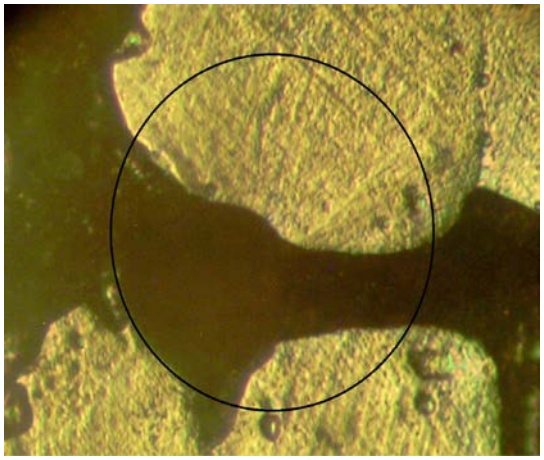

Fig. 4. Specimen microstructure for salt water is the quenching medium and holding time – 1h; number of grains, G = 3.37, mean diameter of grains, D_m = 0.105 μm.

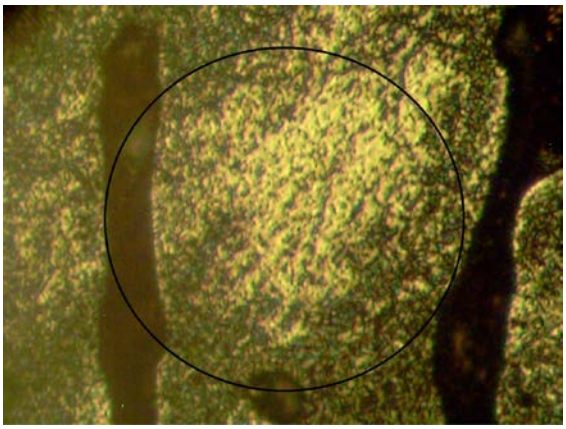

Fig. 5. Specimen microstructure for SAE Oil is the quenching medium and holding time – 1h; number of grains, G = 6.52, mean diameter of grains, D_m = 30 μm.

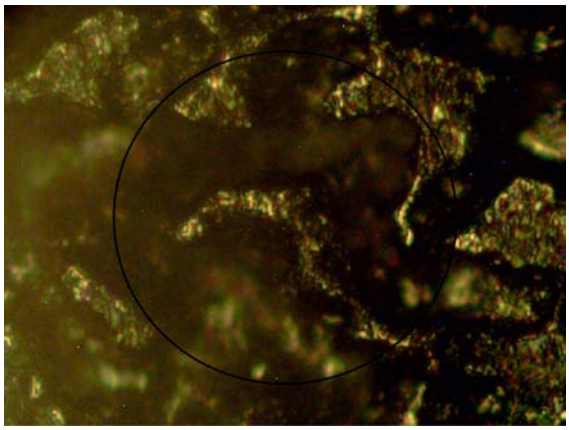

Fig. 6. Specimen microstructure without treatment; number of grains, G = 3.90, mean diameter of grains, D_m = 90 μm.

Table 1. Grain size for various cases of quenching medium and holding time.

Quenching medium	Holding time (hours)		
	1	3	5
Pure Water	G = 4.85; D_m = 65 μm	G = 4.95; D_m = 65 μm	G = 5.47; D_m = 55 μm
Salt water	G = 3.37; D_m = 0.105 μm	G = 4.25; D_m = 75 μm	G = 5.02; D_m = 65 μm
Oil SAE 10-40	G = 6.52; D_m = 30 μm	G = 6.90; D_m = 30 μm	G = 7.58; D_m = 27 μm
Without treatment	G = 3.90; D_m = 90 μm		

5. Conclusion

In the grain growth in the structure of the disk holder component, there is a process without T6 heat treatment, leading to the number of grains G = 3.90 and obtaining the mean diameter of D_m = 90 μm.

Moreover, the following results for holding time of 5 hours were obtained:

1. at the water cooling medium, the number of grains G = 5.47 and the mean diameter of the granules D_m = 55 μm;
2. at the brine cooling medium, the number of grains G = 5.02 and the mean diameter of the granules D_m = 65 μm,

3. at the SAE 10-40 hydraulic oil cooling medium, the number of grains G = 7.58 and the mean diameter of the granules D_m = 27 μm.

References

[1] S.W. Agus Hadi, *Jurnal Saint and Teknologi Indonesia* (Humas – BPT/ANY, 2003).
[2] Azki Hakim, *Composite Material Technology* (2007).
[3] *ASM Metal Forming* (American Society for Metal, United States of America, 1995), p. 45.
[4] *ASTM Annual Book of ASTM Standards* (ASTM, United States, 2000), p. 82.
[5] E. Dieter George // *Mechanical Metallurgy* **1** (1987) 297.
[6] Karl-Erik Thelning, *Steel and Its Heat Treatment, 2nd Edition* (Butterworths, London, 1984).
[7] Ir. Tata Surdia and DR. Shinroku Saito, *Engineering Materials Knowledge, 4th Edition* (Pradiya Paramita, Jakarta, 1999).
[8] M.M. Schwartz, *Composite Materials Volume II; Processing, Fabrication, and Applications* (Prentice Hall PTR, Upper Saddle River, New Jersey, 1996).
[9] R.E. Smallman and R.J Bishop, *Modern Physical Metallurgy and Materials Engineering, 6th Edition* (Erlangga, Jakarta, 1999).

Submission of papers:
Manuscript should be submitted (**both MS Word and PDF**) by e-mail to: **mpmjournal@spbstu.ru**
After a confirmation of the paper acceptation, the authors should send the signed hard copy of the "Transfer of Copyright Agreement" form (available at http://www.mpm.spbstu.ru section "Authors") by regular post to "Materials Physics and Mechanics" editorial office:
Periodicals Editorial Office, Institute of Advanced Manufacturing Technologies, Peter the Great St.Petersburg Polytechnic University, Polytechnicheskaya, 29, St.Petersburg 195251, Russia.
The scanned copy of the signed "Transfer of Copyright Agreement" should be send by e-mail to: mpmjournal@spbstu.ru.

Filetype:
Authors are invited to send their manuscripts **as MS Word file with PDF format copy.**
MS Word file should be prepared according to the general instructions bellow; we are kindly asking the authors to look through the detail instruction at: http://www.mpm.spbstu.ru.

Length:
Papers should be limited to 30 typewritten pages (including Tables and Figures placed in the proper positions in the text).

Structure of the manuscript:

PAPER TITLE: CENTERED,

TIMES NEW ROMAN 14 BOLD, CAPITAL LETTERS

A.B. Firstauthor[1], C.D. Secondauthor[2*] –Times New Roman 12, bold, centered

[1]Affiliation, address, country - Times New Roman 10, centered

*e-mail: e-mail of the corresponding author - Times New Roman 10, centered

Abstract. Times New Roman 12 font, single line spacing. Abstract should not exceed 12 lines.
Keywords: please, specify paper keywords right after the abstract.

Paper organization. Use Times New Roman 12 font with single line spacing. Use *Italic* font in order to stress something; if possible, please, use **bold** for headlines only.

Page numbering. Please, do not use page numbering.

Tables, Figures, Equations. Please, see the sample file at http://www.mpm.spbstu.ru for more details.

References
References should be subsequently numbered by Arabic numerals in square brackets, e.g. [1,3,5-9], following the sample style below:
[1] A.K. Mukherjee // *Materials Science and Engineering: A* 322 (2002) 1.
[2] C.C. Koch, I.A. Ovid'ko, S.Seal, S. Veprek, *Structural Nanocrystalline Materials: Fundamentals and Applications* (Cambridge University Press, Cambridge, 2007).
[3] A.E. Romanov, V.I. Vladimirov, In: *Dislocations in Solids*, ed. by F.R.N. Nabarro (North Holland, Amsterdam, 1992), Vol. 9, p.191.
[4] C.K. Takemori, T.D. Müller, M.A. De Oliveira, *Numerical simulation of transient heat transfer during welding process*, In: *International Compressor Engineering Conference* (Purdue, USA 2010).
[5] W. Pollak, M. Blecha, G. Specht // *US Patent 4572848.*
[6] http://www.mpm.spbstu.ru

Правила подготовки статей:

Рукопись (**английский язык, MS Word и копия PDF**) должна быть направлена в редакцию журнала по электронной почте: **mpmjournal@spbstu.ru**.

После подтверждения принятия статьи в печать, авторы должны отправить подписанные:

1. Соглашение о передаче авторских прав (http://www.mpm.spbstu.ru, раздел «Авторам»);
2. Экспертные заключения о том, что материалы статьи не содержат сведений, составляющих государственную тайну, и информацию, подлежащую экспортному контролю; по адресу:

Россия, 195251, Санкт-Петербург, Политехническая, д. 29, Санкт-Петербургский политехнический университет Петра Великого, Институт передовых производственных технологий, Редакция периодических изданий.

Скан-копии подписанных документов просим направить по электронной почте: mpmjournal@spbstu.ru

Тип файла:

Редакция принимает **файлы MS Word с копией в формате PDF**. Статья должна быть подготовлена в соответствии с настоящей инструкцией, мы просим авторов также следовать более подробным инструкциям на сайте журнала http://www.mpm.spbstu.ru в разделе «Авторам».

Длина статьи:

Статья не должна превышать 30 страниц формата А4, включая Таблицы и Рисунки, размещенные непосредственно в соответствующих местах.

Общие правила оформления статьи:

НАЗВАНИЕ СТАТЬИ: ВЫРОВНЯТЬ ПО ЦЕНТРУ, ШРИФТ, TIMES NEW ROMAN 14 BOLD, ЗАГЛАВНЫЕ БУКВЫ

Автор(ы): **А.Б. Первыйавтор[1], В.Г. Автор[2*]**- шрифт Times New Roman 12, bold, по центру

[1]Наименование организации, адрес, страна - шрифт Times New Roman 10, по центру

* e-mail автора, представившего статью - шрифт Times New Roman 10, по центру

Аннотация. Аннотация статьи составляет не более 12 строк. Используйте шрифт Times New Roman 12, одинарный межстрочный интервал.

Ключевые слова: укажите ключевые слова после аннотации.

Как организовать текст статьи. Используйте шрифт Times New Roman 12, одинарный межстрочный интервал. При необходимости выделить какую-либо информацию используйте *курсив*. Используйте **полужирный** шрифт только для заголовков и подзаголовков.

Номера страниц. Пожалуйста, не используйте нумерацию страниц

Таблицы, Рисунки, Уравнения. Подробные правила оформления данных элементов статьи приведены в инструкции на сайте журнала http://www.mpm.spbstu.ru

Литература

Ссылки приводятся в тексте в квадратных скобках [1,3,5-9]. Стиль оформления ссылок:

[1] A.K. Mukherjee // *Materials Science and Engineering: A* 322 (2002) 1.

[2] C.C. Koch, I.A. Ovid'ko, S.Seal, S. Veprek, *Structural Nanocrystalline Materials: Fundamentals and Applications* (Cambridge University Press, Cambridge, 2007).

[3] A.E. Romanov, V.I. Vladimirov, In: *Dislocations in Solids*, ed. by F.R.N. Nabarro (North Holland, Amsterdam, 1992), Vol. 9, p.191.

[4] C.K. Takemori, T.D. Müller, M.A. De Oliveira, *Numerical simulation of transient heat transfer during welding process*, In: *International Compressor Engineering Conference* (Purdue, USA 2010).

[5] W. Pollak, M. Blecha, G. Specht // *US Patent 4572848.*

[6] http://www.mpm.spbstu.ru

МЕХАНИКА И ФИЗИКА МАТЕРИАЛОВ

37 (2) 2018

Учредители: Санкт-Петербургский политехнический университет Петра Великого,

Институт проблем Машиноведения Российской академии наук

Издание зарегистрировано федеральной службой по надзору в сфере связи,

информационных технологий и массовых коммуникаций (РОСКОМНАДЗОР),

свидетельство ПИ №ФС77-69287 от 06.04.2017 г.

Телефон редакции

+7 (812) 591-65-28

E-mail: mpmjournal@spbstu.ru

Компьютерная верстка А.Ю. Зобачева

Подписано в печать 28.05.2018 г. Формат 60x84/8. Печать цифровая
Усл. печ. л. 10,0. Тираж 100. Заказ____.

Отпечатано с готового оригинал-макета, предоставленного автором
в Издательско-полиграфическом центре Политехнического университета Петра Великого. 195251, Санкт-Петербург, Политехническая ул., 29.
Тел.: (812) 552-77-17; 550-40-14.

MPM SCIENTIFIC JOURNAL

MPM, Vol. 37, No. 2, 2018